SPECTROSCOPIC CHARACTERIZATION OF IRON-OXYGEN INTERMEDIATES IN HUMAN AROMATASE (CYP19A1)

BY

ABHINAV LUTHRA

DISSERTATION

Submitted in partial fulfillment of the requirements
for the degree of Doctor of Philosophy in Biochemistry
in the Graduate College of the
University of Illinois at Urbana-Champaign, 2015

Urbana, Illinois

Doctoral Committee:

Professor Stephen G. Sligar, Chair
Professor Susan A. Martinis
Professor Paul J. Hergenrother
Professor David M. Kranz

ABSTRACT

CYP19A1 or aromatase, is a human steroidogenic P450 important for estrogen biosynthesis in humans. Over activation of aromatase results in malignancies of the breast tissue, especially in post menopausal women. In fact, aromatase inhibitors constitute the front line therapy for estrogen receptor positive (ER+) breast cancer in post-menopausal women which accounts for over 70% of all breast cancer cases in the United States.

Starting with its androgenic substrates, testosterone and androstenedione, CYP19A1 forms estradiol and estrone utilizing one molecule of atmospheric oxygen and two reducing equivalents in the form of NADPH. This is accomplished in a three-step process one of which involves a carbon-carbon bond scission and aromatization. The catalytic mechanism of P450s has been long studied and it is well known that an oxo-ferryl π-cation radical, known as "Compound 1" in P450 chemistry is the reactive intermediate that catalyzes most of the reactions of P450s. The identity of the reaction intermediate that catalyzes the terminal step estrogen biosynthesis by CYP19A1 is still a mystery. There is evidence in the literature suggesting the involvement of Compound 1 via a hydrogen abstraction that initiates deformylation and subsequent aromatization. There is also suggestion of the peroxo-anion or "Compound 0" acting as a nucleophile, attacking the electrophilic carbonyl carbon of 19-oxo-androstenedione forming a peroxide adduct that then fragments to produce acyl-carbon cleavage.

Owing to the interesting chemistry CYP19A1 catalyzes and its role in human health I focused my attention towards elucidating the mechanism of this critical enzyme with the hope that a detailed picture of the workings of CYP19A1 will help guide efforts to make more specific inhibitors and improve breast cancer prognosis.

CYP19A1 is a membrane-bound hemeprotein with a rich spectroscopic landscape thus affording an opportunity to apply a repertoire of biophysical approaches to help piece together a reaction mechanism. I used the Nanodisc technology to stabilize CYP19A1 in its native membrane-like environment to obtain a mono-disperse, stable and homogenous enzyme preparation that is amicable to the optical, resonance Raman (rR) and electron paramagnetic resonance (EPR) spectroscopy and also, cryoradiolysis and cryospectroscopy. The approach I have applied in this project has been that of characterizing the individual fate of reaction intermediates on their way from substrates to products thereby catching them 'in action'.

My cryospectroscopy, EPR, rR and steady state kinetics efforts outlined in this doctoral thesis all implicate “Compound 1” as the reactive intermediate that is responsible for the carbon-carbon scission reactivity of CYP19A1.

To Mom, Dad, Seema masi, Soumya and Zeshta

ACKNOWLEDGEMENTS

I would like to thank my advisor Prof. Steve Sligar for taking me under his wing and helping me grow into the mature and independent scientist that I am today. I am deeply grateful for his continued support, patience and interest in my intellectual and professional growth. He has encouraged me to pursue projects of my own, attend meetings and workshops, take time off research to go on a summer internship and explore entrepreneurial ventures. I cannot thank him enough for the variety of experience that I have gathered being a part of his research group. I also owe a huge piece of gratitude to Dr. Ilia Denisov whose understanding and knowledge of the physical world is unparalleled. Ilia truly believes in taking time out to mentor young graduate students when they join the lab and I'd like to thank him on behalf of all the recent graduates of the Sligar lab for his mentorship. I am happy to have gotten the chance to work with him closely during parts of my project. I clearly remember the time Steve and Ilia sat me down and helped me develop an outline for a poster at an international meeting after I had just told them that I wanted to back out at the last moment. I was extremely nervous and both Steve and Ilia's confidence in me helped me make an award winning poster presentation.

I've also benefited immensely from interactions with my current and former lab mates –Dr. Mark McLean, Dr. Tim Bayburt, Lena Grinkova, Mike Gregory, Xin Ye, Ivan Lenov, Yogan Khatri, Dr. Mike Marty, Prof. Aditi Das, Dr. Dan Frank and I would like to thank them too. Aretta Weber deserves a special thank you for being the binding glue that holds the lab together and watches out for all of us. They say you are the average of five people you spend most of your time with. I am grateful to have been constantly surrounded by such highly intelligent and capable people.

I would also like to thank my collaborators Dr. Piotr Mak and Dr. James Kincaid at Marquette University and Roman Davydov and Dr. Brian Hoffman at Northwestern University for bringing their expertise in resonance Raman and electronic paramagnetic resonance respectively to the project. Their contributions have been greatly beneficial for the development of my thesis.

Much of the work has been paid for with grants to Dr. Sligar from National Institutes of Health. However, I would also like to acknowledge the generous contribution made by the Department of Biochemistry via the Herbert E. Carter fellowship during 2009-2010.

Above all, I would like to thank my entire family especially my parents, Vandana and Ravindra and my sister, Soumya for their endless love, continuous encouragement, and for being ever so patient and accommodating throughout this long but rewarding journey of graduate school.

TABLE OF CONTENTS

Chapter 1: Introduction

OBJECTIVE, APPROACH AND OVERVIEW

CYP19A1, or aromatase is a human steroidogenic P450 important for estrogen biosynthesis in humans. Starting with its androgenic substrates, testosterone and androstenedione, it forms estradiol and estrone utilizing one molecule of oxygen and two reducing equivalents in the form of NADPH. This is accomplished in a three-step process one of which involves a carbon-carbon bond scission and aromatization. Over activation of aromatase results in malignancies of the breast tissue, especially in post-menopausal women. In fact, aromatase inhibitors constitute the front line therapy for ER+ breast cancer in post-menopausal women, which accounts for over 70% of all breast cancer cases in the United States. Owing to the interesting chemistry CYP19A1 catalyzes and its role in human health we've focused our attention towards elucidating the mechanism of this critical enzyme. Our hope is that a detailed picture of the workings of CYP19A1 will help guide efforts to make more specific inhibitors and improve breast cancer prognosis.

CYP19A1 is a membrane-bound hemeprotein with a rich spectroscopic landscape thus affording an opportunity to apply a repertoire of biophysical approaches to help piece together a reaction mechanism. I used the Nanodisc technology to stabilize CYP19A1 in its native membrane-like environment to obtain a mono-disperse, stable and homogenous enzyme preparation that is amicable to the optical, RR and EPR spectroscopy and also, cryoradiolysis and cryospectroscopy. The approach I have applied in this project has been that of characterizing the individual fate of reaction intermediates on their way from substrates to products thereby catching them '*in action*'.

Chapter 1 provides a background about CY19A1; cytochrome P450s, the enzyme superfamily CYP19A1 belongs to and the Nanodisc technology. Chapter 2 details temperature derivative spectroscopy (TDS), a technique that was developed to monitor autoxidation in P450s, behavior of the first quasi-stable iron-oxygen intermediate in P450 called the oxy-ferrous complex. Chapter 3 provides an account of how TDS can be extended to monitor other process important in P450s such as spin-state equilibrium, diatomic ligand binding and behavior of the peroxo-anion upon thermal annealing. Chapter 4 and 5 contain information obtained about the nature of oxy-ferrous and reduced oxy-ferrous complexes of CYP19A1 in various substrate-bound states using electron paramagnetic resonance (EPR) and resonance Raman (rR) spectroscopies. Chapter 6 details the

steady state turnover behavior of CYP19A1 and the effect of solvent substitution on NADPH consumption and product formation.

CYTOCHROMES P450

Introduction

Cytochromes P450 are an extremely diverse group of enzymes found across the tree of life that catalyze a variety of chemical modifications on an equally diverse set of substrate molecules. They are found animals, plants, insects, bacteria, fungi and even viruses! Over 21,000 P450s have been discovered till date (Nelson 2009). D. Nelson in his recent article presents a beautiful account of how P450s have helped shape our planet's history and our present biosphere over millions of years of evolution that it really makes one wonder how life on earth would be like without these magical enzymes (Nelson 2013). 57 of these 21,000+ P450s belong to humans where they catalyze critical functions of xenobiotic metabolism such as CYP3A4 and CYP2C9 and steroid hormone biosynthesis such as CYP19A1, CYP17A1 and CYP11A1 (Figure 1). CYP19A1, the subject of this thesis, takes androgens, androstenedione and testosterone and converts them to estrogens, estrone and estradiol respectively.

Catalytic mechanism of P450s

Cytochrome P450s, using two reducing equivalents in the form of NADPH and one molecule of molecular oxygen catalyze a variety of chemical transformations including, but not limited to, hydroxylation of unactivated alkanes, epoxidation, N-oxidation, dearylation and aromatization. The unique ability of these enzymes to catalyze such a broad variety of reactions using the same active site geometry has piqued the interest of many a researchers worldwide since their discovery by Omura and Sato fifty years ago (Omura & Sato 1962). The reaction mechanism of P450s is depicted in the form of a wheel (Figure 2) with seven different iron-oxygen intermediates, each representing a different stage of the reaction in terms of state of the bound substrate, bound oxygen, electronic state of heme iron and protonation. The wheel also contains three unproductive pathways whereby the enzyme undergoes futile cycles, consuming NADPH and O_2 but not yielding any product. These are referred to as the autoxidation shunt, the peroxide shunt and the oxidase shunt. They will be discussed in more detail later in the text.

The enzyme in its resting state exists as a water-ligated, hexa-coordinated, low-spin ferric heme [**1**]. Water is a weak ligand and is easily knocked off by an incoming substrate. Displacement of the

water molecule converts the enzyme to a penta-coordinated, high-spin ferric heme [**2**]. The spin state change is accompanied by a large positive shift in the heme-iron reduction potential. The heme-iron can now be easily reduced by electrons from NADPH supplied in turn by P450's redox partner, cytochrome P450 reductase or CPR. The resulting ferrous heme [**3**] binds a molecule of oxygen to yield the oxy-ferrous complex [**4**], the first quasi-stable intermediate in P450s. The oxy-ferrous complex lies at the cusp of the autoxidation shunt, whereby a spontaneous loss of the bound oxygen and reducing equivalents in the form a superoxide anion returns the enzyme back to its ferric resting state. On the productive arm of the catalytic wheel, the oxy-ferrous complex is reduced by another electron from CPR to form the peroxo-anion [**5a**]. Protonation at the distal oxygen converts the peroxo anion into the hydroperoxo anion [**5b**]. Peroxo anion and hydroperoxo anion are interchangeably referred to as 'Compound 0' in P450 chemistry. Another protonation at the distal oxygen causes a heterolytic O-O bond cleavage releasing a water molecule and yielding an oxo-ferryl π-cation radical, also referred to as 'Compound 1' [**6**]. Protons required for the first and second protonation events are provided by an intricately laid out hydrogen bonding network formed by a conserved acid-alcohol pair, usually aspartic acid and threonine and water molecules present in the active site. Substrate hydroxylation occurs via the hydrogen abstraction/ oxygen rebound mechanism mediated Compound 1 (Groves 1985). The hydroxylated product is released and the enzyme returns back to its resting state.

In addition to the autoxidation shunt, two more uncoupling pathways exist. Incorrect protonation i.e. that at the proximal oxygen atom of the peroxo anion results in futile cycling releasing the bound -OOH moiety as hydrogen peroxide. This uncoupling pathway is referred to as the peroxide shunt. The highly reactive ferryl-oxo intermediate [**6**] instead of oxygenating the substrate can itself be oxidized to water, in a process referred to as the oxidase shunt. The oxidase shunt effectively results in four-electron reduction of dioxygen molecule with the net formation of two molecules of water.

HUMAN AROMATASE

Role, gene organization of CYP19 and tissue specific expression

Human aromatase is the product of the 123 kb long CYP19A1 gene on chromosome 15q.21.1. 93 kb of the 123 kb form the regulatory region, housing at least 10 different promoters. The 30 kb coding region contains nine different coding exons and a number of non-coding alternative first exons. Together, these features allow for a high degree of tissue specific regulation of expression (Bulun et

al. 2004). Aromatase is primarily expressed in ovaries, testes and brain where it is responsible for reproductive development, fertility and sexual behavior, respectively through estrogen synthesis. In addition to the gonads and brain, humans and other primates express aromatase in extragonadal sites such as bone, adipose tissue, placenta and vascular tissue (Simpson et al. 1994). In these tissues estrogens are responsible for bone mineralization, closure of the epiphyseal plates, lipid homeostasis and prevention of atherosclerosis (Simpson et al. 2002; Harada et al. 1999).

Mutations in CYP19A1 leading to human aromatase deficiency have been known to cause virilization of females, pseudohemaphrodism in female newborns and tall stature due to failure in epiphyseal closure and bone undermineralization in their male counterparts (Simpson 2000; Jones et al. 2007). These abnormalities occur due to the inability of affected individuals to produce endogenous estrogens are often treatable by hormonal therapy if detected early. Overexpression of aromatase causes aromatase excess syndrome (AEXS) characterized by gynecomastia, infertility and Leydig cell tumors in males and thelarche in females. Both sexes experience an premature growth spurt and early closure of epiphyseal plates (Shozu et al. 2003). These conditions arising from mutations of the CYP19A1 gene are rare. A more severe impact of abnormal aromatase expression on human health is seen in post-menopausal women in the form of estrogen receptor positive, or ER+ breast cancer. ER+ breast cancer has the poorest long-term survival rates among various breast cancer subtypes and claims upwards of 39,000 lives each year in the United States alone.[1]

Aromatase and breast cancer

The ovarian granulosa cells are the primary source of aromatase in premenopausal women. In postmenopausal women however, estrogen is no longer synthesized in the ovary but in other tissues such as vascular endothelium, smooth muscle cells, skin and adipose tissue including the adipose tissue present in the breast itself. Estrogens synthesized within these extragonadal sites act predominantly at the local tissue level in a paracrine or intracrine manner (Labrie 2003). As a consequence, despite low circulating estrogen levels, the concentration of estrogen in the breast tissue of postmenopausal patients is several fold-higher than that in premenopausal women. Abnormal levels of estrogen in the breast tissue lead to an over activation of estrogen receptor which in turn leads to uncontrolled cell growth and development of a tumor.

[1] Breast Cancer Facts & Figures 2013-2014:
http://www.cancer.org/acs/groups/content/@research/documents/document/acspc-042725.pdf

Approximately 75% of breast cancers test positive for the estrogen receptor (ER), the progesterone receptor (PgR), or both. Estrogen stimulation of these receptors is an important factor for growth and development of a tumor. Competitive antagonists for the estrogen receptor such as Tamoxifen have been used to treat patients with ER+ breast cancer since its FDA approval in 1977. Tamoxifen along with reducing estrogen receptor activation prevents bone demineralization and improves their lipid profiles (Love 1994). However, Tamoxifen treatment increases the risk for endometrial cancer and thromboembolic disease (Cuzick et al. 2003) in these patients. There are also instances of relapse occurring 15 years after a 5-year course of Tamoxifen treatment (Fisher et al. 2001).

Aromatase inhibitors (AIs) such as exemestane, anastrozole, letrozole constitute the state of art for ER+ breast cancer treatment. AIs reduce estrogen levels by inhibiting the production of aromatase itself. AIs do not inhibit the ovarian production of aromatase so only women without functioning ovaries benefit from this kind of therapy. The benefit of using AIs is fewer serious side effects , such as endometrial cancer and stroke, than Tamoxifen. However, the use of AIs has been associated with heart problems and osteoporosis. There is a dire need for more specific, mechanism-based inhibitors to aromatase to provide better disease prognosis for breast cancer patients and therefore, it is paramount that we direct our efforts towards gaining a molecular understanding of this unique enzyme.

Structural organization

CYP19A1 consists of a thiolate-ligated heme prosthetic group enclosed in a polypeptide chain of 503 amino acids. A hydrophobic tail of about 40 amino acids on its N-terminal helps it attach to the endoplasmic reticulum where it is localized. In 2009, Ghosh and colleagues (Ghosh et al. 2009) solved the X-ray crystal structure of full-length human placental aromatase in complex with its substrate, androstenedione (pdb id: 3eqm).

CYP19A1 retains the characteristic P450 fold with some unique features. Most notable is the I-helix distortion caused by a proline residue at position 308, a residue unique to CYP19A1 among other P450s. I-helix distortion in P450s is not uncommon (Podust et al. 2001; Rowland et al. 2006; Nagano et al. 2005; Williams et al. 2004) however, in this case it seems to be specifically designed to create room for the 3-keto group of the substrate in CYP19A1's active site. Superposition of the aromatase backbone with bacterial P450cam and P450eryF as well as with human CYP3A4 and CYP2D6 has shown that without this shift, the 3-keto end of the substrate would clash with the I-helices of respective P450s (Ghosh et al. 2009)

The active site of aromatase is made up of hydrophobic and polar residues arranged in a manner that complement the steroid backbone and confer the enzyme its high specificity towards its substrates. Additional H-bonding interactions between the 3-keto and 17-keto oxygen atom of androstenedione and Met-374/ Arg 115 and Asp 309 respectively stabilize the substrate molecule in a specific orientation with respect to the heme iron.

There exists an elaborate network of H-bonding and salt-bridge interactions involving among other residues, Asp-309, 3-keto group of the substrate and water molecules present in the active site that presumably provide protons for the first and second protonation of the oxy-ferrous complex and keeps the Asp-309 protonated so it may participate in substrate binding interaction as well.

The 2.9 °A resolution structure is informative but does not offer insights into the reaction mechanism for the aromatization step of CYP19A1. Moreover, the crystal structure was obtained with AD, substrate for the hydroxylation step, bound at the active site.

REACTION CATALYZED

CYP19A1 catalyzes the conversion of androgens (androstenedione, testosterone, and 16α-hydroxytestosterone) to estrogens (estrone, 17β-estradiol, and estriol, respectively) via a three-step reaction (Figure 3). The first two steps involve consecutive hydroxylation reactions that result in the formation of a C19 hydroxyl, followed by a gem-diol intermediate that dehydrates to yield a C19 aldehyde. In the third and final step of estrogen synthesis, the carbon-carbon bond between C19 and C10 undergoes scission resulting in release of the C19 carboxyl as formic acid and a concomitant aromatization of A-ring of the steroid molecule (Akhtar et al. 2011).

Proposed mechanisms of C-C lyase and aromatization by human aromatase

The first two steps of CYP19A1 catalysis are generally accepted as being classic Cpd1 mediated hydroxylations. During these steps, the acid-alcohol pair, T310 and D309 conserved in the I-helix of CYP19A1 along with active site water molecules play an important role in protonating the distal oxygen atom of the peroxo anion to facilitate O-O bond cleavage and generate Cpd 1, as described in CYP101 and CYP17A1 (Poulos et al. 1985; Raag et al. 1991; Imai & Nakamura 1989; Nagano & Poulos 2005; Vidakovic et al. 1998; Khatri et al. 2014). However, the mechanism of the third step is still a matter of considerable debate. Two competing hypotheses exist. They are referred to as the 'Compound 0', or peroxo-anion mechanism and the 'Compound 1' mechanism on the basis of the reactive intermediate that is proposed to carry out catalysis.

In the 'Compound 0 mechanism' (Panel A, Figure 4) C-C bond cleavage occurs through the participation of Fe^{III}-$[O\text{-}O]^{-2}$ species, or peroxo anion that is stabilized by the electrophilic property of the carbonyl group of 19-oxo-AD. It has been proposed that 19-oxo-AD causes a displacement of Thr-310 of the acid-alcohol pair of CYP19A1. This disturbs the H-bonding network at the active site and as a result proton delivery to the distal oxygen of the heme-O-O moiety is stalled, thus stabilizing the peroxo anion (Graham-Lorence et al. 1995). The peroxo anion acting as a nucleophile attacks the C19 carbonyl of its 19-oxo substrate generating a peroxide adduct that subsequently fragments resulting in acyl-carbon cleavage, release of C19 as formic acid and aromatization of the A-ring.

The 'Compound 1 mechanism' (Panel B, Figure 4) represents a more traditional route of catalysis wherein protonation of the peroxoanion generates a ferryl-oxo π-cation radical via an intermediate hydroperoxo anion. The high valent heme-oxygen radical, Cpd 1 abstracts the 1β-hydrogen from the A-ring of its steroid substrate thus initiating aromatization and the deformylation cascade which results in a C10-C19 bond cleavage.

A clear answer as to the mechanism used in the third step of the aromatase reaction has been missing due to conflicting evidence in the field. Non-enzymatic deformylation of 19-oxo-AD mimic by a peroxo-ferric model complex (Wertz et al. 1998) and the use of peroxo-ferric species directly as a reactive intermediate by CYP2B4, CYP17 and CYP51 for C-C cleaving reactions with aldehyde- or ketone-containing substrates, and by nitric oxide synthase (Vaz et al. 1996; Woodward et al. 2009; Shyadehi et al. 1996; Lee-Robichaud et al. 1995) support the 'Cpd 0 mechanism'. However, application of density functional theory (DFT) on a minimal CYP19 active site model showed an strong energetic preference for Cpd 1 mediated hydrogen abstraction from C1 of 19-oxo AD rather than direct reaction of the peroxo-ferric species, or Cpd 0 with 19-oxo AD to produce estrone (Hackett et al. 2005).

Owing to its role in human health, the interesting chemistry it catalyzes and the controversy surrounding the mechanism for the terminal C-C lyase step of aromatase I undertook the task of doing a systematic characterization of the reactive intermediates in CYP19A1 on its path from reactants to products.

EXPRESSION AND PURIFICATION OF CYP19A1

A modified version of human CYP19 having a hexahistidine tag on the C-terminal was expressed in DH5α cells co-expressing the GroES/EL chaperone system. Cells were grown for ~40 hours at 29 °C

in the presence of 1 mM δ-aminolevulinic acid, 1 mM isopropyl β-D-1-thiogalactopyranoside (IPTG) and 4 mg/ml L-arabinose (for induction of GroES/GroEL chaperones). Resuspension of the cell pellet in 100 mM potassium phosphate (KPi) pH 7.4, 50 mM NaCl, 20% glycerol, 10 μM AD, 10 mM β-mercaptoethanol (β-Me) and 0.1 mM phenylmethylsulfonyl fluoride (PMSF) followed by sonication and ultracentrifugation yielded a membrane pellet. Supernatant obtained after solubilization of the membrane pellet in 100 mM KPi pH 7.4, 500 mM NaCl, 20% glycerol, 3 mM Androstenedione, 10 mM β-Me, 0.1 mM PMSF, and 0.1 % cholate and 1 % Tween-20 (Buffer A) and ultracentrifugation was loaded on a Ni-NDA column. The column was washed with buffer A containing 16 mM imidazole and buffer A containing 50 mM imidazole and eluted with buffer A containing 250 mM imidazole. Fractions having R_Z of greater than 0.8 were pooled and dialyzed against 100 mM KPi pH 7.4, 0.1 mM EDTA, 20% glycerol, 0.1% Tween-20, 10 μM AD and 10 mM β-Me at 4 °C. The protein was then concentrated using Amicon centrifugal concentrators of 10,000 MWCO, flash-frozen with liquid nitrogen and stored at -80 °C until further use.

NANODISC TECHNOLOGY TO STABILIZE HUMAN AROMATASE

CYP19A1 is a membrane bound enzyme making the biophysical characterization of this protein outside the membrane environment challenging. The Nanodisc system developed by the Sligar lab provides a solution to this problem through self-assembly of membrane proteins into nanoscale lipid bilayers that maintain full functionality of the protein (Bayburt et al. 2002; Bayburt & Sligar 2003). This provides a soluble, monodisperse, homogenous and stable preparation of membrane proteins to which biophysical and chemical methods can be applied.

Overview of the Nanodisc technology

Nanodiscs are nanometer-sized circular patches of lipid bilayer held together by two strings of amphipathic helices acting as an encircling belt. The amphipathic helices are part of a genetically engineered version of human apolipoprotein A1 referred to as the membrane scaffold protein (MSP). Different versions of MSP (MSP1D1, MSP1E3D1) have been developed with varying number of helices thereby providing control over disc size and therefore, ability to incorporate different sized proteins into Nanodiscs. The amphipathic nature of surrounding belt protein allows the entire assembly to be soluble in aqueous buffer systems. This is truly enabling in the study of membrane proteins since not only do Nanodiscs help stabilize membrane proteins in their native membrane-like environments, they render them soluble in aqueous solutions thus allowing application of a whole slew of biophysical and biochemical tools that would otherwise have been unusable.

Traditional methods of studying membrane proteins include using reconstitution systems such as mixed detergents, lipid micelles and liposomes. Micelles do not contain a lipid bilayer and therefore, do not represent the membrane protein's native environment very well. Lipid vesicles and liposomes are better in this regard but offer no control over stoichiometry, oligomerization state or local lipid environment of the membrane protein target. Nanodiscs surmount all these problems and have been successfully applied to mechanistic investigations of variety of membrane proteins such as cytochrome P450s (Denisov & Sligar 2011), ion channels (Shenkarev et al. 2010), G-protein coupled receptors (Leitz et al. 2006) and transporters (Ritchie et al. 2009). Some examples highlighting the advances that the use of Nanodisc technology has enabled in these systems are listed below:

- By providing precise control over the oligomerization state of incorporated protein target, Nanodiscs have helped identify the functional unit of chemotactic receptors (Li & Hazelbauer 2011; Boldog et al. 2006)
- By providing stable and homogenous enzyme preparations, Nanodiscs have facilitated:
    - The characterization of microscopic rate constants and binding intermediates of CYP3A4, a critical xenobiotic metabolizing human hepatic P450, that can bind up to three different substrate molecules. This has implications in drug-drug interactions for eliminating undesirable side-effects of drugs, especially in patients following a regimen of multiple lifestyle and/or disease management drugs (Denisov et al. *Unpublished work*)
    - Stabilization of transient intermediates of membrane-bound P450s such as CYP17 and CYP19 (the subject of this thesis) for spectroscopic analysis (Gantt et al. 2009; Luthra et al. 2011b).
- By providing a means to precisely control the local lipid environment of membrane proteins Nanodiscs have helped unravel the minutiae of recruitment and assembly of protein-protein complexes central to the blood coagulation cascade in humans. (Morrissey et al. 2008; Morrissey et al. 2011)

Marriage of Nanodisc technology with detection modalities such as nuclear magnetic resonance spectroscopy (NMR) (Kijac et al. 2007; Glück et al. 2009), surface plasmon resonance spectroscopy (SPR) (Borch et al. 2008; Glück et al. 2011), mass spectrometry (Marty et al. 2012), ring resonators (Sloan et al. 2013) and microscale thermophoresis (Singh et al. 2013) widens the scope of analytical tools that may be applied to study various aspects of a membrane protein biochemistry such as

ligand binding, protein structure, protein-protein and protein-lipid interaction with exceptional fidelity.

The experiments described in this thesis rely on the ability to produce stable, fully functional ligand (substrate, oxygen)–iron complexes that would be amicable to various spectroscopic methods. Nanodiscs by providing a native-like membrane bilayer environment and eliminating the need for detergents, liposomes etc. satisfy both these requirements.

Incorporation of CYP19A1 into Nanodiscs

Nanodiscs are formed by the process of self-assembly upon removal of detergent from a reconstitution mixture comprising of MSP, lipids and membrane protein target solubilized in a detergent of choice using dialysis or hydrophobic beads. The relative amounts and concentration of lipids, detergent, target protein are critical in ensuring a successful incorporation of the protein target in Nanodiscs. A detailed description of the protocol followed for incorporating CYP19 into Nanodiscs follows:

A stable preparation of CYP19A1 was obtained by incorporating it into MSP1D1-POPC Nanodiscs using the protocol described in (Luthra et al. 2013). Briefly, 1-palmitoyl-2-oleoyl-sn-glycero-3-phosphocholine (POPC) was dried in 18-ml glass culture tube from a chloroform stock under stream of nitrogen so as to deposit a thin layer of dried lipids on the sides of the glass culture tubes. Remaining chloroform was removed by placing the tubes inside a vacuum desiccator for 4-6 hours. Once completely dried, the lipids were dissolved in 100 mM sodium cholate to achieve a final lipid concentration of 50 mM. Disc reconstitution mixture was prepared, targeting a POPC:MSP1D1:CYP19A1 ratio of 1300:20:1 and final POPC concentration of 6-7 mM. It was incubated on ice for 15 minutes after which 1-ml equivalent of hydrophobic beads (Amberlite XAD-2) was added per ml of solution with the help of a 10-ml plastic syringe with its luer-lock connection cut off. The tube was then placed on a shaker platform for 6 hours at 4 °C. Protein solution containing empty and membrane protein containing discs was separated from the slurry by passing it through a filter column. The spent beads were rinsed with one volume of 100 mM KPi pH 7.4 thrice and the wash solution added to the pool. Discs with CYP19 incorporated in them were then separated from empty discs by nickel affinity chromatography taking advantage of the His-tag on CYP19. The eluent from the Ni-NTA column was concentrated using 4-ml Amicon centrifugal concentrators of 10,000 MWCO and purified using size-exclusion chromatography. The desired fractions from SEC were pooled and concentrated. 15% (v/v) ultra-pure glycerol (Sigma-Aldrich) was added to CYP19A1 discs, the entire solution flash-frozen and stored at -80 °C until further use.

Figure 5 contains a schematic representation of the disc assembly process of CYP19A1 into Nanodiscs.

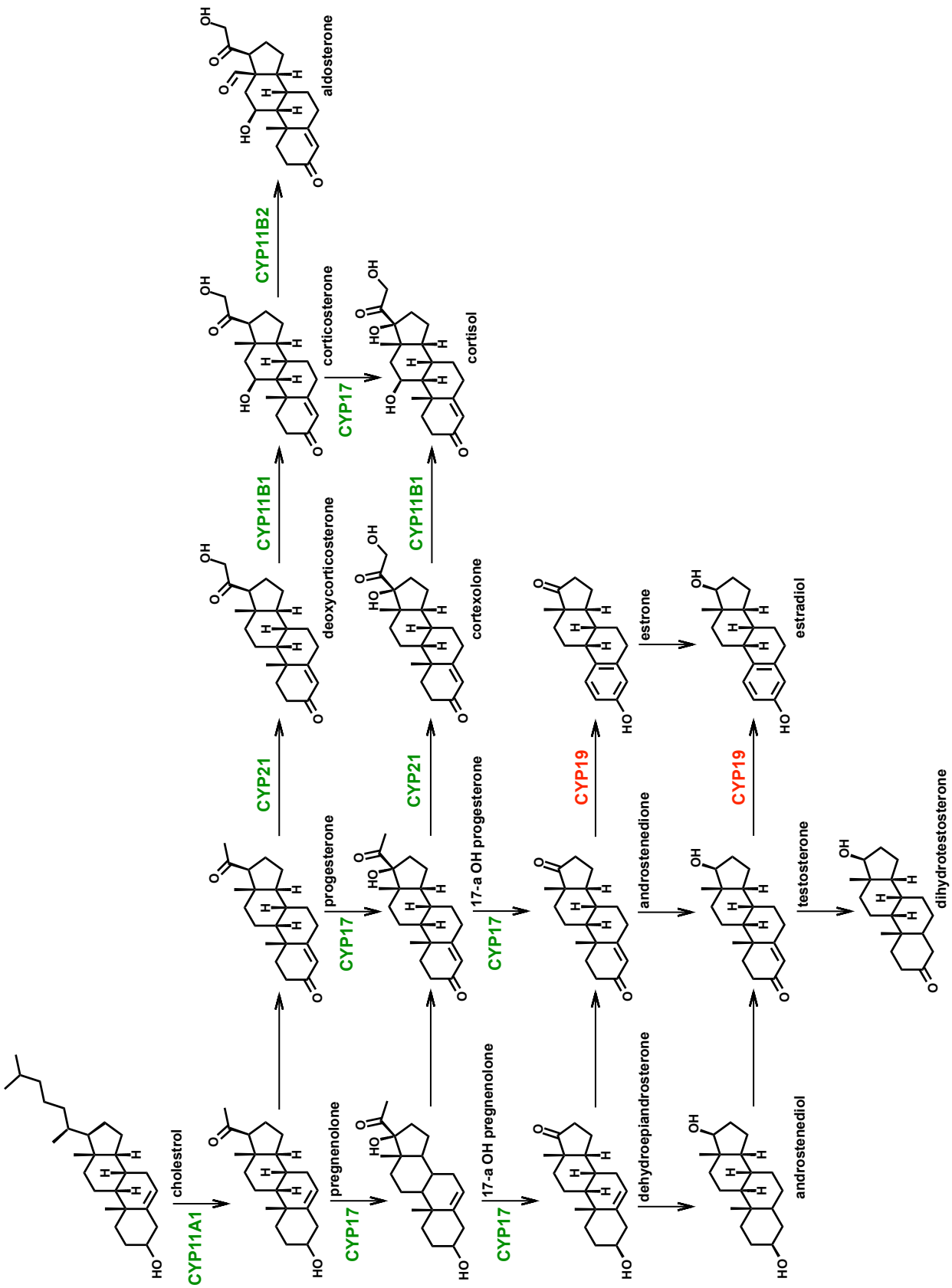

Figure 1. Human steroidogenic pathway showing the role of various P450s, especially CYP19A1.

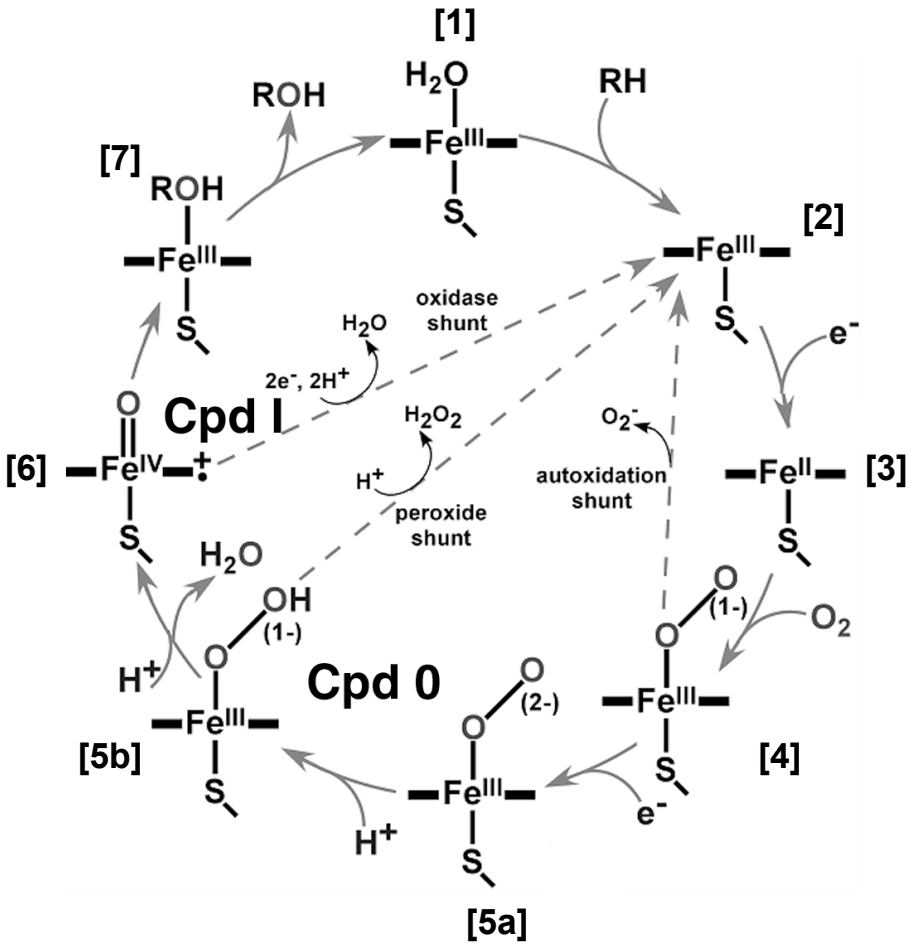

Figure 2: The P450 catalytic wheel

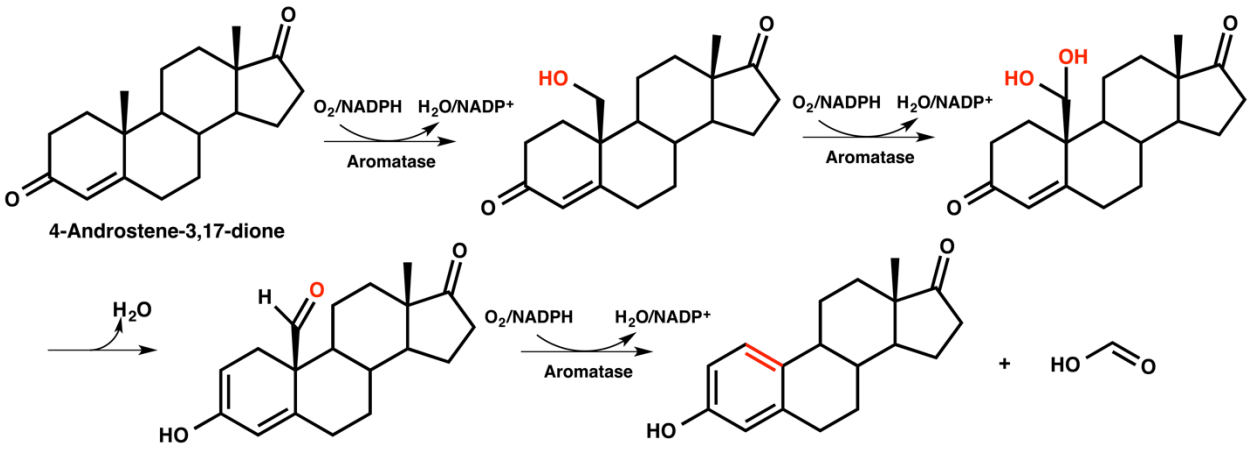

Figure 3: Conversion of Androstenedione to Estrone by CYP19A1. Red marks the modifications introduced into the steroid molecule by the action of CYP19A1

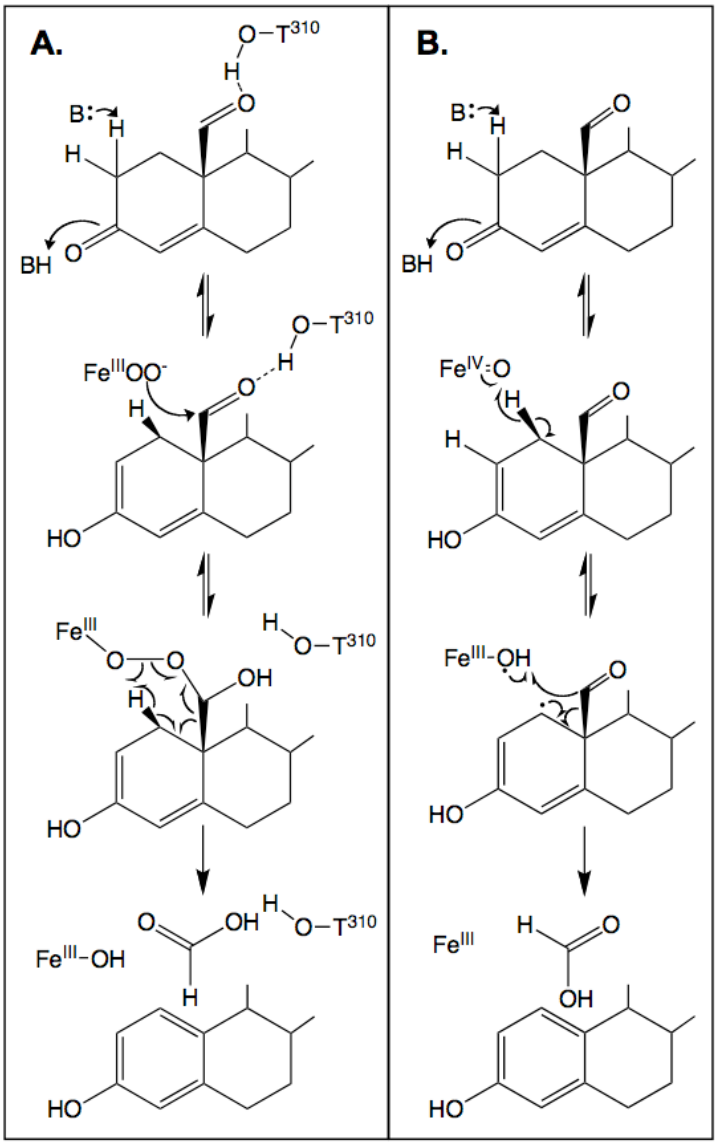

Figure 4: Proposed hypothesis for the lyase chemistry of CYP19A1. A. 'Compound 0' mechanism and B. 'Compound 1' mechanism'.

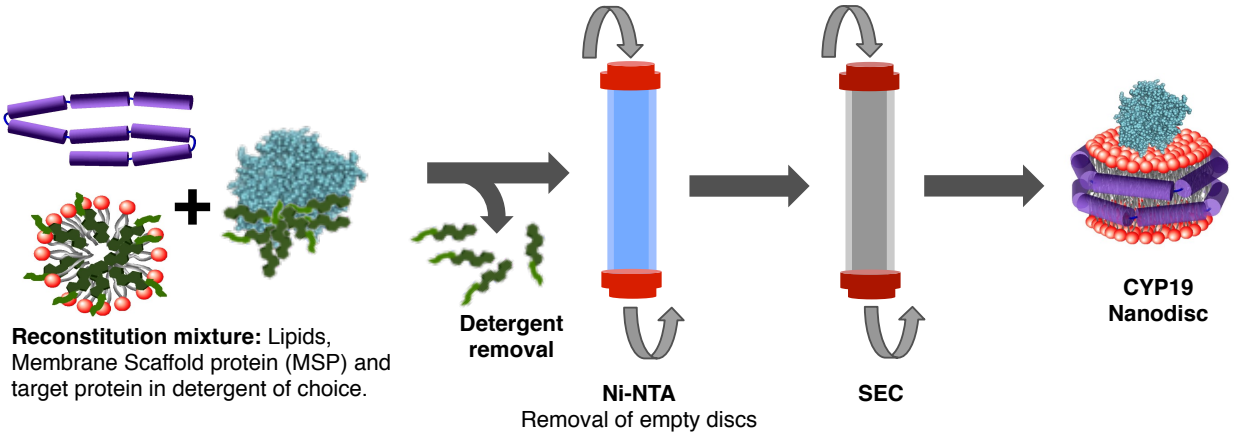

Figure 5: Schematic representation of the disc assembly process.

Chapter 2: Temperature Derivative Spectroscopy (TDS) To Monitor Autoxidation In Cytochromes P450

INTRODUCTION

Temperature derivative spectroscopy (TDS) (Berendzen & Braunstein 1990) is a type of relaxation spectroscopy that involves a temperature-dependent "perturbation" and a corresponding "observable". The perturbation may be the formation or decay of a molecular species by photolysis, ligand binding, or a mere change in temperature. The list of observables that may be used with TDS includes Raman scattering, circular dichroism, fluorescence anisotropy, and UV-Vis absorption spectroscopy. Previously, TDS has been used extensively to study various aspects of ligand binding and dynamics in myoglobin (Nienhaus et al. 1994) and neuroglobin (Kriegl et al. 2002). Here TDS has been adapted to characterize the energetics of autoxidation in cytochromes P450s. Autoxidation is the first major uncoupling pathway in P450s wherein the oxy-ferrous complex loses the bound oxygen as superoxide anion and oxidizes back to the ferric state. This results in the net wasteful expenditure of one reducing equivalent.

The autoxidation shunt constitutes the major unproductive pathway for many P450s and thus its quantitation and mechanism of action are of interest to pharmacologists, toxicologists, and biochemists. Autoxidation is intimately coupled to the redox potential of heme iron in these enzyme systems (Clark et al. 2006), and different substrates exercise their control on the rates of autoxidation primarily by modulating the midpoint reduction potential of the heme iron. The rates of autoxidation in P450s range from 0.005 s^{-1} in camphor-bound CYP101 (Lipscomb et al. 1976) to 20 s^{-1} in substrate-free CYP3A4 at 5 °C (Denisov et al. 2006). It is known that the autoxidation shunt accounts for a major fraction of reactive oxygen species (ROS) in mammalian P450 CYP11A1, both in vivo and in vitro (Derouet-Hümbert et al. 2005), and this can lead to the induction of apoptosis in cells. The oxy-ferrous complexes of various cytochromes P450 have been characterized spectroscopically (Luthra et al. 2011a). However, the more physiologically relevant information is the autoxidation rates and the energy of activation for the conversion of the oxy-ferrous complex into the ferric resting state of the enzyme. The most commonly used method to investigate the autoxidation of cytochromes P450 in the 0.01-10 s time range is stopped-flow spectroscopy. However, this requires special equipment and substantial amounts of enzyme which normally

cannot be recovered after experiments. Alternatively, TDS provides a relatively easy and quick method to obtain the same information using a regular slow scanning spectrophotometer and an easily assembled optical cryostat. Because the measurements are done at lower temperatures, where all reaction rates are dramatically slowed, TDS makes possible studies of fast reactions without the need of expensive instrumentation. The Nanodisc technology allows the same method to be used with the membrane proteins solubilized in the native bilayer environment at a known oligomerization state (Bayburt & Sligar 2010). In monitoring autoxidation using TDS, the perturbation and the observable are the decay of oxy-P450 and the spectral changes in the UV-vis region induced by conversion of the oxy-ferrous complex to the ferric form.

MATERIALS AND METHODS

Expression and purification of CYP101

Expression of CYP101 in *Escherichia coli* (*E. coli*) and protein purification were performed as described in (Makris et al. 2007). Mutagenesis of the CYP101 gene (pCamT7) was performed using Stratagene Quikchange kit following the manufacturer's directions. The CYP101 gene with a hexa-histidine tag added at the C-terminal (pT7-P450 His) was expressed in BL21 (DE3) cells (Stratagene) and grown overnight in the presence of 0.5 mM δ-aminolevulinic acid. After cell sonication, resuspension in 50 mM KPi, pH 7.4, containing 150mM KCl (buffer A), and ultracentrifugation, the protein extract was loaded on a Ni-NTA column (Amersham), washed with buffer A in the presence of 50 mM imidazole, and eluted with the same buffer supplemented with 20 mM ethylenediaminetetraacetic acid (EDTA). The red fractions in the eluent were dialyzed against 50 mM KPi, 400 μM D-camphor, and 20 mM β-mercaptoethanol, pH 7.4, overnight at 4 °C. Solid ammonium sulfate was added to 30% saturation over 30 min, and the protein was subsequently loaded onto a phenyl–sepharose CL6B column equilibrated in the same buffer and eluted in a linear gradient from 30 to 0% ammonium sulfate. Resulting fractions with an R_z-value (A_{392}/ A_{280}) greater than 1.45 were judged as pure and concentrated using an Amicon cell.

Expression, purification and Nanodisc incorporation of CYP19A1

The expression, purification and incorporation of CYP19A1 into POPC Nanodiscs was performed as previously described on pages 7 and 10.

Preparing oxy-samples for optical spectroscopy

A 60 μl aliquot of a mixture of 100 μM CYP19A1 in 1-palmitoyl-2-oleoylphosphatidylcholine (POPC) Nanodiscs, 125 μM 4-androstenedione (obtained from Sigma) and 2.5 μM methylviologen in 100 mM phosphate buffer, pH 7.4, was taken in a small glass vial with a poly(tetrafluoroethylene) (PTFE)/Red rubber septa (SUPELCO) and deoxygenated by argon, under rotation, for 3–4 min. Separately, 540 μl of a solution containing 75% glycerol, 125 μM substrate, and 100 mM phosphate buffer, pH 7.4, was prepared in a methacrylate cuvette (4.3 mm path length UV-enhanced semi-microcells, Fisher) and saturated using pure oxygen by bubbling and occasional stirring for 15 min. Concentrated CYP19A1 with 125 μM AD, methylviologen (MV:CYP19A1 molar ratio of 1:50), 100 mM KPi, pH 7.4, and 15% glycerol was deoxygenated and reduced with 2.5 Molar equivalents of dithionite in a Coy Laboratories anaerobic glovebox. Dithionite concentration was determined using its molar absorption coefficient of 8.05 $mM^{-1}cm^{-1}$ at 315 nm (McKenna et al. 1991). To form the oxy–ferrous complex, the reduced AD–bound CYP19 sample in glycerol was manually injected into a solution of aerobic glycerol containing buffer precooled to 243 K, mixed for 45 seconds, transferred to a 200 K dry ice/ethanol bath, and stored in liquid nitrogen before further use. The same procedure was used to form the oxy complex of soluble CYP101, except no methylviologen was used.

Thermal annealing instrumentation

The experiments were performed in a home-built cryostat setup previously described in (Denisov et al. 2002). The cyrostat comprises an unsilvered Pyrex glass dewar that is transparent to wavelengths above 300 nm. A holder attached to the top cover of the dewar houses the cuvette during the experiment. Prior to beginning the experiment, the dewar is precooled to 200 K using liquid nitrogen at the bottomof the dewar, added through a plastic funnel attached to the top cover of the dewar. The sample is never in direct contact with liquid nitrogen to prevent cracks and maintain the optical transparency. A thermocouple in contact with the sample solution was used to monitor the temperature of the sample during measurement. Figure 6 shows the cryostat setup with its various components labeled.

Choosing an optimal temperature ramping rate

For a first-order reaction involving conversion of a species S to product P the rate of disappearance of S can be calculated using the Arrhenius equation and represented mathematically as,

$$\frac{dS}{dt} = -\left(A.exp\left(-E_a/_{RT}\right)\right).S \quad [1]$$

Rearranging, we get

$$\frac{dS}{S} = -A.exp\left(-E_a/_{RT}\right).dt \quad [2]$$

For a linear temperature-time dependence, dT = mdt. Here, m is the slope of the temperature-time profile. Substituting for dt and integrating within proper limits, we get

$$\int_S^0 \frac{dS}{S} = -\frac{1}{m}.\int_{T_1}^{T_2} A.exp\left(-E_a/_{RT}\right).dT \quad [3]$$

Figure 7 contains a series of calculated curves depicting the decay of the oxy-ferrous complex, generated using [3] with an Arrhenius activation energy of 18 kcal/mol and varying ramp rates. This graph illustrates how the ramping rate influences the time span of an experiment and, therefore, the number of data points available for analysis. The number of available data points is determined by the ability of the instrumentation to record high quality spectra at the rate of data acquisition which defines the level of accuracy in extracting parameters such as E_a (activation energy) and kT (rate of autoxidation at a particular temperature). For instance, at the scanning rate 600 nm/min, one can measure the full spectrum in the range of 750 to 300 min in 1 min, which corresponds to one spectrum per kelvin at a temperature ramping rate of 1 K/min.

Data acquisition

All UV-vis absorption spectra were acquired with a Cary 300 Bio UV-visible spectrophotometer. (Varian Instruments), in a continuous scan mode, at a scan rate of 600 nm/min and a 45-second gap between scans. A thermocouple inserted into the sample cuvette was used to monitor temperature. Temperature readings were noted at the start and end of each UV-vis scan and averaged for analysis.

Data analysis

The raw spectral data from the spectrophotometer were first corrected for baseline shifts between scans by subtracting the average absorbance at 595-600 nm of each spectrum. The baseline-corrected and time-dependent data were analyzed by a singular value decomposition (SVD) routine in MATLAB to identify the eigenvectors and eigenvalues of the reaction. SVD is a linear-algebra

technique that allows one to determine the number of spectrally distinguishable components that are involved in a reaction and to extract maximum information about the transition between these species from experimental data set. Figure 8(a) shows the TDS data for AD-bound CYP19 reconstructed using the first two eigenvectors. Isosbestic points show a single transition, which is the decomposition of the oxy-ferrous complex into the ferric resting state. The small drift at the isosbestic point at 408 nm is due to the temperature-dependent changes of the band shape of both components, i.e., substantial narrowing and sharpening of Soret bands at low temperatures. Figure 8(b) shows the first four abstract absorption spectra multiplied by their corresponding singular values for the autoxidation of P450. Only the first two main spectral components are significant, with others being close to zero. This clearly indicates, along with isosbestic points in the raw data, the presence of only two major absorbing species in the data set. Hence, the second concentration vector from SVD is a measure of disappearance of the oxy-ferrous complex or appearance of the ferric complex. These difference spectra were normalized and fitted to a modified rate equation derived on the basis of the Kramers' theory to account for variable temperature (equation [4]). The time and temperature increments were used directly as time steps for integration.

Fitting the concentration profile to the TDS equation

The autoxidation of oxy-CYP101 and oxy-CYP19A1 in their substrate bound states can be modeled as a first-order reaction. For reactions occurring in the high-friction/ high-viscosity regime, a modified Kramers' theory (Yedgar et al. 1995) provides a good description of the reaction kinetics where the rate constant for a biochemical reaction can be expressed as:

$$k = \frac{A}{\eta^p} exp\left(-E_a/_{RT}\right) \qquad [4]$$

Here, A is a frequency (or pre-exponential) factor, η, the solvent viscosity and Ea, R and T, the Arrhenius activation energy, gas constant and temperature (in Kelvin) respectively. p is an empirical exponent smaller than unity, which has been shown to be related to the molecular weight of the cosolvent in question and estimated as 0.54 for glycerol (Yedgar et al. 1995).

Samples prepared for TDS contain 70% glycerol and are hence, highly viscous. Since autoxidation involves a dynamic process of opening of the active site to release the superoxide anion, the phenomenon is affected by the viscosity of the solution. It is well known that viscosity of pure liquids and their mixtures depend on temperature and pressure. Very recently, González *et al.* (Gonzalez et al. 2011) proposed an equation for calculation of the dynamic viscosity of aqueous-

glycerol mixtures over a wide range of temperatures and compositions. In fitting the TDS data, a value of 0.65 was used as the weight fraction of glycerol.

Using p as 0.54, and the model for temperature dependence of viscosity proposed by González *et al*. (Gonzalez et al. 2011)the TDS data for autoxidation decay of the oxy-ferrous complex for camphor-bound CYP101 and AD-bound-CYP19A1 was fitted to the equation [6] in the form given below.

For a first-order reaction involving decay of species S (representing the oxy-complex of cytochrome P450),

$$k = \frac{A}{\eta^p} exp\left({}^{-E_a}/_{RT}\right) \qquad [5]$$

$$\frac{dS}{dt} = -k.S$$

$$k = \frac{C}{\eta^p} exp\left({}^{-E_a}/_{RT}\right)$$

$$\frac{dS}{dt} = -\frac{C}{\eta^p} exp\left({}^{-E_a}/_{RT}\right).S \qquad (a)$$

The rate constant '*k*' can be alternatively expressed as,

$$k = \frac{C}{\eta^p} exp\left({}^{-E_a}/_{RT}\right) = \left(\frac{k_{298K}.\eta_{298K}^p}{\eta^p}\right).exp\left(\frac{-E_a}{RT}\left(\frac{298-T}{298}\right)\right) \qquad (b)$$

From (a) and (b),

$$\frac{dS}{S} = -\left(\frac{k_{298K}.\eta_{298K}^p}{\eta^p}\right).exp\left(\frac{-E_a}{RT}\left(\frac{298-T}{298}\right)\right)dt$$

Integrating within proper limits for S and T we get,

$$\int_S^0 \frac{dS}{S} = -\left(\int_{T_1}^{T_2}\left(\frac{k_{298K}.\eta_{298K}^p}{\eta^p}\right).exp\left(\frac{-E_a}{RT}\left(\frac{298-T}{298}\right)\right)dT\right).\frac{dt}{dT} \qquad [6]$$

Fitting was accomplished with a program written in MATLAB, using the subroutine 'fminsearch.m' that implements the Nelder-Mead Simplex algorithm to find the minimum of a multiparametric, non-linear function.

RESULTS AND DISCUSSION

As shown in Figure 8(a), the starting spectra of oxygenated CYP19A1 in 70% glycerol are almost identical to those previously measured using either stopped flow (Grinkova et al. 2008) or cryospectroscopy (Gantt et al. 2009). At 220 - 230 K the rate of autoxidation is very low, and the oxy-complex remains stable. As the temperature increases, the rate of autoxidation also increases, and the oxy-ferrous complex starts to decompose, as shown in Figure 8(c). When the temperature reaches 260 K, the rate of autoxidation becomes high enough to change significantly the fraction of oxy-complex during the time of single scan (45 s). The curve shown in Figure 8(c) reaches zero at 285 K, where all of the oxy-CYP19A1 returns to the high-spin ferric form, as seen from Figure 8(a).

The energy of activation for the conversion of oxy-ferrous CYP19A1, saturated with androstenedione, to ferric CYP19A1 was calculated to be 17.5 kcal/mol with a rate constant of 0.02 s^{-1} at 298 K (Figure 8(c)). In the case of CYP101, saturated with camphor, this value was determined to be 18.0 kcal/mole with a rate constant of 0.015 s^{-1} at 298 K (Figure 9(d)). The values of E_a obtained, in both cases, correspond well with those published earlier (Lipscomb et al. 1976; Grinkova et al. 2008). The results obtained using TDS approach with a single sample match almost exactly the parameters derived in earlier stopped-flow studies, which confirms the validity of TDS approach to the autoxidation processes in heme enzymes.

Cytochromes P450s do not possess a static channel for the access of O_2 to the active site. Therefore, the protein has to undergo a conformational change to form a dynamic path for the entry and egress of ligands such as O_2 and CO. The high activation energy barrier for autoxidation (17 kcal/ mol for camphor-bound-CYP101(Lipscomb et al. 1976) and 18 kcal/mol in AD-bound-CYP19A1 (Grinkova et al. 2008)) reinforce this idea. An even higher activation energy, 22 kcal/mol was reported for the autoxidation of CYP11A1, another P450 involved in steroid hormone biosynthesis (Tuckey & Kamin 1982), although this measurement was made in the presence of 38% ethylene glycol at subzero temperatures and was not corrected for high viscosity.

As described in Materials in Methods, absolute rates of enzymatic catalysis usually depend on the solvent viscosity. The first attempts to include viscosity into the Kramers' approach to describe biochemical reactions yielded an inverse dependence of the rate of a reaction on viscosity (i.e. p = 1) (Gavish 1978) . This approach was tested for hydrolysis catalyzed by carboxypeptidase (Gavish & Werber 1979), and later for the variety of processes such as oxygen escape from myoglobin (Beece et al. 1980) and hemerythin (Lavalette et al. 1979), ester hydrolysis by subtilisin (Ng & Rosenberg 1991), photocycle of bacteriorhodopsin (Beece et al. 1981) and hydrogen isotope

exchange in lysozyme and in other proteins (Rosenberg et al. 1989; Somogyi et al. 1988). In all these experiments it was observed that biochemical reactions that take place within a protein matrix are sensitive to the viscosity of the solvent, especially at high viscosities, and that in most cases a fractional power ($p < 1$) describes the process. In a systematic study of many solvents, Yedgar et al. (Yedgar et al. 1995) have shown that the effect of solvent viscosity on the escape of oxygen from hemerythrin follows the power-law with p dependent on the molecular weight of the cosolvent. This relation can be expressed as:

$$p(M) = 1.52M^{-0.23} \quad [7]$$

where, M is the molecular weight (in Daltons) of the cosolvent. For glycerol, M = 92 and therefore, p = 0.54. This empirical value is also the value that the authors determined experimentally.

Temperature dependence of viscosity

Our TDS experiment samples temperatures from 230K to 290 K. In this range, the viscosity of water-glycerol mixtures strongly depends on temperature (Gonzalez et al. 2011). There are various models that attempt to correlate viscosity-temperature data of pure liquids and liquid-solutions starting from the simple Arrhenius type models (Andrade 1934) to more elaborate and complex empirical fits (Cheng 2008; Chen & Pearlstein 1987). Most of these models have been derived from fitting experimental data for the viscosity of aqueous glycerol solutions at temperatures between 253 K and above. These models often fail when used to make predictions outside their validity limit. We used the equation derived by Trejo González *et al*. (Gonzalez et al. 2011), which uses the general Aramov-Michev equation (Avramov 2005) to model viscosity data of glycerol aqueous solutions in the entire range of compositions, $0 \leq w_2 \leq 1$ and which also provides equations for the composition dependence of the parameters in this equation. This approach was also shown to be applicable over a wide range of temperatures including the supercooled region of water and glycerol where other methods of predicting the viscosity-temperature relationship fail. The equations used for calculating viscosity of the glycerol-water mixture used are:

$$\eta = \eta^0 exp\left[(28.75 - \ln \eta^0)\left(\frac{T_g}{T}\right)^{\alpha}\right] \quad [8]$$

Where, T_g is the glass transition temperature of the liquid solution. η_0, T_g and α were expressed as a functions of the weight fraction of glycerol (w_2) in the solution as:

$$T_g(K) = 140.3 + 35.272\, w_2 - 3.879\, w_2^2 + 23.467\, w_2^3 \quad [9]$$

$$-\ln(\eta_0\ /mPa.s) = 2.1686 - 2.7096\, w_2 + 1.4449\, w_2^2 \quad [10]$$

$$\alpha = 3.6344 + 1.2198\, w_2 - 1.6142\, w_2^2 \quad [11]$$

If not corrected for, temperature dependence of η contributes ~5 kcal/mol to the observed energy barrier as seen by Gavish and Werber while studying the rate of catalysis of carboxypeptidase in different cosolvent mixture (Gavish & Werber 1979). Fitting the TDS data reported in this paper to the simple Arrhenius equation, not accounting for viscosity of solution or its temperature dependence, yields the same result.

A value of 0.65 was used as the weight fraction of glycerol instead of 0.75 that would result if one calculated the weight fraction of glycerol in a 70% (v/v) glycerol-water mixture. The presence of glycerol preferentially hydrates protein molecules and results in a higher than average content of water in the hydration shell of the protein (Sinibaldi et al. 2007). Preferential hydration in the presence of glycerol and ethylene glycol is known to stabilize the activity of enzymes and retain the native structure of proteins (Gekko & Timasheff 1981). For a 75% w/w glycerol-water mixture the amount of glycerol present in the local domain of the protein molecule is approximately 65% (Sinibaldi et al. 2007).

Intracellular microviscosity is an important regulator of cellular functions and membrane enzyme activity (Kuimova et al. 2009). The analysis developed in this work, integrating the two important parameters of temperature and viscosity, not only gives a full Arrhenius dependence of the also provides a way to calculate rates of autoxidation of oxy-P450s in different cellular milieu. Importantly, high viscosity has a profound effect on the rates of autoxidation, and in some cases this can affect the stability of oxy-ferrous intermediate in membrane bound cytochromes P450 and overall uncoupling of P450 catalysis.

Apart from being quick, this technique offers high precision, in terms of agreement between experimental data and the theoretical model of autoxidation decay, as well as high accuracy, as evident from the comparison of E_a values obtained with this methodology and that obtained by other approaches. TDS gives spectral data corresponding to a finely spaced, wide range of temperatures, the eigenvalues and eigenvectors obtained from SVD analysis are more robust than that obtained from the SVD analysis of spectral data sets at five to six temperature points in a

typical stopped-flow experiment. TDS also gives the complete Arrhenius dependence of the autoxidation process in a single experiment, using very little sample.

CONCLUSION

TDS provides a rapid, robust and a convenient method to measure decay kinetics of oxy-ferrous complexes in cytochromes P450. Using this method, the full Arrhenius dependence of the autoxidation process can be measured in a single experiment, with relatively little sample. Furthermore, the sample is completely recoverable unlike in stopped-flow. By integrating data analysis with data acquisition the method described has the potential to be developed into a semi-automatic way to characterize the oxy-ferrous complex in heme proteins. The concept, in general, can be applied to any temperature-dependent process, the 'observable' varying from absorption spectra, as illustrated here, to other parameters such as mid-point reduction potential and pH.

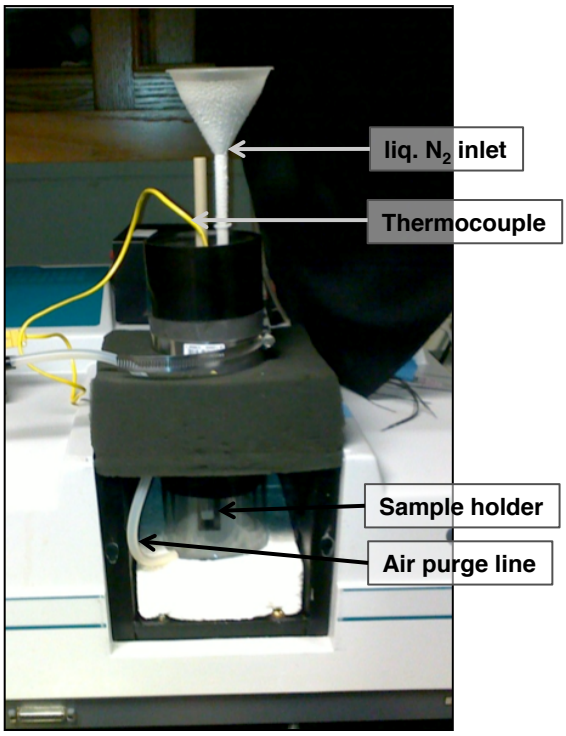

Figure 6: Home-built cryostat setup for measuring autoxidation via temperature derivative spectroscopy

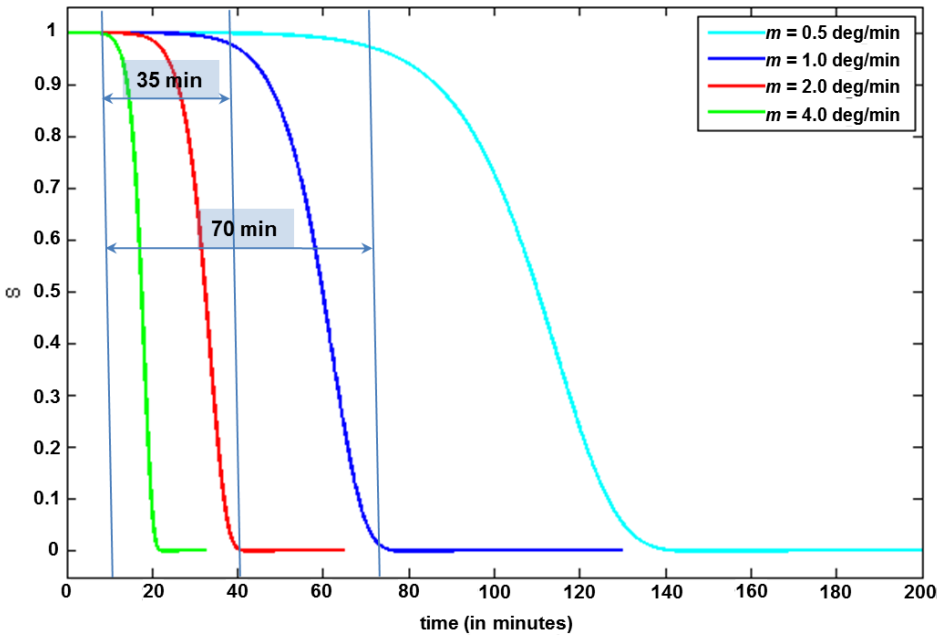

Figure 7: Theoretical curves depicting the effect of temperature ramp rate on the shape of the concentration profile. All curves were generated assuming an 18 kcal/mol Arrhenius activation energy

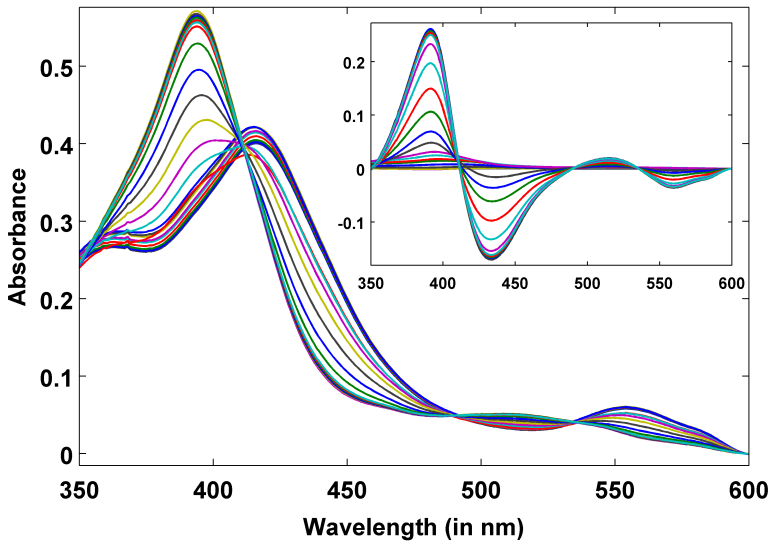

Figure 8: (a) SVD reconstructed TDS data for AD-bound CYP19. Inset: Difference spectra corresponding to the same data set. Both sets of spectra show clear transition from the oxy-ferrous complex to the ferric resting state.

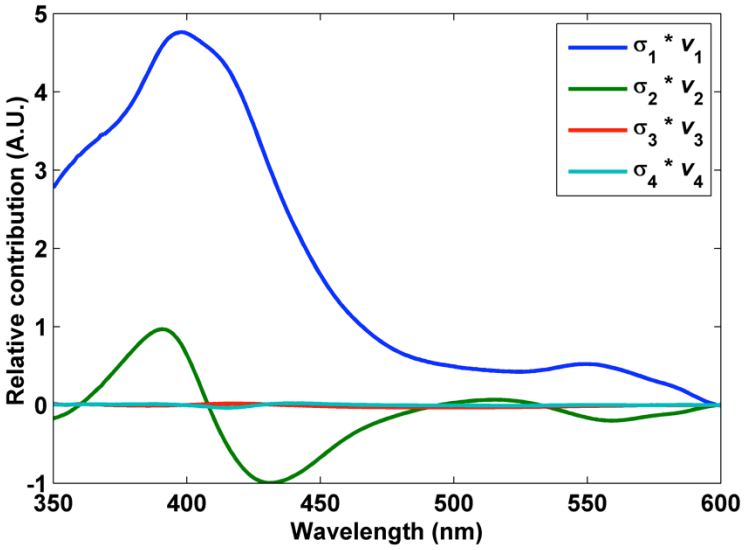

(b) Eigenvectors from singular value decomposition (SVD) of TDS data for AD-bound CYP19, normalized with respect to the corresponding eigenvalues.

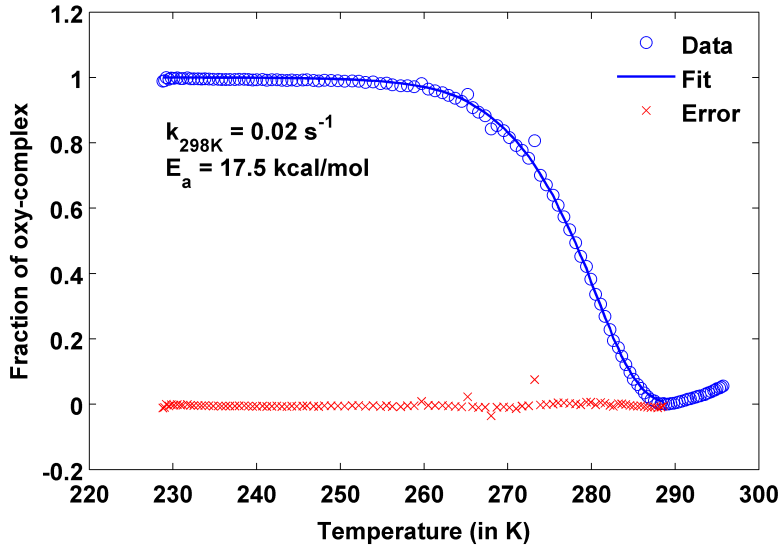

(c) Decomposition of the oxy-ferrous complex of AD-bound CYP19 via autoxidation fitted to a rate equation based on Kramers' theory with viscosity corrections. The uptick toward the end of the experiment, as seen in the figure, could be due to light scattering. Condensation of water molecules on the walls of the cuvette and changes in turbidity of the sample solution with rise in temperature contribute to this effect

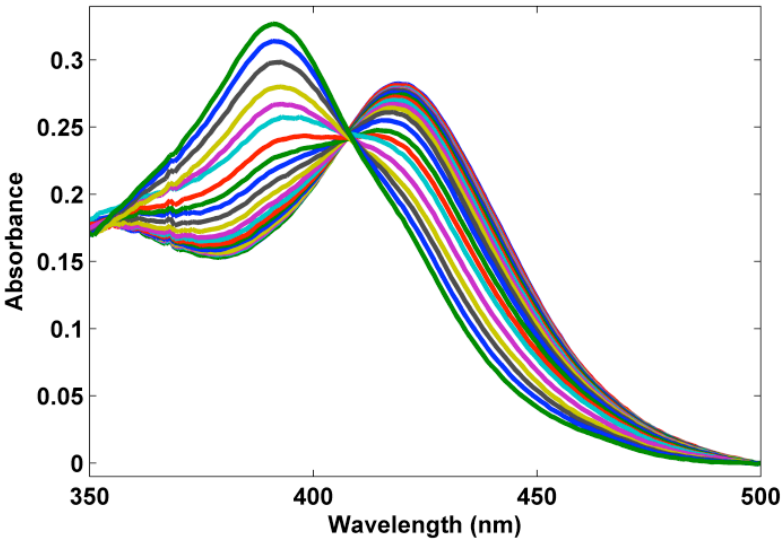

Figure 9: (a) SVD reconstructed TDS data for camphor-bound CYP101.

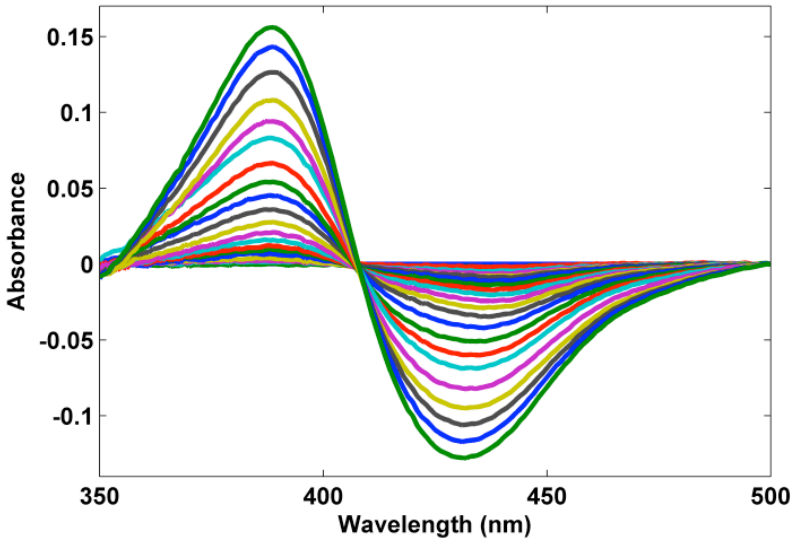

(b) Difference spectra corresponding to the same data set. Both sets of spectra show clear transition from the oxy-ferrous complex to the ferric resting state.

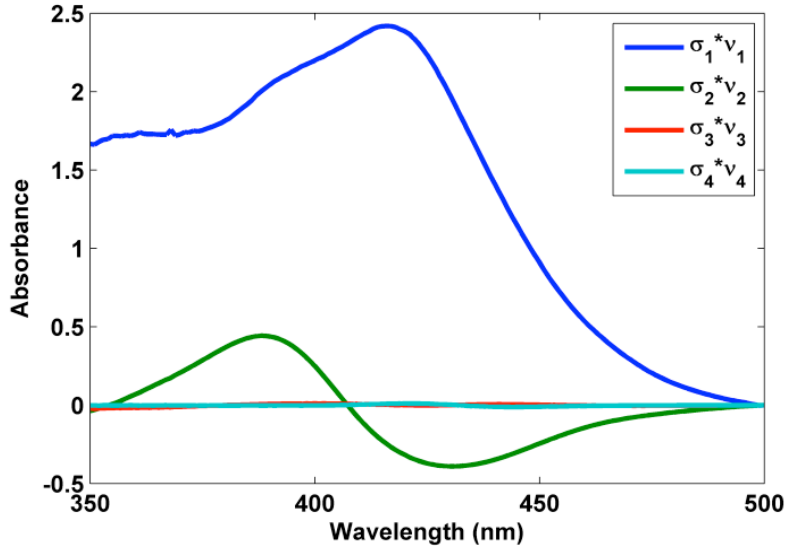

(c) Eigenvectors from singular value decomposition (SVD) of TDS data for camphor-bound CYP101, normalized with respect to the corresponding eigenvalues.

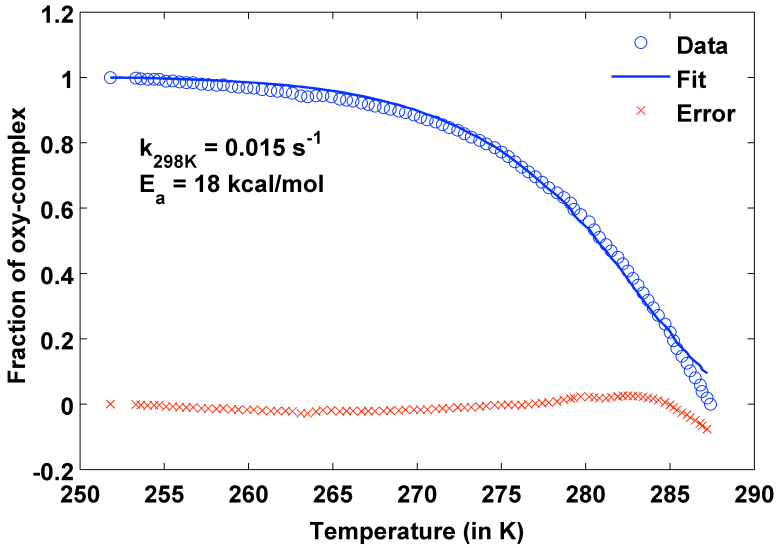

(d) Decomposition of the oxy-ferrous complex of camphor-bound CYP101 via autoxidation fitted to a rate equation based on Kramers' theory with viscosity corrections. The systematic deviations for the P450cam data in Figure S4 may be due to a small fraction of substrate-free P450cam in the experiment which autoxidizes at a higher rate. This can be estimated as being less than 5% from the slight deviation of the fit from experimental data at low temperatures. For this particular experiment we did not gather data above 16 °C. More data points obtained at higher temperatures i.e. the flat region of the curve, would remove this systematic deviation as shown in Figure 3c.

Chapter 3: TDS to study protein dynamics in P450s

INTRODUCTION

The previous chapter presented the application of temperature derivative spectroscopy to monitor autoxidation in cytochromes P450 (Luthra et al. 2011b). TDS was used to characterize the energetics of conversion of oxy-ferrous states of substrate bound CYP19 and CYP101 into the corresponding ferric states. This chapter outlines the implementation of TDS to study other key processes in the P450 catalytic cycle, namely, high-spin low-spin relaxation, binding of a diatomic ligand and decay of the reduced oxy-ferrous complex.

These three processes have been studied at temperatures below the glass transition of aqueous-glycerol solutions used to prepare the samples. In this temperature range protein motion is frozen and the heterogeneity of the protein's energy landscape becomes consequential. One way to describe this mathematically is by using a normal distribution, where the activation energy is described as a Gaussian distribution described by a peak enthalpy, H_P and a standard variance in distribution, σ. These concepts are discussed in more detail below:

Protein flexibility and rigidity

For a long time after X-ray crystallography enabled the determination of 3-dimensional structures of protein molecules it was thought that each protein molecule assumed a unique molecular structure that gave it its functional characteristics. This view held its ground until 1959, when Linderstrøm-Lang & Schellman based on studies of hydrogen/deuterium exchange in proteins concluded that proteins exist as a group of similar structures having comparable free energies and that a protein molecule must be thought of as trying out every possible structure rather than possessing a unique structure (Linderstrøm–Lang & Schellman 1959). Both these points of view are valid in their own right. We now know that proteins reside the space between these two extremes of flexibility and rigidity favored by deuterium exchange experiments and X-ray crystallography respectively and that both these aspects are absolutely important for proper function.

Origin of conformational substates

Proteins are polypeptides held together by strong covalent bonds that are organized into secondary structure elements such as helices, sheets and coils, which in turn are assembled into unique

tertiary and quaternary structures. The biological function of a protein molecule is intimately related to its structure and therefore, proper folding is critical for biological activity. Secondary structure formation and its higher order organization is governed by weak forces such as H-bonds, van der Waals forces and other non-covalent interactions. Although the overall 3-dimensional structure of a protein is unique and depends on its primary sequence, slight differences in the position and orientation of such weak interactions result in minor differences in the structure of individual protein molecules thus transforming the unique structure of protein molecule into a structure ensemble. Individual members of a structure ensemble are referred to as conformational substates.

Evidence for conformational substates in proteins comes from non-exponential rebinding kinetics of carbon-monoxide (CO) to myoglobin (Austin et al. 1975) and nitrous oxide (NO) to azurin (Ehrenstein & Nienhaus 1992), temperature dependence of B-factor in X-ray crystallography of myoglobin and ribonuclease (Frauenfelder et al. 1979; Tilton et al. 1992), non-exponential spin echo decays and non-homogenous broadening of EPR line shapes in spin labeled Na^+/K^+ -ATPase (Guzzi et al. 2014) and much recently from picosecond X-ray solution scattering in sperm whale myoglobin (Oang et al. 2014).

Conformational sampling

A protein molecule is constantly shifting among its various conformational substates in the general neighborhood of the native structure via thermally driven motions. Such motions, referred to as 'conformational motions' span time scales of femtoseconds (bond vibrations) to picoseconds (small group fluctuations) to nano- and microseconds or longer (collective motion of groups of bonded or non-bonded atoms) and corresponding distance scales of fractions of an Angstrom to nanometers (McCammon 1984). Conformational motions allow enzymes to bind substrate molecules, catalyze reactions by breaking old and forming new bonds, and release product molecules at the end of the catalytic cycle. A rigid molecule would not be able to do any of these functions in a catalytically competent manner and therefore, conformational motion is essential for protein function (Daniel et al. 2003). It has been shown in prolyl cis-trans isomerase cyclophilin A (CypA) that the characteristic enzyme motions necessary for catalysis are already present in the free enzymes with frequencies corresponding to catalytic turnover rates and that protein motion important for catalysis is an intrinsic property of the enzyme (Eisenmesser et al. 2005).

Since conformational motions are thermally driven the picture of a protein molecule that emerges from an experiment depends on the temperature and time scale of measurement. At low

temperatures, much of conformational motion is frozen and individual protein molecules remain trapped in different conformational substates giving rise to a distribution in reaction rates. At intermediate temperatures, only conformational fluctuations that occur on the timescale of the reaction are visible. In the high temperature regime, individual protein molecules undergo conformational relaxation on time scales much shorter than that of the reaction studied and therefore only a single, average rate of reaction is observed.

Modeling conformational substates

In terms of free energy, conformational substates sit at points of local minima in the rugged energy landscape of proteins. The energy landscape itself is organized in a hierarchy. Top tiers consist of functionally relevant states of a protein and are separated by moderate differences in free energy. The lower tiers are much less separated in free energies and make themselves recognized only at low temperatures (Frauenfelder et al. 2009). The top tier substates can be characterized experimentally and a taxonomic approach for classifying them is feasible. However, as we go down in the hierarchy of states, the number of possible substates explodes exponentially making a taxonomic approach absolutely unemployable (Frauenfelder et al. 1991).

A solution may be obtained by treating the energy barrier of a physicochemical process A → B as not being sharp but defined by a spectral function $g(H_{AB})$, such that $d\{g(H_{AB})\}$ or $g(H_{AB})dH_{AB}$ represents the probability of having the energy barrier between H_{AB} and $H_{AB} + dH_{AB}$ and $\int_0^\infty g(H_{AB})dH_{AB} = 1$.

The number of molecules going from A to B at any given time can then be given by,

$$N_t = N_0 \int_0^\infty g(H_{AB})dH_{AB} \,.\, e^{-k_{AB}t} \qquad [12]$$

where, k_{AB} denotes the rate of reaction and bears an Arrhenius dependence on H_{AB}.

Nature of g(H)

g(H) is temperature independent (Austin et al. 1975; Frauenfelder et al. 1988) and can be obtained by taking a Laplace transform of equation [12] if N_t can be measured over a wide temperature and time range. However, a more efficient way to obtain the distribution is to assume an analytical form of $g(H)$ and then solve equation [12] numerically. In the literature, mainly two forms of $g(H)$, namely the Gamma function (Ansari et al. 1987; Young & Bowne 1984; Austin et al. 1975) and normal distribution (Ehrenstein & Nienhaus 1992; Nienhaus & Nienhaus 2011) have been used to

fit experimental data corresponding to processes exhibiting non-exponential decay kinetics arising from conformational substates in proteins.

For quantification of barrier distributions corresponding to the experimental cases presented in this chapter, the activation energy barriers were assumed to follow a Gaussian distribution such that,

$$g(H) = \frac{1}{\sqrt{2\pi\sigma^2}} exp[-(H - H_P)^2/2\sigma^2] \quad [13]$$

Where, H_P and σ are the peak enthalpy and standard variance of the distribution respectively. A good agreement of the least-squares fit to experimental data using a Gaussian/normal distribution to represent *g(H)* suggests that the model chosen represents the enthalpy barrier distribution observed in the experimental data sufficiently.

For the purpose of fitting, the pre-exponential factor '*A*' was fixed at 10^9 s^{-1}. One can derive *A* as one of the fit parameters performing TDS experiments at different ramping rates ('*m*'). However, this is not feasible in practice. The model used here may be a simplification of the energetics of the processes studied but still manages to capture the main features activation barrier involved and allows us to make faithful and meaningful comparison between test cases.

MATERIALS AND METHODS

Expression and purification of CYP119

Cytochrome P450 CYP119 was cloned from the genomic DNA library of *Sulfolobus solfataricus P1* and expressed and purified from *E. coli* as previously described (McLean et al. 1998; Maves & Sligar 2001).

Expression and purification of CYP101

CYP101 was expressed and purified as previously described in Chapter 2.

Preparing ferrous-CO complexes of CYP101 for studying CO-rebinding upon flash photolysis via TDS

Approximately 25 nmoles of CYP101 (from a stock solution of > 500 µM) was diluted in 650 µl of 80% ultra-pure glycerol (Sigma-Aldrich) in a clear Fisherbrand 10-425 glass-vial with a screw thread top. The protein was deoxygenated by passing a gentle stream of compressed Argon over it under rotation for 2 minutes. The protein solution was then taken inside an anaerobic chamber

where it was reduced with ~5 mM sodium dithionite solution, prepared fresh in anaerobic buffer. Reduction was confirmed spectrophotometrically with the help of an Oriel spectrophotometer. Additional dithionite was added so as to maintain a similar height of the absorption peak for sodium dithionite and reduced P450 (314 nm for sodium dithionite and 408 nm for reduced P450). This approximately translates to a fifteen-fold molar excess of dithionite in solution. The reduced protein solution was then transferred to a methacrylate cuvette and the volume of solution was adjusted to 800 µl with anaerobic buffer. The cuvette was sealed with parafilm, placed in a secondary container (glass cylinder with ends sealed with rubber septa) and brought out of the anaerobic chamber where pure, compressed carbon monoxide was bubbled through it at room temperature for 45 seconds at a rate of 1-2 bubbles per second. The samples were then gradually cooled down to 77K in the cryostat setup to avoid formation of cracks that might affect optical quality of the sample.

Preparing ferric samples of CYP119 for studying spin-state equilibrium kinetics

Recombinant CYP119 from *Sulfolobus solfataricus P1* was expressed and purified *E.coli* as described in (McLean et al. 1998; Maves & Sligar 2001). In order to obtain CYP119 in its low-spin ferrous state 31.25 µM of CYP119 in 100 mM KPi pH 7.4 containing 65% glycerol was taken in a methacrylate cuvette and cryoreduced with an approximately, 3.5 MRad dose of reducing X-rays from a ^{60}Co source.

Eliminating free electron absorption via photobleaching

Only a small fraction of mobile electrons generated upon gamma radiolysis of aqueous glycerol solution is utilized for heme-iron reduction. The large excess of unused electrons result in a deep violet color of the solution which hinders optical characterization of the sample. The problem is overcome by photobleaching the samples in a shallow, wide-mouthed liquid nitrogen dewar placed in the path of a focused light beam from a 100W/ 12V tungsten lamp fitted with a 450 nm filter for 4 hours.

Data acquisition

Changes in the optical spectra corresponding to each of the three temperature sensitive processes studied here were recorded in the same setup described in Chapter 2 under “Thermal annealing instrumentation”. However, this time the thermocouple was not in direct contact with the protein solution but was rather fixed to the sample holder at its base, making physical contact with the

sample cuvette when present. Spectra were recorded between 350 and 600 nm at a scan rate of 300 nm/min and a time interval of 1 min between 100 K and 200 K.

Modeling the conformational heterogeneity in proteins

The temperature range of 100-200 K falls below and around the glass transition temperature (~170 K) of aqueous-glycerol solutions used here (Gonzalez et al. 2011). In this temperature range all large-scale protein motion is frozen and therefore, conformational heterogeneity of the sample becomes consequential.

$$\frac{dN}{dT} = -kN \quad [14]$$

where, $k = A\left(\frac{T}{T_0}\right) exp\left(\frac{-H}{RT}\right)$ [15]

For a linear temperature ramp

$$T = T_i + mt \quad [16]$$

where, m is the linear temperature ramp rate

N at any given temperature can be given by the integral form of (2.1) as,

$$N = N_i exp\left[-\int_0^t k dt'\right]$$

Substituting *'t'* for *'T'* using [16] we get,

$$N = N_i exp\left[-\int_{T_i}^{T} \frac{k}{m} dT'\right]$$

Differentiating w.r.t *'T'* to get an expression for the rate of change of *'N'* with temperature

$$\frac{dN}{dT} = N_i exp\left[-\int_{T_i}^{T} \frac{k}{m} dT'\right] . \frac{d}{dT}\left(-\int_{T_i}^{T} \frac{k}{m} dT'\right)$$

$$\frac{dN}{dT} = N_i exp\left[-\int_{T_i}^{T} \frac{k}{m} dT'\right] . \left(\frac{-k}{m}\right)$$

$$\frac{dN}{dT} = -N_i \frac{k}{m} exp\left[-\int_{T_i}^{T} \frac{k}{m} dT'\right]$$

$$\frac{dN}{dT} = -N_i \frac{k}{m} \exp(-\theta) \quad [17]$$

where, $\theta = \frac{AT_0}{m}\left[\left(\frac{T}{T_0}\right)^2 E_3\left(\frac{H}{RT}\right) - \left(\frac{T_i}{T_0}\right)^2 E_3\left(\frac{H}{RT_i}\right)\right]$

$E_3(x)$ is the exponential integral which can be calculated as,

$$E_3(x) = \int_1^\infty \frac{e^{-xt}}{t^3} dt$$

For a distributed energy barrier [17] transforms into

$$\frac{dN}{dT} = -N_i \frac{k}{m} \int_0^\infty k exp(-\theta)\, g(H) dH \quad [18]$$

where,

$$g(H) = \frac{1}{\sqrt{2\pi\sigma^2}} exp\left[-\frac{(H - H_P)^2}{2\sigma^2}\right]$$

and, k is given by [15].

The schematic in Figure 10 depicts organization of the energy landscape of proteins and the origins of distributed barriers. If A and B are two normally distributed energy minima with characteristic parameters of (H_A, σ_A) and (H_B, σ_B) on the energy landscape of a protein, separated by ΔH (= H_A – H_B), heretofore referred to as H, in terms of their mean enthalpies, any transition between A and B could also be represented as a normal distribution with mean enthalpy of H.

As shown in the previous chapter, a linear temperature-time dependence results in a sigmoidal shape of the 'N' versus 'T' curve for a process characterized by a single activation energy barrier. A distributed energy barrier affects the curve by causing broadening of the transition along the temperature axis. Figure 11 presents a simulated 'N' versus 'T' curve for such a process with characteristic parameters, H_P and σ of 9.5 and 0.5 kcal/mol respectively. Here, H_P determines the temperature for half-transition, $T_{1/2}$ and σ effects the overall spread of the transition on the temperature domain. Figure 11 depicts this point aptly. Figure 12A contains three energy distributions having the same peak enthalpy, H_P of 9.5 kcal/mol but varying standard variances, σ of 0.5, 1.0 and 2.0 kcal/mol. Figure 12B shows the simulated concentration profiles for these three distributions. All three curves exhibit a $T_{1/2}$ of 175 K but different breadth of transition with curves corresponding to broader energy distributions showing a shallower transition.

Another variable that effects the shape and position of concentration profiles on the temperature axis is temperature ramp rate, or 'm'. Figure 13 shows simulated plots for the rate of decrease of

concentration of starting species, 'N' as a function of temperature and the concentration profile that would one would obtain studying such a transition via TDS. The plot contains three different temperature ramping rates and peak enthalpies in five different combinations. The standard variance in peak enthalpy was kept constant at 0.1 kcal/mol. Like H_P, 'm' affects $T_{1/2}$. The blue lines represent simulated curves for transitions having identical activation barriers but variable temperature ramp rates. Higher values of 'm' correspond to higher values of $T_{1/2}$. The same trend is seen upon keeping 'm' constant and varying 'H_p' (curves #2, 3 and 5). Thus, 'm' and 'H_P' decide the position of the concentration profile whereas 'σ' governs its shape.

Fitting routine

For the data described below curve fitting was performed using the unconstrained nonlinear minimization routine 'fminsearch' in MATLAB 2012b. An objective function was setup to calculate the root mean square difference between simulated and experimental 'N' versus 'T' curves at temperatures where experimental data was available. Input parameters to the fitting routine were scaled to fall between 0 and 1. Different initial guesses were tested to make sure there was no bias in the fit parameters obtained on the values of initial guess input.

RESULTS AND DISCUSSION

Non-equilibrium relaxation of spin state

The heme-iron of cytochromes P450 in its resting state exists in equilibrium between penta-coordinated, high-spin and hexa-coordinated, low-spin states. Substrate-free P450s are predominantly low-spin due to a water molecule coordinated as the sixth ligand trans to the distal cysteine. Substrate binding destabilizes water ligation and converts the heme iron into a penta-coordinated, high-spin ferric state. This is accompanied by a positive shift in redox potential that allows the substrate-bound enzyme to be reduced by NADPH from its redox partner, cytochrome P450 reductase. The spin-state transition is essentially the 'on' switch for P450 chemistry keeping the enzyme from consuming redox equivalents in futile cycles and preventing the formation of superoxide and peroxide via the autoxidation and peroxide shunts respectively.

The high-spin, low-spin equilibrium can be studied by exploiting the fact that water, although a weak ligand, favors the ferric state over ferrous state. Reducing a low-spin ferric P450 results in a low-spin ferrous enzyme which then relaxes to a high-spin state, a transition that can be monitored

spectrophotometrically owing to different optical absorption spectra of each of these species. (Figure 14 Top panel)

To study the relaxation of a low-spin to high spin, a low-spin ferric enzyme preparation of CYP119 was cryoradiolytically reduced in a 65% glycerol solvent to convert it into its low-spin ferrous state. The low-spin ferrous heme has a characteristic absorption spectra with maxima at 441 nm and 561 nm (Denisov et al. 2001). As the temperature is gradually increased from 100 K to 200 K, conformational motion becomes less restricted which allows for the relaxation of low-spin ferrous heme to its high-spin state. Spectrally, this is observed as the appearance of an absorption maximum at 410 nm. After 191 K, carbon monoxide (CO) produced as a result of radiolysis of glycerol, finds its way into the active site where it reacts with the ferrous heme to form the ferrous-CO complex evidenced by the appearance of the 450 nm band. Figure 14 provides a schematic of the process and corresponding changes in the optical absorption spectral landscape.

In order to trace the conversion of low-spin ferrous to high-spin ferrous from the complex data set as in Figure 14, optical spectra gathered between 110 K and 195 K (Spectra #5-63) were subjected to a singular value decomposition (svd) analysis. The second eigen concentration vector from the svd of spectral range of 400-500 nm and 550-570 nm was plotted against temperature (Figure 15A). The values of concentration obtained were normalized between 0 and 1 before they were fit to a distributed energy barrier model as previously described.

Best fit was obtained with a combination of a single activation energy barrier of 9.89 kcal/mol (obtained as a distributed barrier of $H_{P,1}$ = 9.89 kcal/mol and σ_1 = 0.005 kcal/mol) and a distributed barrier of $H_{P,2}$ = 8.28 kcal/mol and σ_2 = 0.684 kcal/mol. The relative contributions of $H_{P,1}$ and $H_{P,2}$ were 0.6 and 0.4. (Figure 15B) This may correspond to states of the enzyme with water or glycerol present in the active site.

Di-atomic ligand binding

Wild-type CYP101

The next important step after reduction of ferric-heme in P450 catalysis is the binding of molecular oxygen. Ferrous heme in P450s, like in other heme proteins such as myoglobin and hemoglobin, has the ability to bind a molecule of oxygen to form a superoxo species termed as the oxy-ferrous complex. This stage onwards the enzyme can either proceed to catalytic arm of the P450 reaction wheel or dissociate the bound oxygen as a superoxide anion and return to the ferric resting state. The latter process, referred to as the autoxidation shunt, constitutes the first uncoupling pathway in

P450s. The quasi-stable nature of oxy-ferrous intermediate makes it difficult to study. However, to study the binding event use of diatomic ligands such as CN^-, NO and CO has proven to be more beneficial.

In the current study, we have used CO as an O_2 mimic. The Fe-CO complex has a characteristic absorption peak at 448 nm (*binding of CO –split Soret*). Moreover, the Fe-CO bond is photo-labile. Monitoring rebinding of CO upon photolysis of a ferrous-CO complex provides a good means to study diatomic ligand binding.

We prepared the ferrous-CO complexes of substrate free CYP119 and camphor-bound CYP101, WT and T252A mutant by bubbling pure, compressed CO through a preparation of reduced enzyme in an aqueous-glycerol solvent. The resulting Fe-CO complexes were then photolyzed by subjecting them to a focused beam of light from a tungsten lamp for 4 hours at 77 K. CO-rebinding was studied via temperature derivative spectroscopy, monitoring the increase in absorbance at 448 nm as the temperature increased linearly from 100 K to 200 K.

Photolysis of ferrous-CO complex of wild-type CYP101, in H_2O gave approximately 60% yield of photolysis. To obtain the energetics of rebinding of the flashed CO-molecule to the heme iron the second eigen concentration vector from the singular value decomposition (svd) analysis of the entire spectral was normalized and fitted to the distributed energy barrier model, as described earlier. Using a pre-exponential factor of 10^9 and a ramping rate of 1.2 deg/min, which is the average ramping rate of the transition, the best fit to the experimental data corresponded to a peak enthalpy of 7.42 kcal/mol and a standard variance in peak enthalpy of 0.93 kcal/mol (Figure 17The same experiment was done in deuterated solvent. This yielded a peak enthalpy and standard variance of enthalpy of 7.28 and 0.95 kcal/mol respectively (Figure 18). Since the geminate rebinding of CO is not expected to be isotope sensitive we expect similar energy distribution profiles. Observations from TDS annealing experiments done in protiated and deuterated solvents confirm the fact.

T252A mutant of CYP101

In addition to wild-type CYP101 CO-rebinding behavior of the T252A mutant of CYP101 was also investigated. The plot of fraction of P450 that was still without CO upon annealing versus temperature in protiated aqueous-glycerol solvent showed multiple barriers as opposed to a single distributed barrier seen in wild-type CYP101. Similar behavior was observed in deuterated solvent (Figure 19). A small non-overlapping region on the concentration profiles observed between H_2O and D_2O is an artifact of normalization. The threonine to alanine mutation in CYP101 creates an

extra cavity in the active site of CYP101 where the CO molecule may migrate upon flash photolysis. Figure 20 elucidates the point.

Wild-type CYP119

CO-flash photolysis of CYP119 gave a 15% yield of photolysis. Fitting the geminate rebinding of CO as a function of temperature to a distributed energy barrier model gave a peak enthalpy of 6.52 kcal/mol and a standard variance of distribution of 0.535 kcal/mol (Figure 21).

Peroxo-annealing

Another process that can be studied using temperature derivative spectroscopy and where it really shows its utility in answering important mechanistic questions is peroxo annealing. In this study, we used TDS to study the fate of cryoreduced oxy-complexes of cytochrome P450s in protiated and deuterated aqueous-glycerol solvents. This comparison allows for calculating kinetic solvent isotope effects (KSIE) in the decay of the peroxo-complex which in turn provides a basis to distinguish between mechanisms that differ in the involvement of protons such as in CYP19A1 and CYP17A1. TDS distinguishes itself from other techniques of measuring KSIEs by being more sensitive and providing a complete temperature profile of KSIE. Rates of chemical reaction are temperature dependent and so are their ratios. This is well understood but not applied much since measuring rates at different temperatures and in different solvent conditions is time, labor and material intensive. However, in order to draw a faithful comparison based on KSIEs we need a complete temperature profile of rates in different solvent systems.

In this part of chapter 3, I describe the results obtained from applying temperature derivative spectroscopy to monitor the decay of reduced oxy-ferrous complexes of D251N mutant of CYP101 and human CYP19A1.One electron reduction of the oxy-ferrous complex in P450s produces the 'peroxo-anion', which upon protonation at the distal oxygen atom of the bound dioxygen molecule yields the 'hydroperoxo-anion'. The peroxo-anion, and sometimes the hydroperoxo anion as well, is referred to as 'Compound 0' in P450 literature. A second protonation at the distal oxygen facilitates O-O scission giving rise to the reactive oxo-ferryl π-cation radical known as 'Compound 1'. The protons needed to ensure the productive progression of the peroxo anion to Compound 1 are supplied by a hydrogen bonding network comprised of an acid-alcohol pair, Asp-251 and Thr-252 in CYP101 and Asp-309 and Thr-310 in CYP19A1, and water molecules present at the active site.

The role of the acid-alcohol pair was first discovered by mutagenesis studies in CYP101. A mutation of Asp to Asn in CYP101 has been shown to hinder the first protonation leading to an accumulation

of the peroxo-anion as opposed to the hydroperoxo anion as seen in wild-type CYP101 and most other P450s. It is also known, via EPR annealing experiments that the peroxo anion in D251N CYP101 transforms to the hydroperoxo anion and then the product complex (Davydov et al. 2001). Furthermore, under steady-state turnover conditions, D251N shows an enhanced kinetic solvent isotope effect as compared to the wild-type enzyme (Vidakovic et al. 1998). Prior knowledge of the fate of peroxo anion upon thermal annealing and the steady state kinetic behavior of CYP101/ D251N in protiated and deuterated solvents makes it the perfect model candidate for testing the idea of measuring KSIE during peroxo annealing via TDS. Success in doing so would give us a means to distinguish between the 'Cpd 0' and 'Cpd 1' mechanisms of aromatization by CYP19A1 (Page 6). Should Cpd1 be used as the reactive intermediate for C-C scission, Cpd 0 or peroxo-anion would have to be protonated twice at the distal oxygen to facilitate O-O heterolysis that results in the formation of Cpd1. This would manifest as a difference in rates of decomposition of reduced oxy-ferrous complex of CYP19A1 in protiated and deuterated solvents. On the other hand, the use of Cpd0 as the reactive intermediate by CYP19A1 would not necessitate such protonation and would therefore, show no H/D sensitivity under similar circumstances.

D251N mutant of CYP101

The magnitude of optical absorption signal corresponding to peroxo-annealing of CYP101 D251N was less than that compared to the other two examples of application of TDS presented in this chapter. A slightly different approach than used previously was used to extract the concentration profile of reduced oxy-ferrous complex of CYP101 D251N and CYP19A1 for this section. Difference spectra from the TDS experiment was subjected to svd analysis and reconstructed using the first four eigen vectors. Difference in the absorption values at 446 nm and 419 nm corresponds to conversion of peroxo-P450 to its low-spin form and was plotted against temperature. The concentration values were normalized between 0 and 1 and fit to a distributed energy barrier model using the same fitting routine described on page 41.

Fitting was performed using the single distribution model and best fit was obtained with a single distributed energy barrier with H_P = 8.66 kcal/mol and σ = 0.515 kcal/mol and H_P = 9.31 kcal/mol and σ = 0.39 kcal/mol in protiated and deuterated solvents respectively. The 0.65 kcal/mol increment in the peak enthalpies in D_2O is seen by a positive shift in the half transition temperature by ~10 K. Figure 25A is a plot of the rate constants corresponding to these two activation energies and shows a clear temperature dependence of the KSIE on temperature (Figure 25B). Based on this analysis, the KSIE on peroxo annealing for D251N mutant of CYP101 at 298 K is 3.98.

CYP19A1

A treatment similar to that described above was applied to monitor the decay reduced 19-oxo-AD bound oxyCYP19A1 upon thermal annealing via TDS. Poor signal-to-noise interfered with the ability to obtain perfect fits to the experimental data using the fitting routine described earlier. Best fit was obtained with H_P = 9.9 kcal/mol and σ = 0.005 kcal/mol and H_P = 10.26 kcal/mol and σ = 0.003 kcal/mol in protiated and deuterated solvents respectively. Despite poor fitting a positive shift in the temperature of half transition in D_2O clearly indicates the presence of a kinetic solvent isotope effect of greater than 1 for this process (Figure 26). This in turn supports the use of 'Compound 1' for aromatization by CYP19A1.

CONCLUSION

It is now well known that proteins are not biomolecules with a fixed three-dimensional structure but an ensemble of structures all vibrating around a central structure, sampling innumerable related structures in the process. Enzymes and also substrates control the rate and route of catalysis by altering the conformational landscape of both the ground and excited states by preferentially sampling some energy minima over others. A randomly selected pair of substates in this vast conformational landscape may be separated by a small-scale motion such as a single bond rotation or vibration or by a much larger scale motion involving multiple atoms of a secondary structure element. If these two states are experimentally distinguishable one may be able to see the conformational relaxation that the enzyme undergoes while going from state A to B. This has been done by matching the magnitude order of timescale in which these transitions may occur by faster data acquisition or by artificially slowing down the process by studying it at a significantly lower temperature. If these conditions are met, one observes distributed kinetics for the A ⇒ B conversion. The distribution in rates reflects the distribution in energy of activation for the process and therefore, the ruggedness of the conformational landscape.

Temperature derivative spectroscopy is a general experimental method to measure processes with distributed kinetics in combination with different spectroscopic techniques such as fluorescence spectroscopy, FTIR and Raman spectroscopy. In cytochrome P450s, the various iron-heme intermediates have characteristic UV-Vis absorption spectra and high molar absorption coefficients making optical absorption spectroscopy a perfect technique to mirror changes occurring upon thermal annealing of a particular intermediate in a TDS experiment. By tracking the conversion of one intermediate into another TDS can provide precise quantitative data on the fate of individual

intermediates. As shown in this chapter, various processes such as spin-state conversion, di-atomic ligand binding and peroxo-annealing may be studied using this approach.

Furthermore, by performing these experiments under different solvent conditions one can calculate precisely the kinetic solvent isotope effect specially in cases where it answers important mechanistic questions as in the case of CYP19A1. The application of TDS highlights a less appreciated feature of KSIEs which is, KSIEs being ratios of rates are temperature dependent. Usually, the rates of a reaction are compared at a particular temperature to obtain KSIE and conclusions are drawn from its numerical value. As is shown in Figure 25 KSIE bears a temperature dependence. A true comparison of the behavior of a reaction in protiated and deuterated solvent systems can only be obtained from the full temperature profile of KSIE such as that provided by TDS.

The presence of narrow distributions in the case of CYP19A1 and slightly broader distributions in the case of CYP101 suggest control over conformational heterogeneity as a means to acquire specificity by an enzyme system. The presence of a KSIE in peroxo annealing in 19-oxo-AD bound CYP19A1 suggests the involvement of Cpd1 in the C-C lyase reaction of CYP19A1.

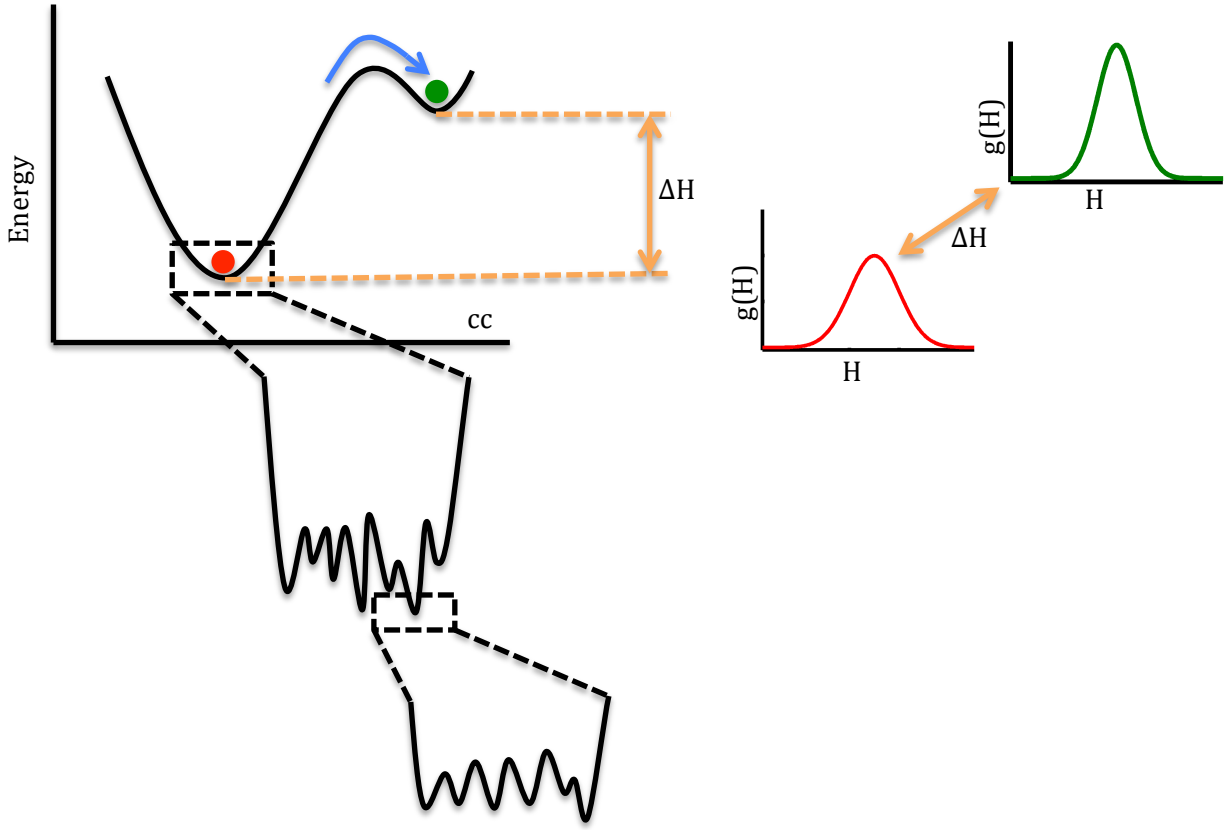

Figure 10: A schematic representation of the origins of conformational heterogeniety in proteins and distributed energy barriers.

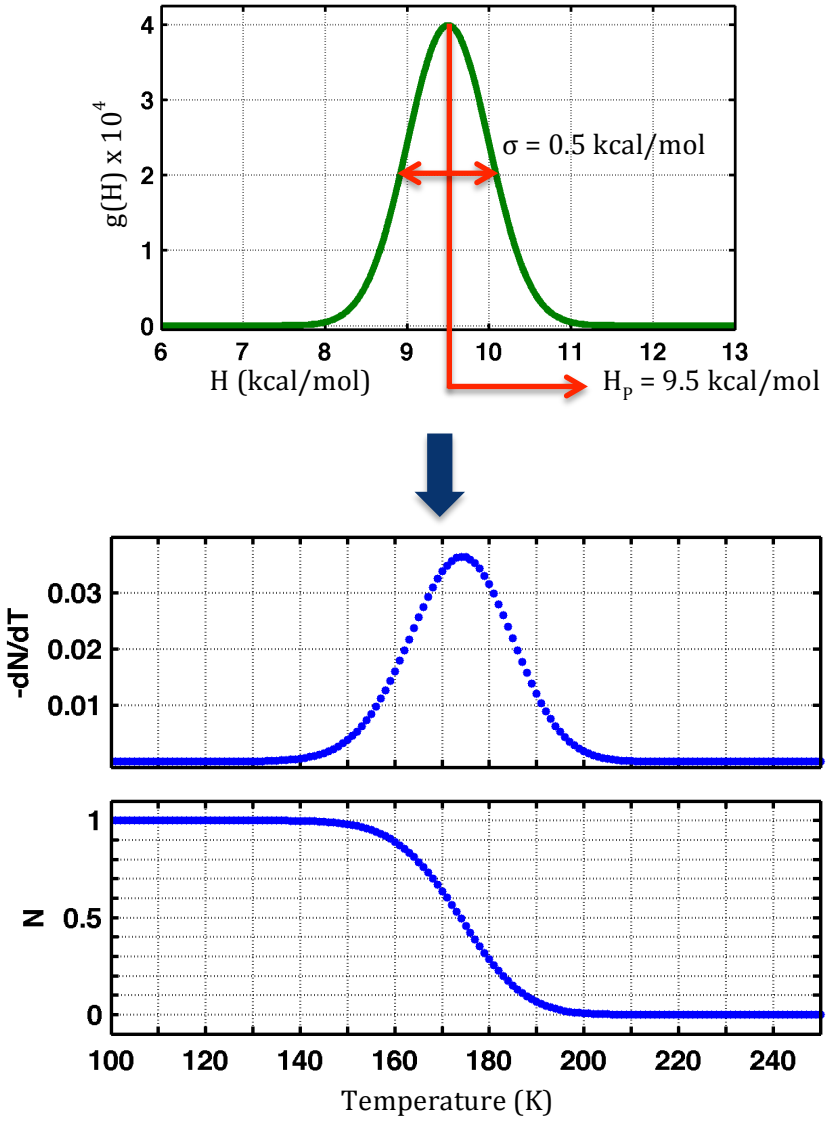

Figure 11: A model N versus T curve for a transition characterized by a distributed energy barrier of peak enthalpy, H_P = 9.5 kcal/mol and a standard variance, σ of 0.5 kcal/mol.

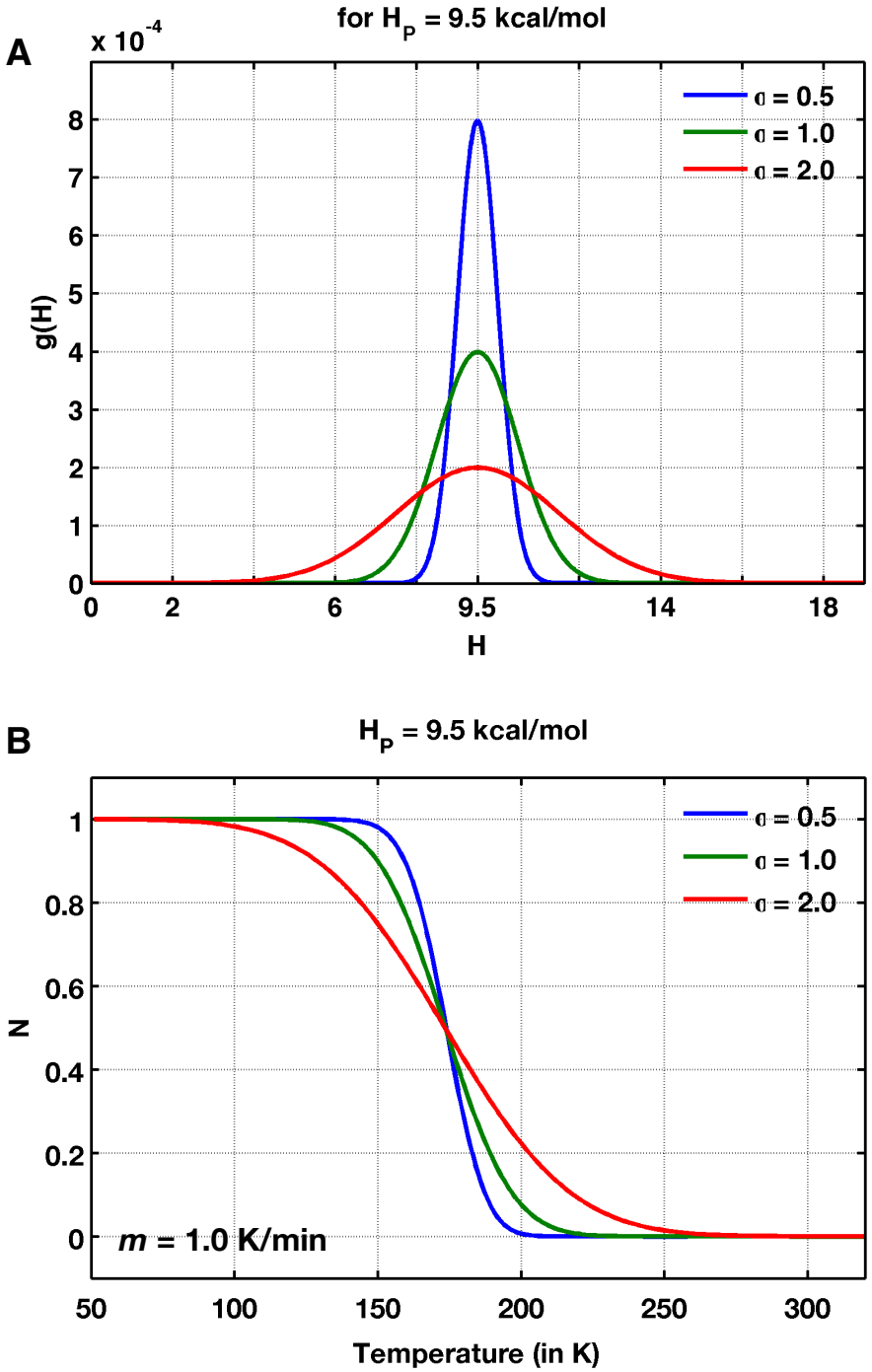

Figure 12: Simulated 'N' versus 'T' profiles for three energy distributions having a peak enthalpy, H_P of 9.5 kcal /mol and varying standard variances of 0.5, 1.0 and 2.0 kcal/mol showing the effect of the breadth of distribution on the breadth of transition observed via TDS.

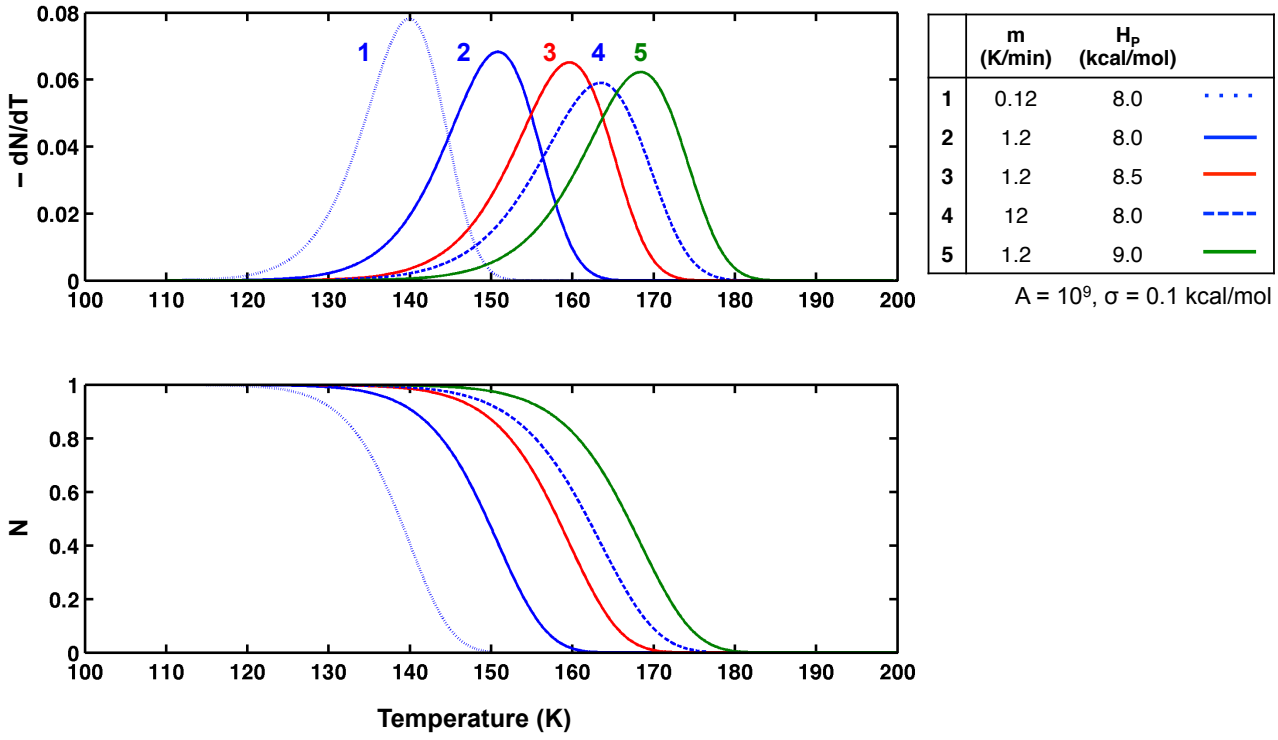

Figure 13: Simulated 'N' versus 'T' curves showing the effect of peak enthalpy, 'H_P' and 'm' on the observed concentration profiles in a TDS experiment.

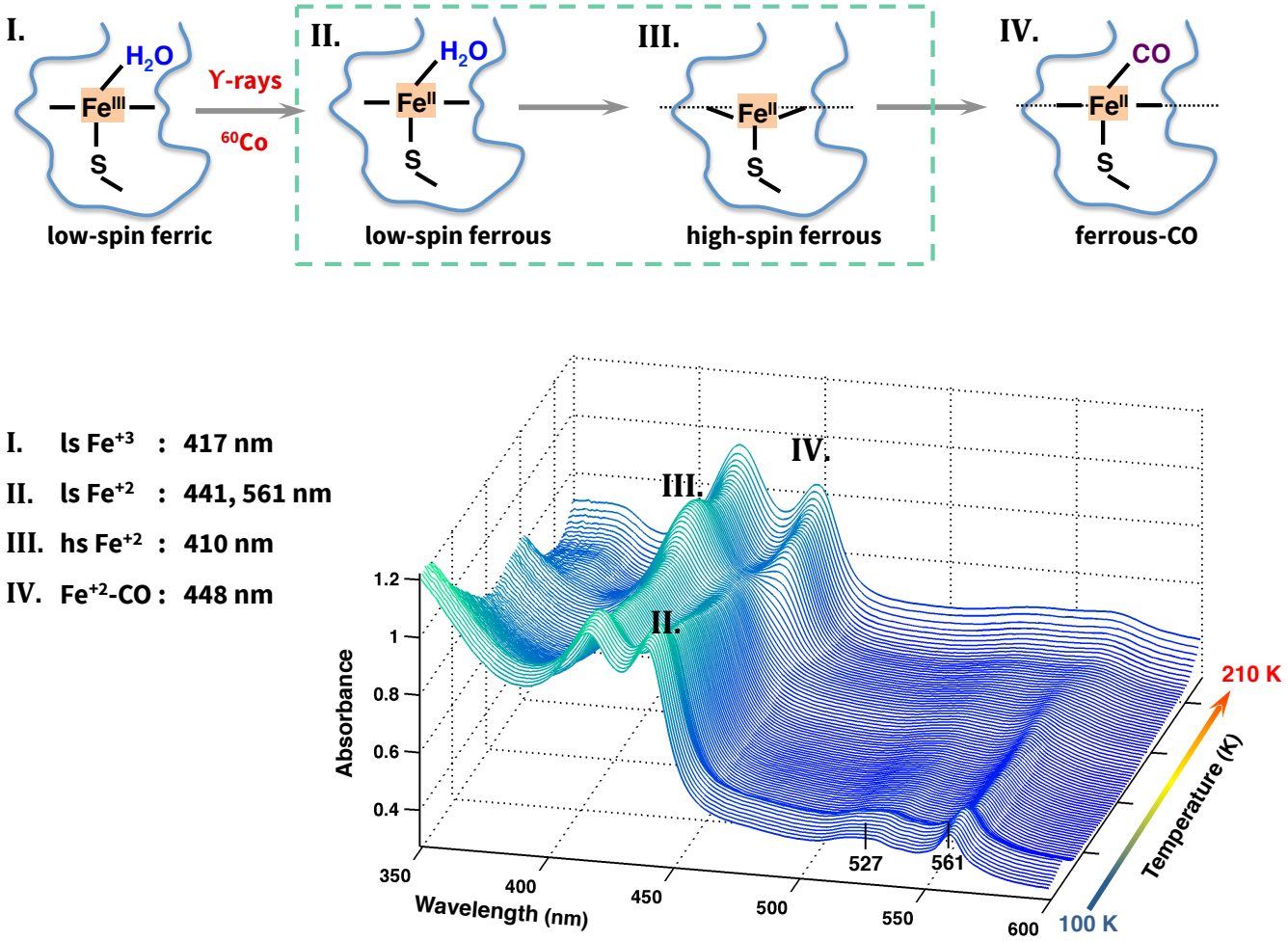

Figure 14: (Top) Schematic of the species obtained upon (Bottom) 3D plot showing spin-state equilibrium relaxation in P450s studied via optical annealing of cryoreduced low-spin CYP119.

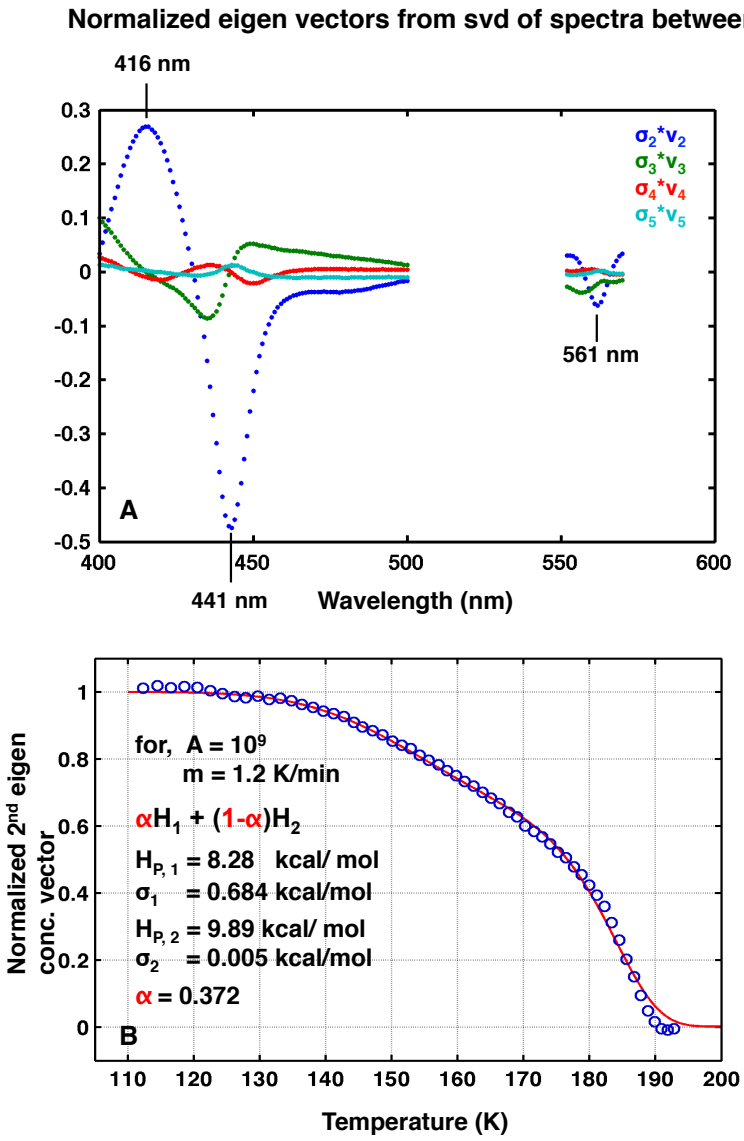

Figure 15: A) Second abstract eigen spectral vector for data between 110 and 195K. B) Normalized second eigen concentration vector for hs-ls relaxation in CYP119 (blue) and corresponding fit to a distributed energy model (red).

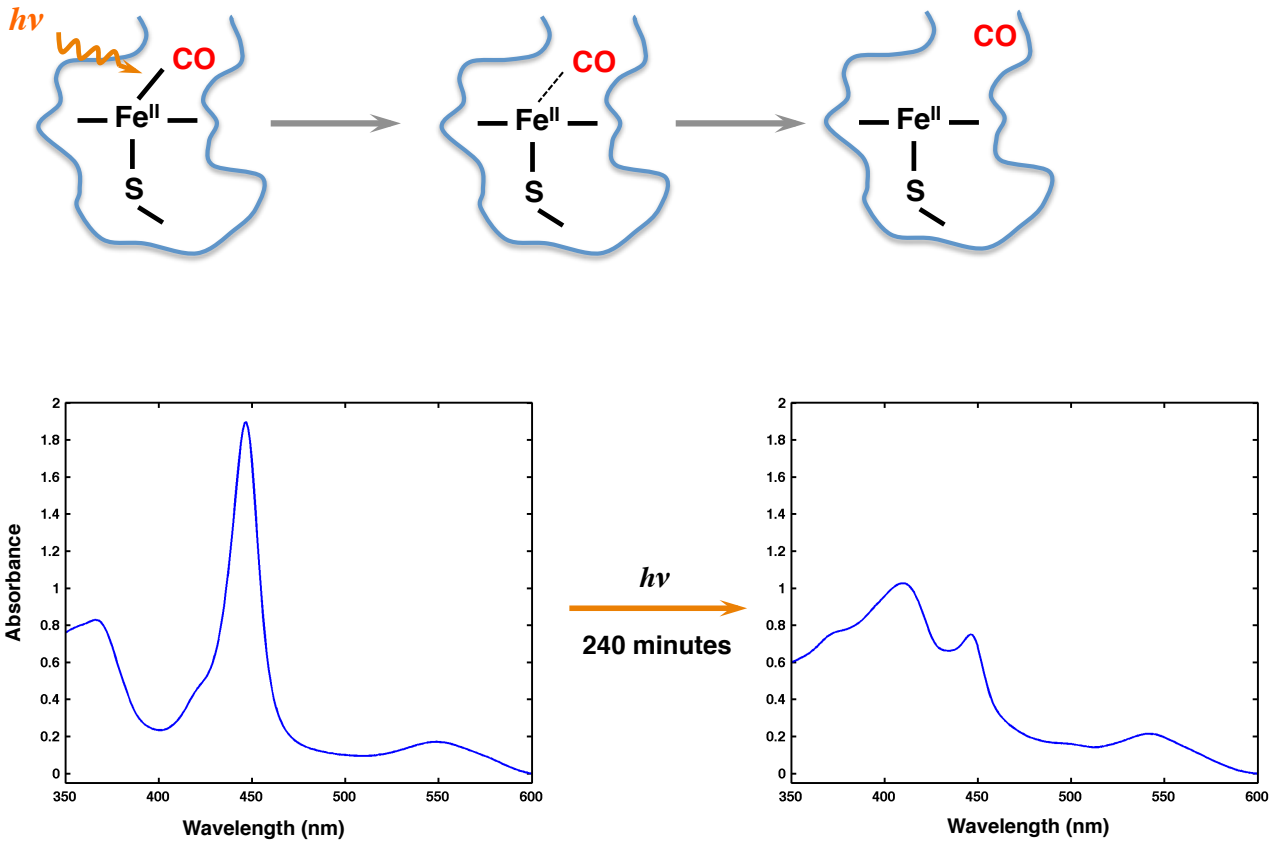

Figure 16: (Top) Schematic of the CO-flash photolysis process (Bottom) Change in the optical absorption spectrum of wild-type CYP101 after subjecting it to a high-intensity light beam from a 100 W tungsten lamp for 4 hours.

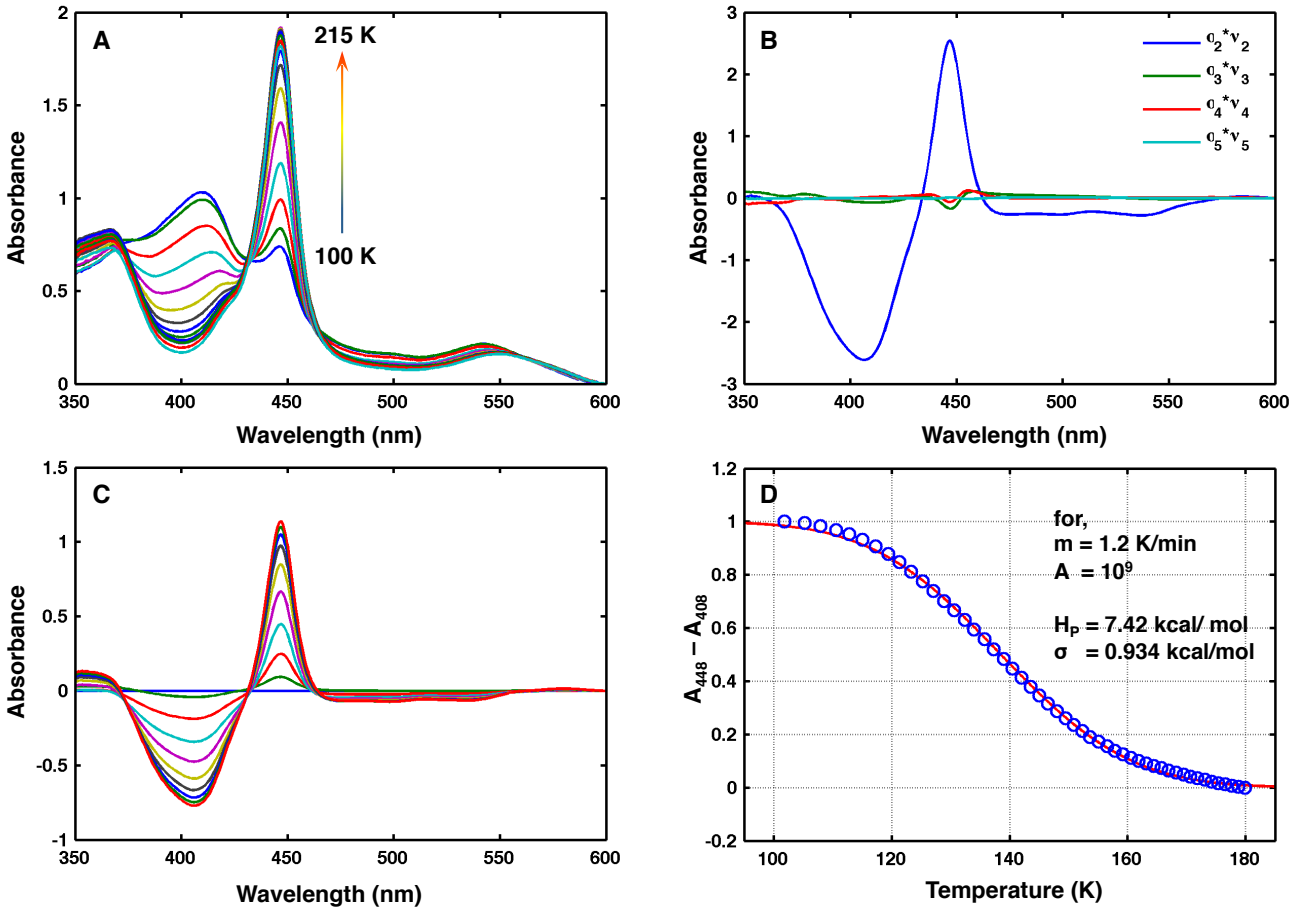

Figure 17: A) Spectral changes associate with CO-rebinding in CYP101 in H_2O as studied by Temperature Derivative Spectroscopy (TDS). B) Normalized eigen vectors from singular value decomposition of the optical absorption data set. C) svd reconstructed difference spectra. D) CO-rebinding as monitored by the difference in absorption at 448 nm and 408 nm versus temperature. The blue dots represent actual data points whereas the red line shows the fit obtained using a distributed energy barrier model.

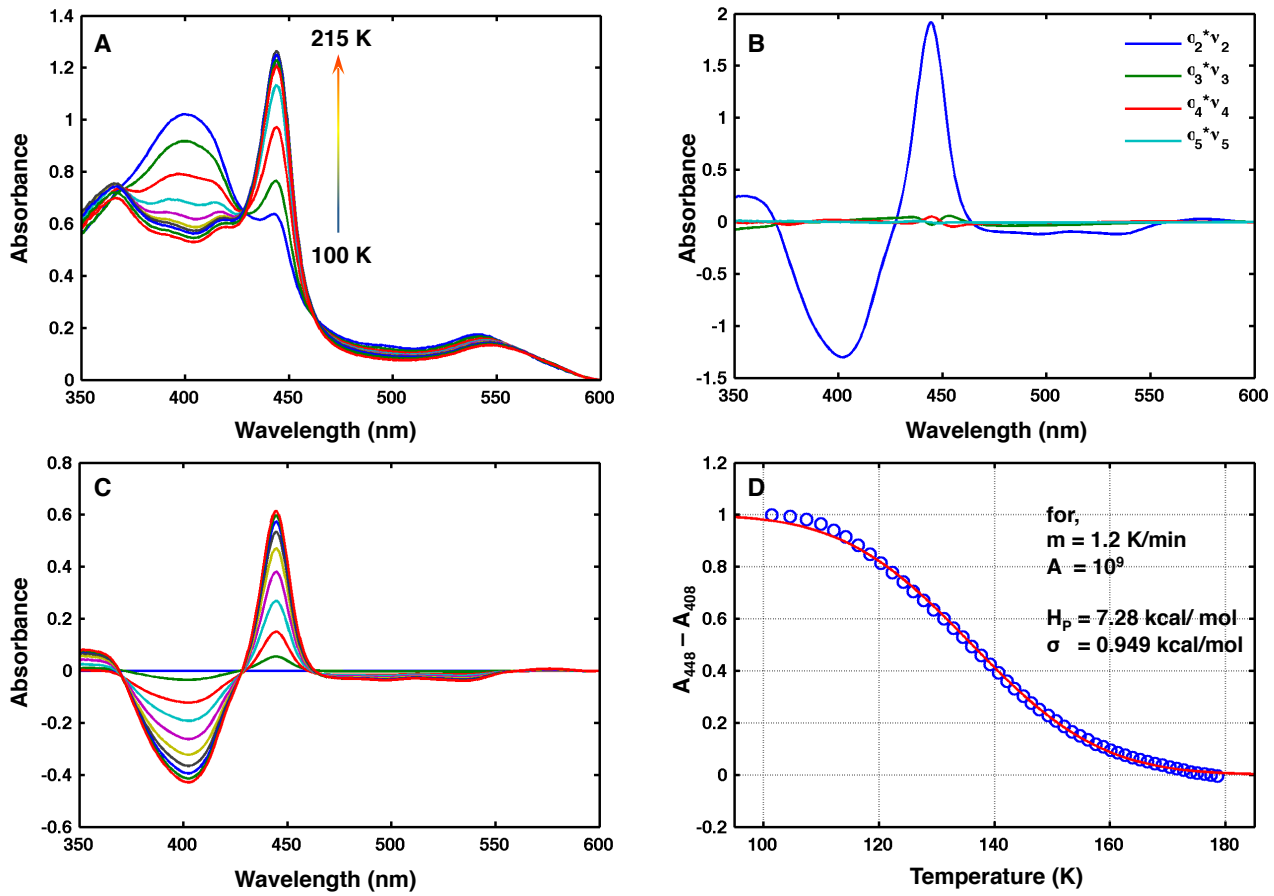

Figure 18: A) Spectral changes associate with CO-rebinding in CYP101 in D_2O as studied by Temperature Derivative Spectroscopy (TDS). B) Normalized eigen vectors from singular value decomposition of the optical absorption data set. C) svd reconstructed difference spectra. D) CO-rebinding as monitored by the difference in absorption at 448 nm and 408 nm versus temperature. The blue dots represent actual data points whereas the red line shows the fit obtained using a distributed energy barrier model.

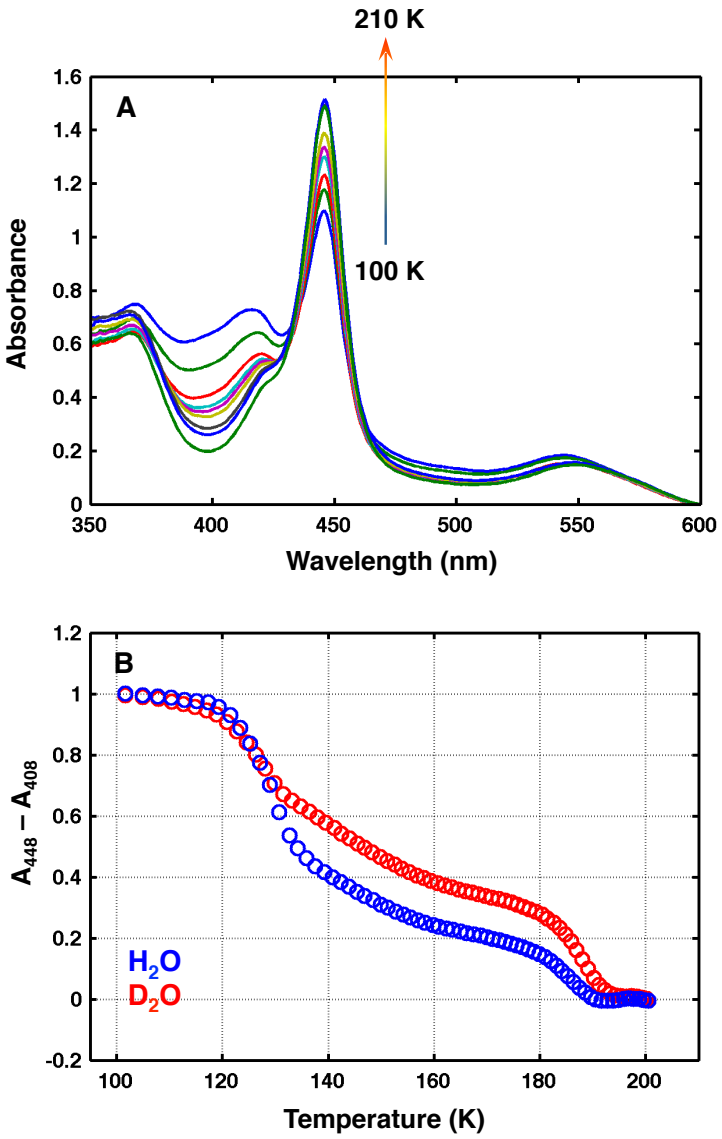

Figure 19: A) Changes in the optical absorption spectrum of CYP101 T252A mutant in protiated aqueous-glycerol solvent after CO photolysis studied via TDS. B) CO rebinding in CYP101 T252A in protiated (blue) and deuterated (red) aqueous-glycerol solvents as observed via TDS.

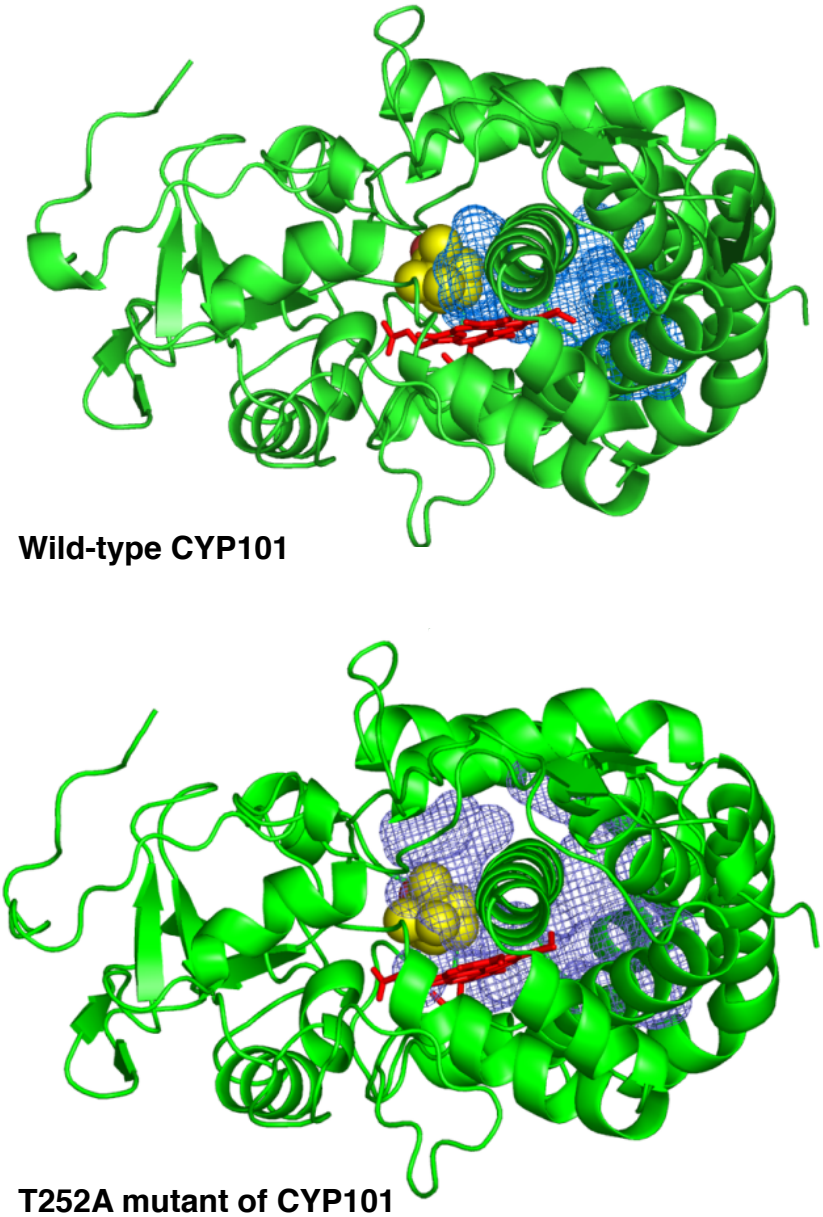

Figure 20: Comparison of the active sites of wild-type CYP101 and its T252A mutant. An extra cavity is created upon mutation of Threonine-252 to Alanine that explains the peculiar CO-rebinding behavior of CYP101 T252A as compared to the wild-type enzyme.

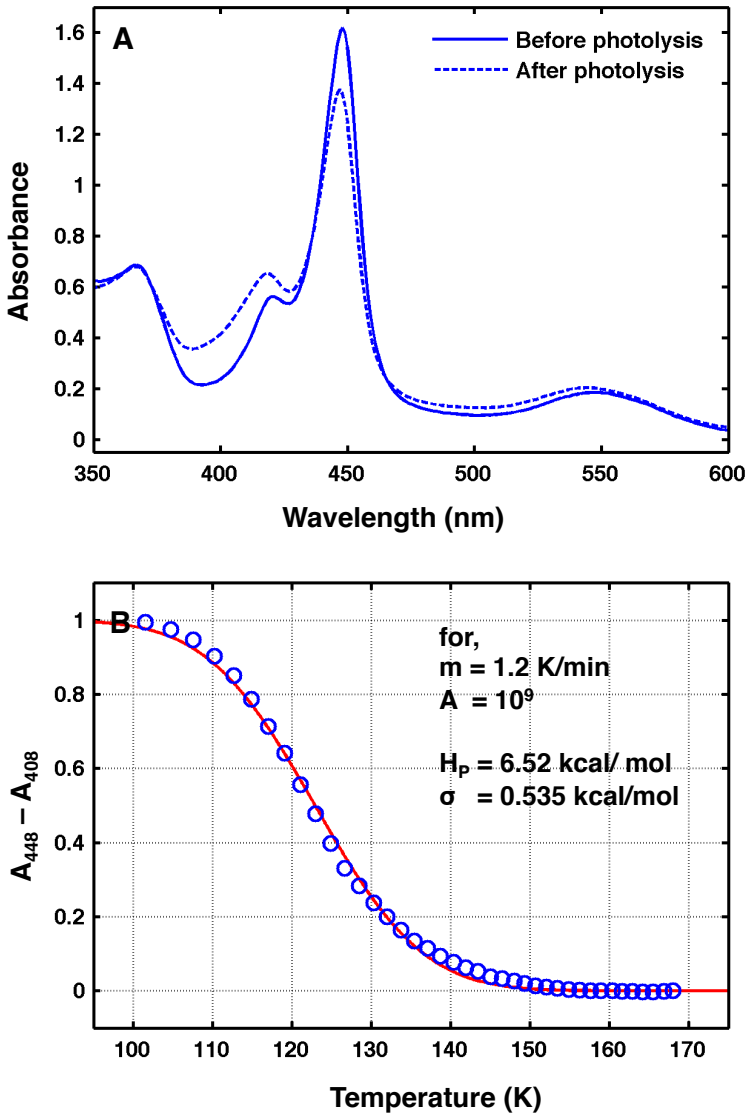

Figure 21: A) Optical absorption spectrum of wild-type CYP119 in protiated aqueous-glycerol solvent before and after photolysis. B) CO rebinding in CYP119 (blue –experimental data and red – fit based on a distributed energy barrier model).

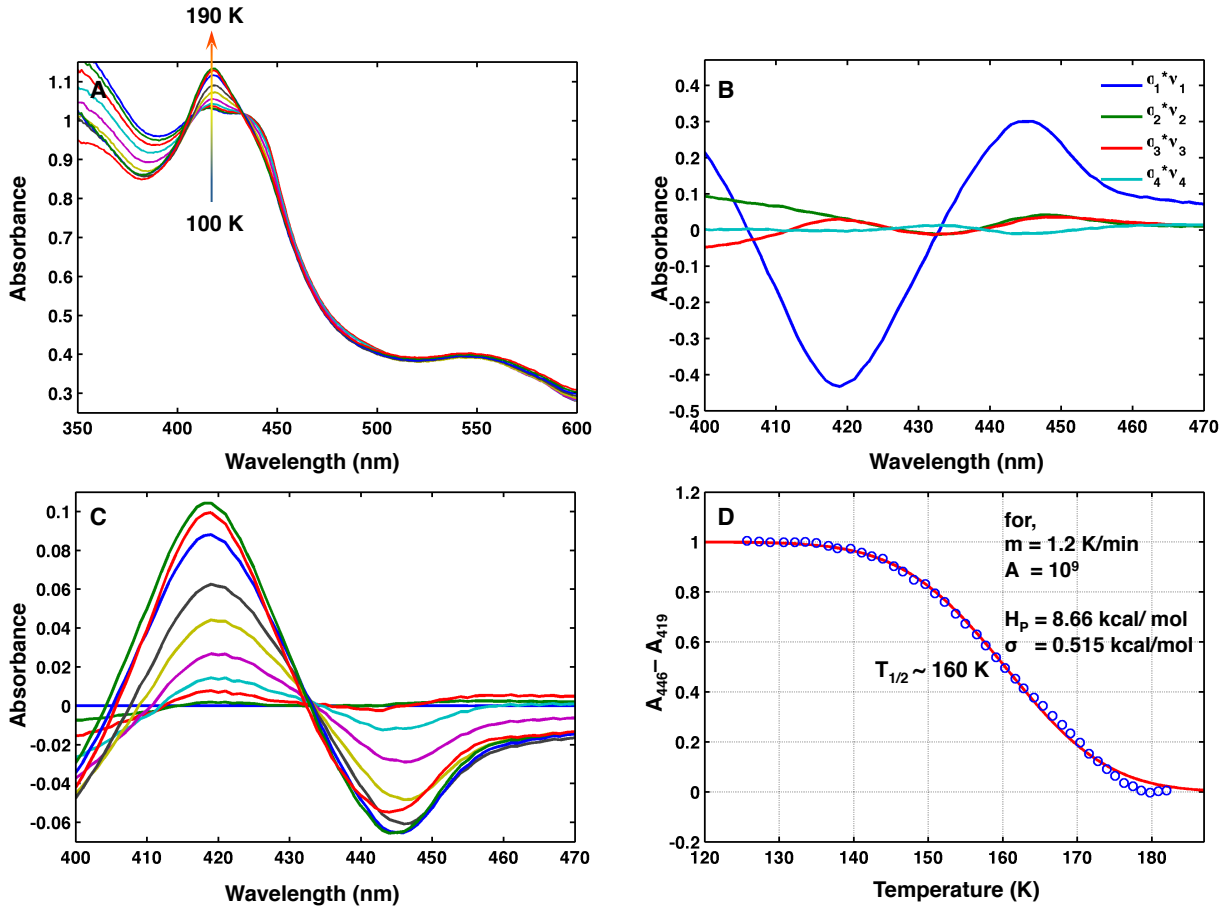

Figure 22: A) Proxy annealing of CYP101 D251N in protiated aqueous glycerol solution as studied by Temperature Derivative Spectroscopy (TDS). B) Normalized eigen vectors from singular value decomposition of the optical absorption data set. C) svd reconstructed difference spectra. D) Decay of the reduced ox-ferrous complex as monitored by the change in absorbance corresponding to conversion of the proxy species to low-spin ferric P450. The blue dots represent actual data points whereas the red line shows the fit obtained using a distributed energy barrier model.

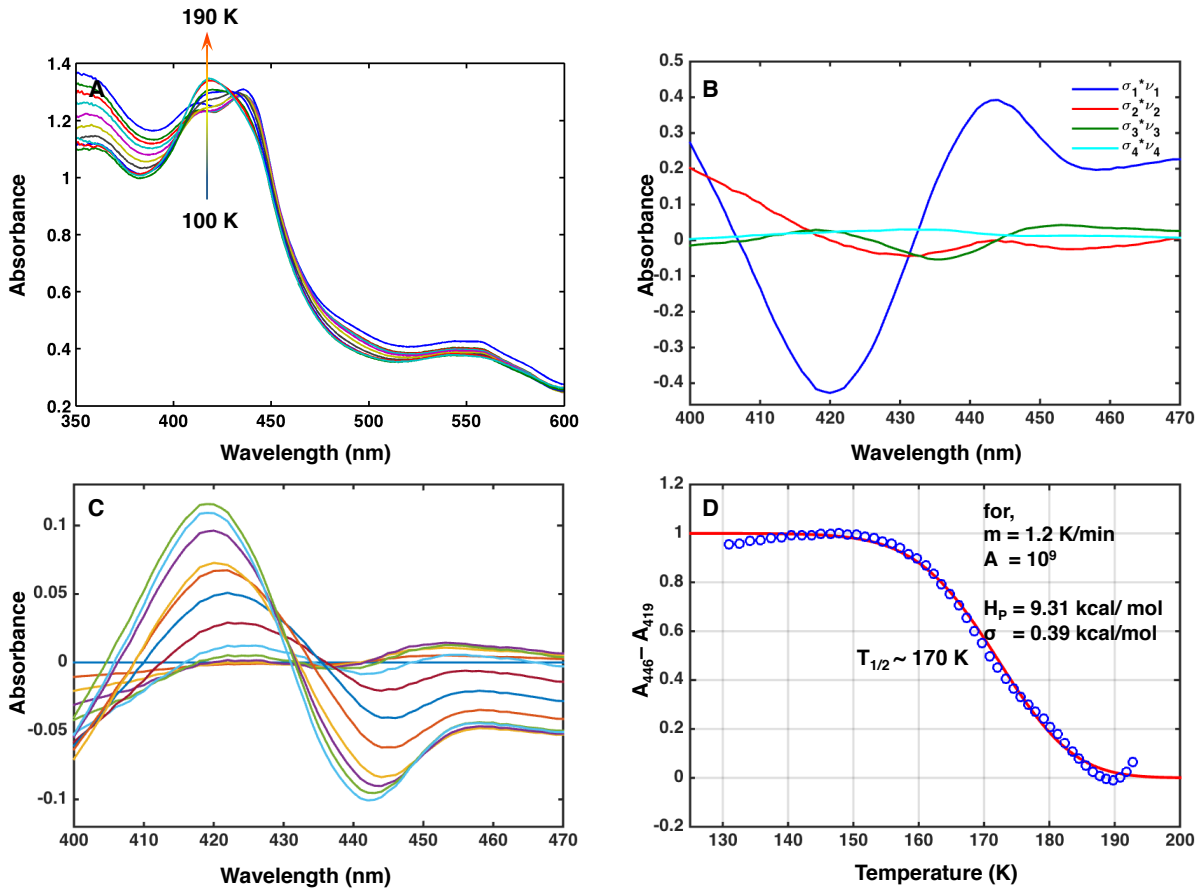

Figure 23: Proxy annealing of CYP101 D251N in deuterated aqueous glycerol solution as studied by Temperature Derivative Spectroscopy (TDS). B) Normalized eigen vectors from singular value decomposition of the optical absorption data set. C) svd reconstructed difference spectra. D) Decay of the reduced ox-ferrous complex as monitored by the change in absorbance corresponding to conversion of the proxy species to low-spin ferric P450. The blue dots represent actual data points whereas the red line shows the fit obtained using a distributed energy barrier model.

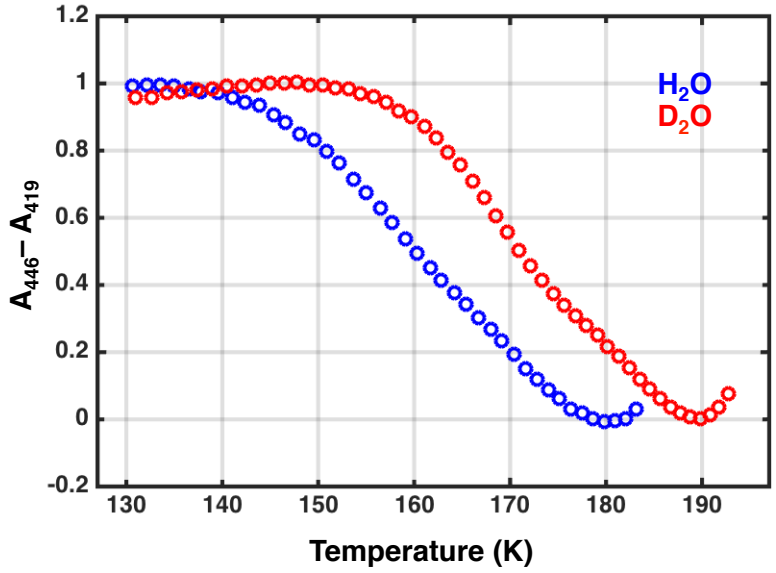

Figure 24: Peroxo annealing profiles of CYP101 D251N in protiated and deuterated aqueous glycerol solvents superimposed. A higher temperature of half transition in D_2O (i.e. ~ 170K) compared to that in H_2O (~ 160K) indicates the presence of a kinetic solvent isotope effect in the peroxo annealing of D251N mutant of CYP101.

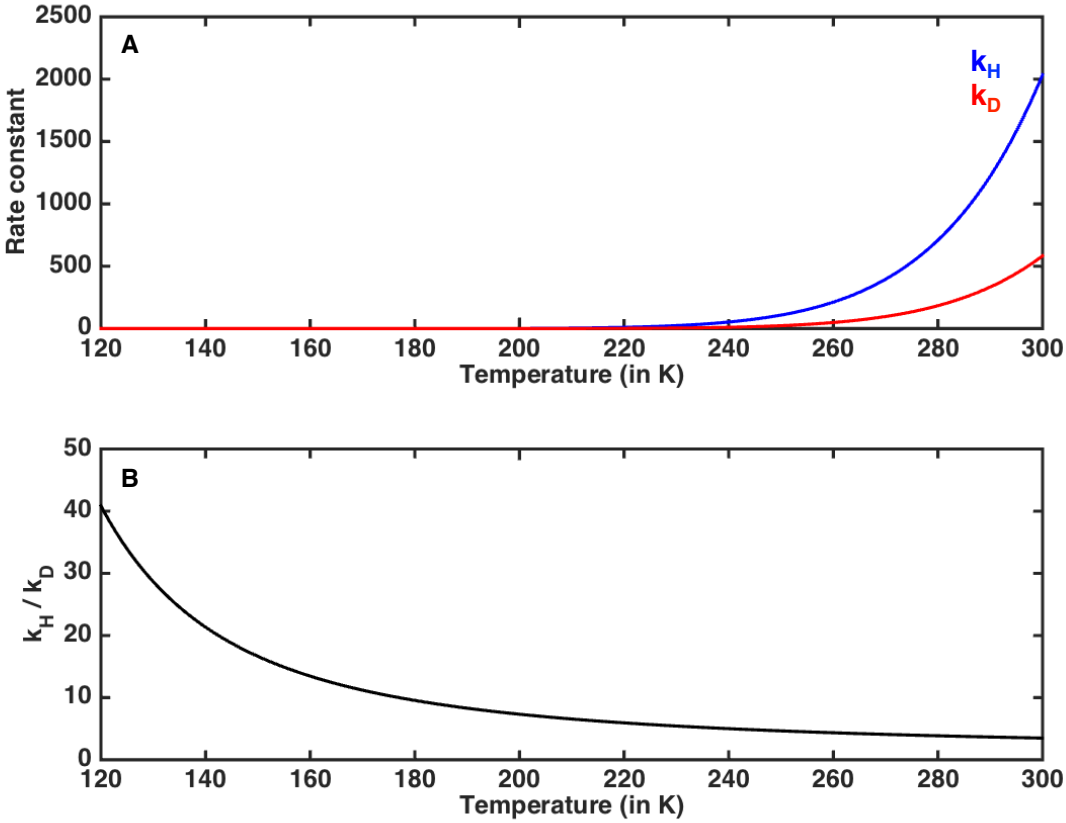

Figure 25: Temperature dependence of KSIE in CYP101 D251N. A) Rate constants corresponding to the decay of peroxo species in protiated and deuterated solvents, and B) their ratio as a function of temperature.

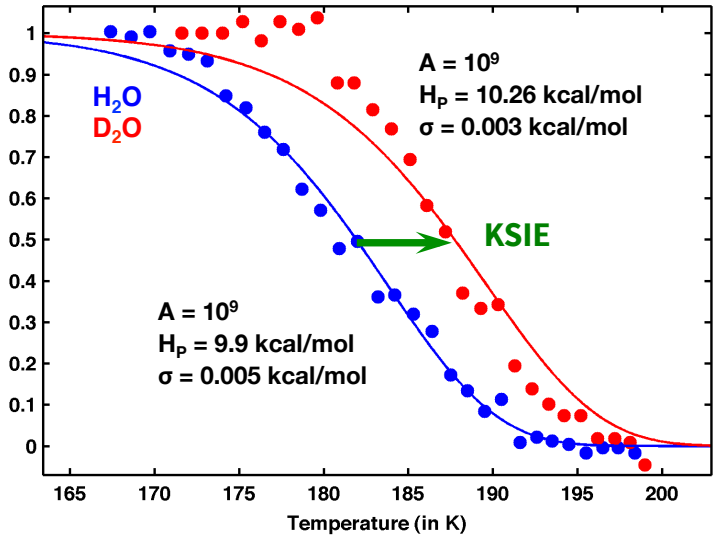

Figure 26: Optical annealing reduced oxy-ferrous complex of 19-oxo-AD bound CYP19A1 in protiated and deuterated aqueous glycerol solvent systems.

Chapter 4: Probing the Iron-Oxygen Intermediates of Human Aromatase Using Electron Paramagnetic Resonance (EPR) Spectroscopy and Electron Neutron Double Resonance (ENDOR) Spectroscopy

INTRODUCTION

Electron paramagnetic resonance (EPR) is the phenomenon of resonant absorption of microwave radiation by a paramagnetic species when subjected to an external magnetic field. EPR spectroscopy relies on the splitting of the otherwise degenerate energy levels of electrons upon application of an external magnetic field. Every electron has a spin quantum number and associated magnetic components of value +½ or -½. In the presence of an external magnetic field, the electron's magnetic moment (m_s) aligns itself in either parallel or anti-parallel orientation with respect to the field. The specific energy, E of an electron in each of these states is directly proportional to m_s and the strength of the applied magnetic field, B_0. An unpaired electron can move between these two energy levels by either absorbing or emitting a photon of energy $h\nu$. According to Maxwell-Boltzmann distribution more molecules have electrons populating the lower energy level than the higher energy level so, there is a net absorption of energy. The resonance condition at which ΔE equals $h\nu$ (obtained by varying B_0 at a fixed ν usually) results in a positive signal in the 'absorption versus B_0' plot as the magnetic field is varied keeping the frequency of incident photons fixed. 'g' factor relates the resonant frequency of incident photons and the magnetic field, B_0. Interaction of the electron spin with local magnetic moments of nuclear spin (spin-orbit coupling) causes a deviation in g-value from that of a free electron. The magnitude of the change gives information about the nature of the atomic or molecular orbital containing the unpaired electron. Splitting of EPR spectral lines, referred to as hyperfine coupling, and line width provide information about neighboring nuclei and their degree of interaction with the paramagnetic center under investigation (Lancaster 1967; Pilbrow & Hanson 1993).

ENDOR spectroscopy provides the NMR spectrum of nuclei that interact with the electron spin of the paramagnetic center. When placed in a magnetic field, NMR active nuclei absorb electromagnetic radiation at a frequency characteristic of that isotope. In ENDOR, a radio-frequency field is applied simultaneously with the microwave field and NMR transitions are detected as

change in the EPR signal intensity of the paramagnetic center rather than directly. The term "double resonance" comes from the fact that we have "EPR-detected" NMR in this case (Hoffman 1991).

ENDOR increases the resolution of the EPR spectra of a paramagnetic species under study by adding an extra layer of NMR data to the existing EPR spectra. ENDOR signals arise from interaction of the paramagnetic species with nearby magnetic nuclei belonging to the molecule on which the unpaired electron is localized or the surrounding molecules. The strength of hyperfine coupling and nuclear quadruple interaction are related to the electron spin and the charge density distribution of the molecule respectively and therefore and thus help discern the structure and organization of the paramagnetic center (Kulik & Lubitz 2009; Kispert & Piekara-Sady 2006).

Electron paramagnetic resonance, in conjunction with electron neutron double resonance (ENDOR) spectroscopy has proved to be an important tool for the elucidation of structural and electronic details of many a metal coordinated biological complexes (Van Doorslaer & Vinck 2007). Among the transition metals found in proteins, iron has the richest variety of EPR spectra and therefore, EPR and ENDOR spectroscopy has been applied heavily to study hemeproteins including cytochromes P450 as described below.

EPR of reduced oxy-ferrous complexes

Davydov et al. reported the first EPR and ENDOR spectra of P450 peroxo intermediate states prepared by cryoradiolysis using ^{60}Co γ-irradiation (Davydov et al. 1991). Using wild-type CYP101 and its mutants D251N and T252A Davydov et al. were able to identify and characterize the unprotonated and protonated peroxo species in this bacterial P450 (Davydov et al. 2001). The EPR spectra of the (hydro)peroxo complexes of CYP101 were found to be similar to those reported for the same complexes in hemoglobin, myoglobin and horse radish peroxidase, and fall within a narrow span of g-values [2.3–2.25, 2.2–2.14, 1.94–1.97] (Davydov 1980; Kappl et al. 1985; Leibl et al. 1986; Symons & Petersen 1978).

This study also helped develop an understanding of the role of the T252-D251N acid-alcohol pair of CYP101 in proton delivery. It was noted that in WT and T252A mutant CYP101 the hydroperoxo anion, [5b] of Figure 2 is observed as the primary product of cryoradiolysis whereas, D251N yields the peroxo anion, [5a] of Figure 2. Additionally, it was observed that cryoreduced oxyCYP101/T252A did not yield product like the wild-type enzyme. Since the hydroperoxo anion lies at the lies at the intersection of the productive arm of the P450 catalytic wheel and the peroxide shunt, whereby the Fe-O bond is cleaved and the bound O-O moiety is lost as H_2O_2 it was concluded

the that threonine-252 in CYP101 participates in delivery of the second proton to the distal oxygen of the hydroperoxo anion that ultimately leads to the formation of Cpd 1. Cryoradiolysis of oxyCYP101 D251N yields the peroxo anion at 77K which gives product upon annealing that this residue is important for the first protonation step (Davydov et al., 2001).

Via the application of ^{1}H ENDOR spectroscopy on oxy-complexes of wild-type and mutant CYP101 upon cryoradiolysis and subsequent thermal annealing the same study afforded identification and delineation of exchangeable protons into covalently bonded or hydrogen bonded and provided strong evidence for the involvement of a high-valent oxo-ferryl intermediate, namely Cpd 1 for product formation.

Recognizing the power and utility of EPR and ENDOR spectroscopy in realizing cytochrome P450 mechanism, this chapter describes my effort and its fruits toward the spectroscopic characterization of cryoreduced oxy-complexes of CYP19A1 in the presence of AD- and 19-oxo-AD, substrates for the hydroxylation and aromatization steps of CYP19A1 respectively. The rationale being that stepwise thermal annealing of these complexes will allow us to examine the conversion of the heme-peroxo anion to product asking the question – is the protonated hydroperoxo state generated prior to formation of the aromatic product? For Step III of CYP19A1 catalysis, the hydroperoxo intermediate is not expected to form if CYP19A1 utilizes the Cpd 0 mechanism, while the formation of the hydroperoxo intermediate would be essential for generation of the oxo-ferryl species in the potential Cpd 1 mechanism.

This work was done in collaboration with Roman Davydov of Prof. Brian Hoffman's group at Northwestern University.

MATERIALS AND METHODS

Expression, purification and Nanodisc incorporation of CYP19A1

The expression, purification and incorporation of CYP19A1 into POPC Nanodiscs was performed as previously described in pages 7 and 10.

Preparation of EPR samples

A 100 µl solution containing 500 µM CYP19 in Nanodiscs, 700 µM Androstenedione, 125 µM methylviologen and 15% glycerol in 100 mM phosphate buffer, pH 7.4 was deoxygenated in a 1-ml glass vial fitted with a rubber septa by passing a gentle stream of Argon over it, under rotation, for 4 minutes and reduced using 2.5 Molar equivalents of sodium dithionite. In an EPR tube, 150 µl of

solution containing 100 mM phosphate buffer pH 7.4, 75% glycerol, 700 μM Androstenedione was taken and cooled to a temperature of -30 °C in a dry-ice ethanol bath. The reduced protein solution was rapidly injected into the EPR tube containing pre-chilled oxygenated buffer using a 500 μl gas-tight Hamilton syringe fitted with an 8"-long 22-gauge needle. The solution was mixed for 30 seconds and transferred to another dry-ice ethanol bath maintained at -60 °C. Once cooled the tube was transferred to liquid nitrogen, immersing it slowly to prevent cracking. D_2O samples were prepared in a similar fashion except all the buffers used were prepared in D_2O and the protein used was exchanged into a D_2O (Cambridge Isotope Laboratory Inc.) buffer via repeated rounds of concentration and dilution in a 10,000 MWCO 500 μl Amicon centrifugal filter.

An alternate route of oxygenation was followed for producing oxy-complexes of 19-oxo AD bound CYP19A1. A 250 μl solution containing 200 μM CYP19A1, 5 μM methylviologen, 500 μM 19-oxo AD (from a 25 mM stock solution, so methanol added is ≤ 2% of total volume of solution) and 30% glycerol in 100 mM phosphate buffer pH 7.4 was deoxygenated in a 1-ml glass vial fitted with a rubber septa by passing a gentle stream of Argon over it, under rotation, for 1 minute and reduced with 2.5 molar excess of sodium dithionite solution inside an anaerobic chamber (Dithionite was added from a stock solution of concentration ≥ 15 mM in anaerobic 100 mM phosphate buffer pH 7.4 to keep the volume added to the minimum). The reduced protein solution was let to sit in the vial for 10 minutes, after which it was transferred to a EPR tube using a 500 μl gas-tight Hamilton syringe fitted with a 8"-long 22-gauge needle. The top of the EPR tube was sealed with a rubber septa, enclosed in a glass cylinder and brought outside where it was cooled to -14 °C in a dry-ice ethanol bath. Oxy-ferrous complexes were formed by bubbling $^{16}O_2$ for 4-5 seconds followed by rapid cooling in a -60 °C dry-ice ethanol bath. The samples were then flash frozen and stored in liquid N_2. D_2O samples were prepared similarly.

Reduced oxy-ferrous complexes were obtained upon γ-cryoradiolysis of oxy-ferrous samples at 77K using a total dose of 3.5 MRad from a ^{60}Co source.

EPR CHARACTERIZATION OF REDUCED IRON-OXYGEN INTERMEDIATES OF CYP19A1

X-band EPR spectra were recorded on a modified Varian E-4 spectrometer at 77 K. Q-band (35 GHz) EPR and ENDOR spectra were recorded on a modified Varian E-110 spectrometer equipped with a helium immersion dewar at Northwestern University by Roman Davydov.

To follow the progression of cryotrapped reduced oxyferrous complexes of CYP19A1 upon thermal annealing, cryoreduced samples were annealed to temperatures by transferring the EPR tubes from

liquid nitrogen to a bath at fixed temperature for 1 minute, after which the sample was transferred back to liquid nitrogen.

RESULTS AND DISCUSSION

EPR of reduced AD-bound-oxyCYP19A1

It was shown earlier that in AD-bound CYP19A1 the first intermediate that accumulates during low temperature oxygenation and subsequent cryoreduction of the thus formed oxy-complex is an unprotonated peroxo-ferric heme (Gantt et al. 2009). This suggested that the proton delivery pathway is more hindered in CYP19A1 in the presence of AD than in most other P450s and perhaps the same intermediate acting as a nucleophile could conduct the aromatization reaction via an attack on the electrophilic carbonyl of 19-oxo-AD when present.

This work conclusively showed the presence of peroxo-anion however, lacked proper resolution to trace the evolution of this intermediate to the product complex. In collaboration with Roman Davydov of the Hoffman group at Northwestern University, this experiment was repeated (see Figure 27) and the following observations were made:

- The primary intermediate obtained upon cryoreduction of AD-bound oxy-CYP19A1 gave a g_1 of 2.263 at 160 K consistent with the presence of an unprotonated peroxo anion as reported earlier (Gantt et al. 2009).
- Upon annealing to 180 K a new intermediate with g = [2.41, 2.45] was obtained. Furthermore, this species showed a kinetic solvent isotope effect (KSIE) of greater than 3.5. This suggests the presence of a protonation step in the decay of this species.
- Upon further annealing to 210 K, an initial product complex at g = 2.40 is observed.

Figure 28 provides a schematic representation of the sequence of events described above.

The acid-alcohol pair along with water molecules in the active site of P450s form an elaborate hydrogen-bonding network that supplies the two protons necessary for formation of the hydroperoxo-anion and subsequently, Compound 1. The observation of an unprotonated peroxo intermediate in CYP19A1 suggests that the proton delivery pathway in CYP19A1 is somewhat impeded. A comparison between the structures of CYP19A1 and CYP101 provides a potential explanation. Upon oxygen binding to ferrous CYP101, Asp251 produces a conformational change in the I-helix that helps order two water molecules and Thr252 at the active site for efficient dioxygen activation (Nagano & Poulos 2005). Asp309 in CYP19A1 is positioned slightly differently than its

CYP101 analogue. In CYP19A1, Asp309 is engaged in H-bonding interaction with the 3-keto group of the substrate molecule and is not available as freely as in CYP101 (Ghosh et al. 2009).

Density functional theory calculations suggest a 7 kcal/mol difference in the energy barrier for H1β abstraction when the A-ring of the steroid is 2,3 enolized as opposed to when its not (Hackett et al. 2005). Asp-309's direct role in catalysis via enolization may mean that its active site orientation is not optimal for proton delivery and explains the experimental observations discussed above.

EPR and ENDOR of reduced 19-oxo-AD-bound-oxyCYP19A1

If the peroxo-anion hypothesis is true one would expect to see peroxo-anion in the 19-oxo-AD bound reduced oxy-complex as well. In contrast to AD-bound enzyme, EPR characterization of cryoreduced 19-oxo-AD bound oxy-CYP19A1 shows the accumulation of the hydroperoxo anion as the primary species with g-values of 2.28 and 2.33. (Figure 29). The ^{1}H ENDOR spectra of g = 2.3 shows H/D variability and provides further evidence that the species at g = 2.3 corresponds to the hydroperoxo anion (Figure 30).

Upon annealing, the species at g = 2.28 diminishes and a new species at g = [2.43, 2.5] emerges. ENDOR spectra of cryoreduced 19-oxo-AD bound oxyCYP19A1 shows the presence of exchangeable protons suggesting that this species is the resting ferric aquo-heme. The species with g = 2.33 is hypothesized to be a minor conformation of the hydroperoxo anion. However, the annealing behavior of this g = 2.33 species is different to the main g = 2.28 peak and warrants further investigation. Beyond 215 K a species with g = [2.43, 2.25] is obtained. This presumably corresponds to the ferriheme complex but remains to be verified independently (Davydov et al. 2001).

CONCLUSION

Because of the challenges associated with producing reduced oxy-samples with signal-noise ratios conducive to annealing type experiments, further experiments planned in this direction could not be completed before preparation of this thesis. However, in repeated attempts to trap and characterize the annealing behavior of the reduced 19-oxo-AD bound oxyCYP19A1 via EPR, including the data presented here, it was conclusively shown that the primary species obtained in this case was the protonated peroxo anion. This observation contradicts the Cpd0 mechanism for the aromatization step of CYP19A1 wherein the peroxo anion acting as a nucleophile attacks the

carbonyl carbon at C19 position of the 19-oxo-AD intermediate and orchestrates the C-C lyase and aromatization reaction and tips the scales in the favor of Cpd1 mediated catalysis (page 6).

In our experiments with reduced AD-bound oxyCYP19A1, we confirmed the presence of the peroxo anion as the primary intermediate and discovered a previously undiscovered intermediate with g = [2.41 2.45]. We hypothesize that this new intermediate is the product complex still bound to the heme-iron of water-ligated complex in some non-equilibrium conformation.

In conclusion, our experiments suggest that in CYP19A1 the C-C scission and aromatization is mediated by the archetypical Cpd1 mediated H-rebound mechanism as opposed to a Cpd0 mediated.

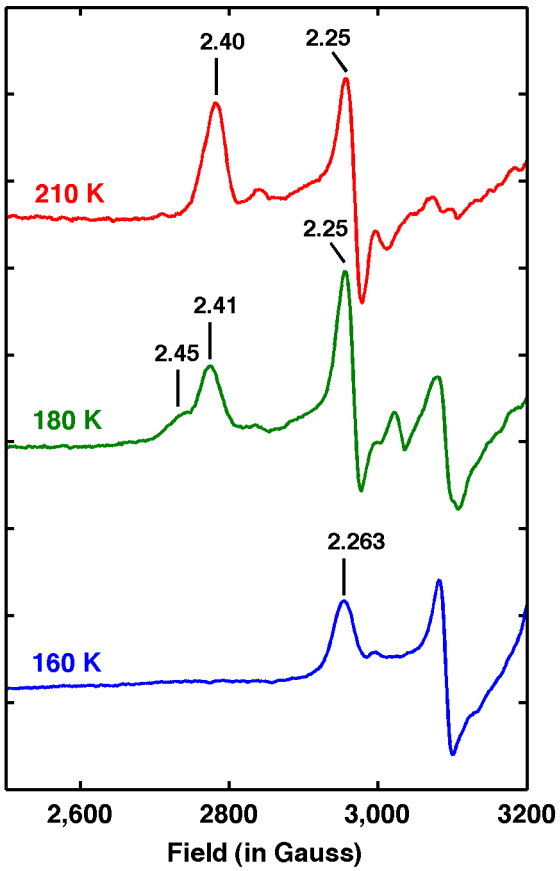

Figure 27: EPR annealing of cryoreduced AD-bound oxy-CYP19A1

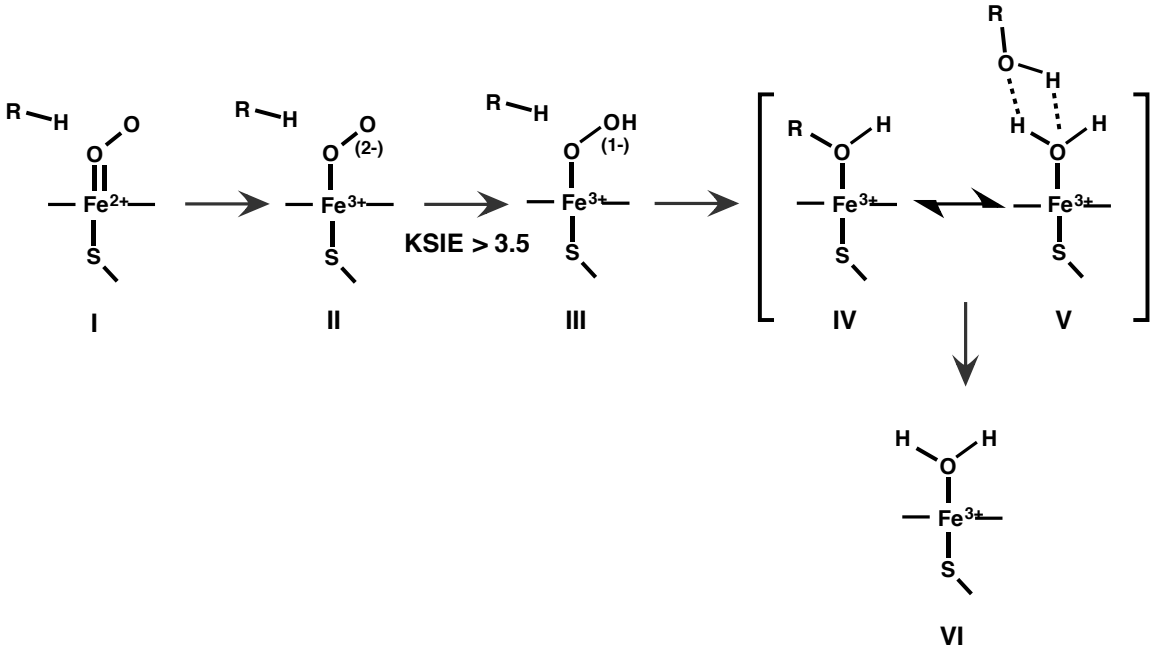

Figure 28: Schematic representation of the sequence of events observed upon EPR annealing of cryoreduced AD-bound oxy-CYP19A1

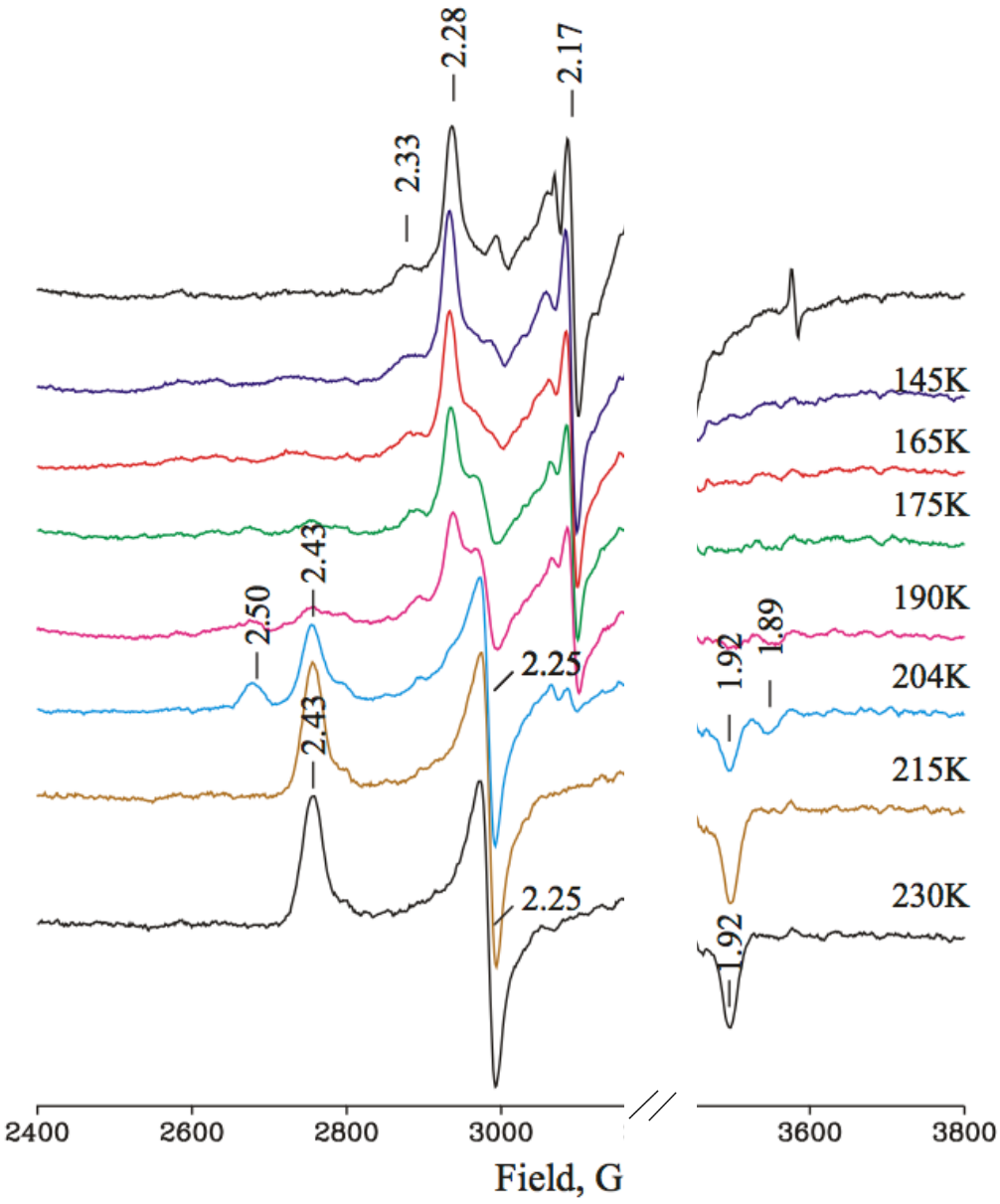

Figure 29: EPR annealing of cryoreduced 19-oxo-AD bound CYP19A1

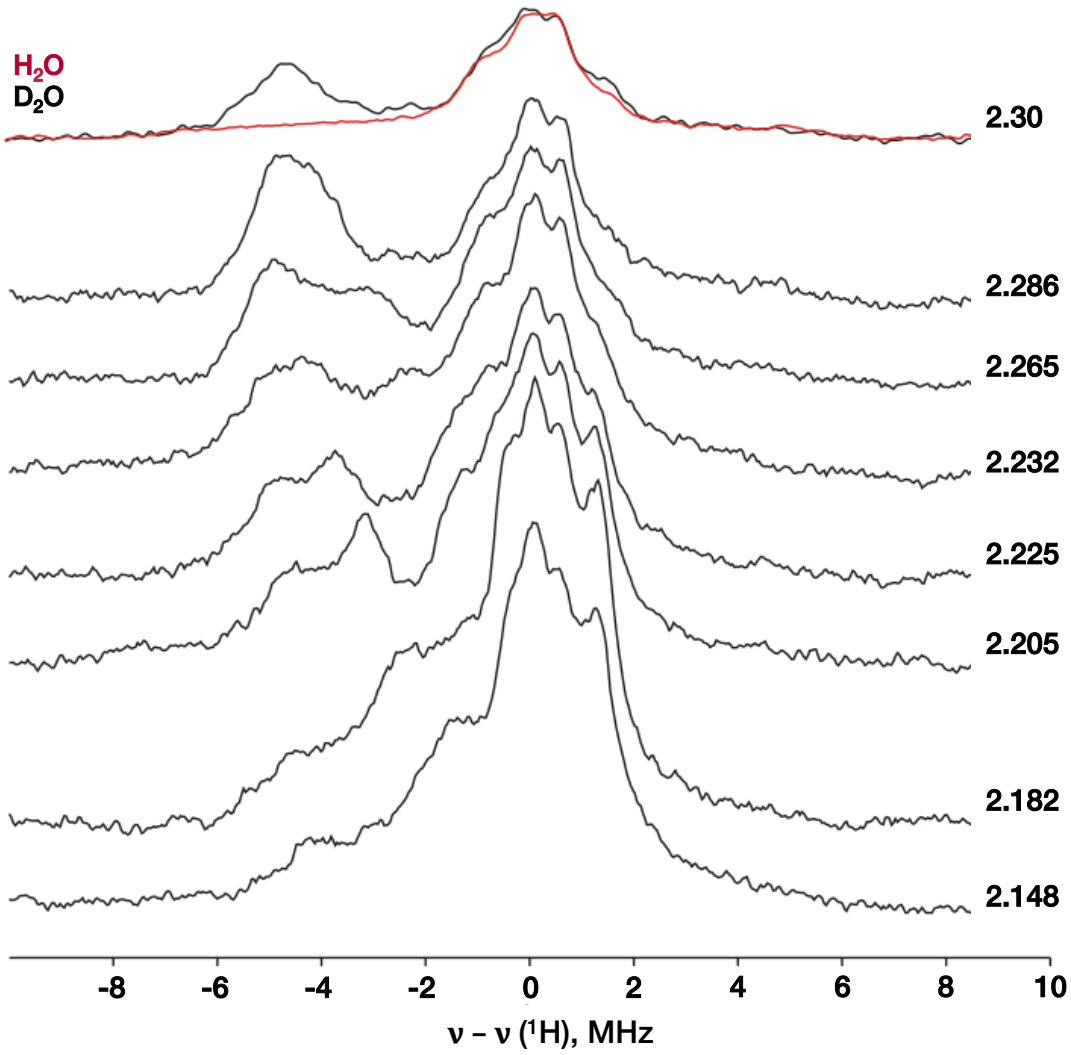

Figure 30: ^{1}H ENDOR spectra of g_1 = 2.3 species of cryotrapped reduced 19-oxo-AD bound oxyCYP19A1

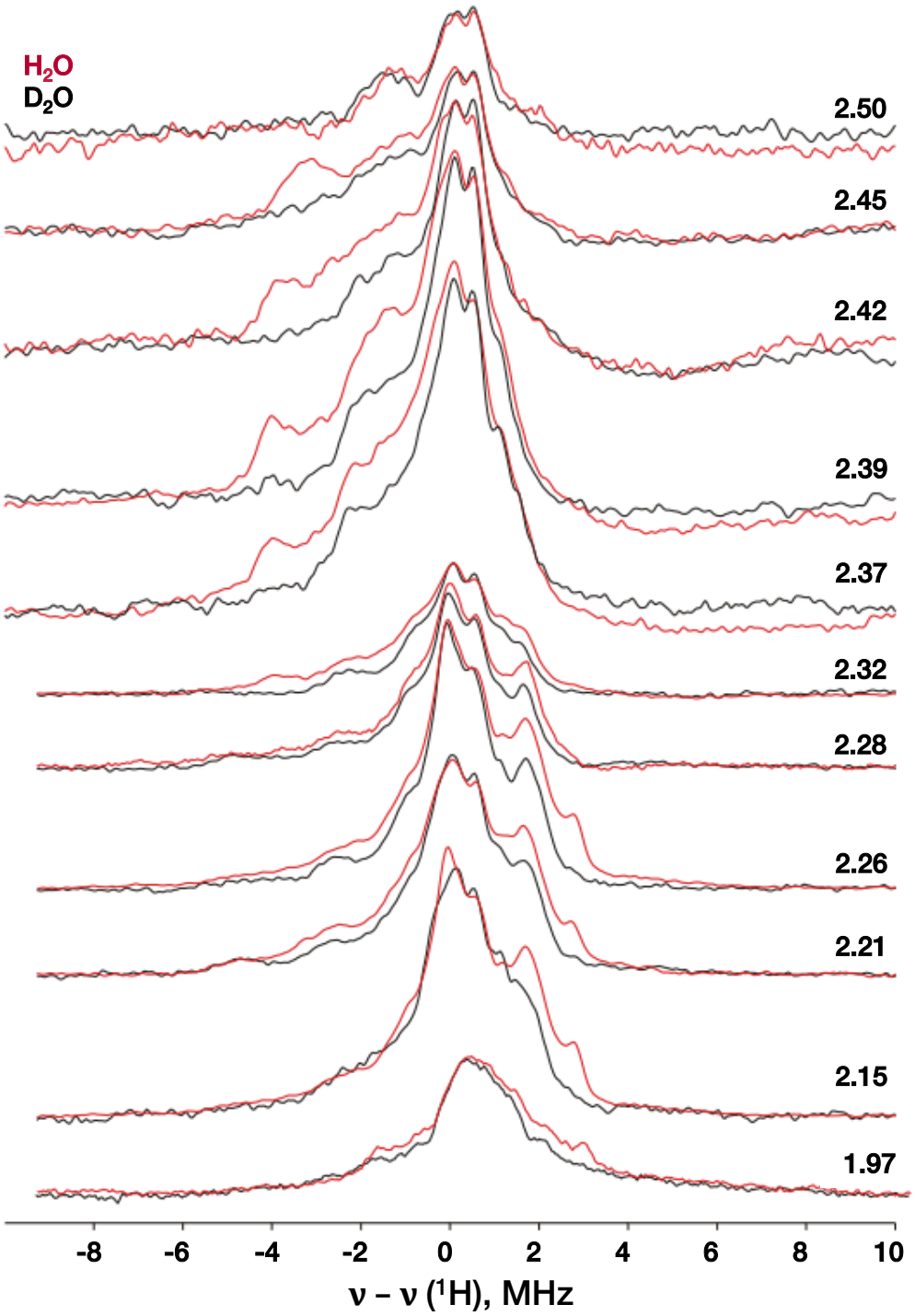

Figure 31: ENDOR spectra of the cryoreduced 19-oxo-AD bound oxyCYP19 annealed at 204K showing the presence of exchangeable protons suggesting that the species observed at 204K [g = 2.43, 2.5] is the resting ferric aquo-heme.

Chapter 5: RR Characterization of Ferric, Oxy-ferrous and Reduced Oxy-ferrous Complexes of Substrate-bound CYP19A1

INTRODUCTION

Raman spectroscopy is a type of vibrational spectroscopy that reports the transition between different vibrational levels in a molecule upon excitation by incident light from a laser beam. Photons from the exciting light excite the molecule in its ground state to a virtual excited state. When the molecule relaxes, it emits a photon and returns to a different vibrational level of the ground state. The reemitted photon lies at a frequency either higher or lower than that of the exciting beam, this is referred to as the 'Raman effect'. In resonance Raman, the wavelength of the exciting laser line is tuned to coincide with an allowed electronic transition. This allows the vibrational modes corresponding to that particular transition to be intensified compared to the off-resonance values making the rR technique more sensitive to its off-resonance (normal Raman) version. This aspect becomes especially useful for biomolecules with chromophores in embedded in them, such as cytochromes P450. A heme prosthetic group forms the heart of the enzymes' catalytic activity. Tuning the laser to the charge transfer transition of the heme group enhances iron-ligand stretching modes and some modes associated with the ligand alone. rR is a powerful tool to study the heme environment in a P450. Porphyrin skeletal vibrations provide information about the coordination geometry and spin-state of the heme iron (Spiro & Czernuszewicz 1995). Vibrations associated with CO in the ferrous-CO adduct help characterize the heme distal site and property of an axial ligand (Spiro & Wasbotten 2005) whereas the Fe-S stretch serves as a structural marker for the heme proximal site.

Recently, RR has been used to substrate induced structural changes in the active site of human CYP3A4 (Mak et al. 2011) and human CYP17 (Mak et al. 2014); characterize the oxy-ferrous complexes of CYP17 especially in terms of their H-bonding geometry (M. Gregory et al. 2013) and characterize the peroxo and hydroperoxo states of CYP101 (Denisov et al. 2008). These studies underscore the applicability and value of rR in studying various arms of the P450 catalytic wheel, particularly the reactive and perhaps more interesting oxy-ferrous and peroxo states.

This chapter outlines the application of rR for structural characterization of human CYP19A1 in Nanodiscs in the presence of AD, 19-OH AD and 19-oxo AD in its ferric and oxy-ferrous states to identify features that could in turn help us identify the reactive intermediate involved in the hydroxylation and C-C lyase chemistries. AD and 19-OH AD undergo hydroxylation whereas 19-oxo AD undergoes C-C scission and aromatization, two very different chemical reactions occurring at the same active site. Structural differences between AD- and 19-oxo AD-bound CYP19A1 or the lack thereof may shed some light on how these seemingly diverse chemical transformations occur at the same active site and lift the cloud of mystery surrounding the identity of heme-oxygen intermediate responsible for catalysis in both these cases.

The resonance Raman characterization of CYP19A1 in its various substrate bound states has been performed before. Tosha et al. (Tosha et al. 2006) measured the rR spectra of substrate-bound CYP19A1 and discovered substrate induced changes in the heme environment in both the distal and proximal side. They also found evidence of reduced electron donation from the axial thiolate to the heme iron in the presence of 19-oxo-AD and favored the Cpd0 mechanism for C-C lyase (page 6) arguing that the reduced axial electron donation may stabilize the ferric peroxo anion and suppresses the formation of Cpd1 in the presence of this substrate. However, these measurements were done using detergent solubilized CYP19A1 and were subject to limitations of non-specific protein aggregation and non-native protein conformational state of the membrane protein. There was a also substantial amount of P420 in the enzyme preparation leading to erroneous observations as pointed out later.

The rR experiments described in this chapter were done with CYP19A1 incorporated in MSP1D1-POPC Nanodiscs. By providing a native membrane-like environment to the membrane-bound P450 Nanodiscs help preserve the enzyme's structural and functional characteristics and provide a better representation of spin-state populations, substrate binding and stability of dioxygen adducts and peroxo complexes.

This work was done in collaboration with Piotr Mak of Prof. James Kincaid's group at Marquette University. I prepared the oxy-complexes and reduced oxy-complexes in different substrate bound and solvent states whereas, Piotr Mak conducted the rR experiments and analyzed data. Data interpretation and manuscript synthesis was done collectively.

PREPARATION OF OXY-FERROUS AND REDUCED OXY-FERROUS COMPLEXES FOR RR SPECTROSCOPY

CYP19A1 substrates

Androstenedione (AD) and 19-oxo-AD (19oxoAD) were purchased from Sigma-Aldrich and Steraloids, respectively, and were used as a 25 mM stock solution in methanol.

Protein expression, purification and incorporation into Nanodiscs

The expression, purification and incorporation of CYP19A1 into POPC Nanodiscs was performed as previously described in pages 7 and 10.

Preparation of oxy-samples for rR measurements

70 μL of 250 μM ferric CYP19A1, 6.25 μM methylviologen (Sigma-Aldrich), 500 μM substrate, 30 % (v/v) glycerol (or glycerol-d3 where appropriate) in 0.1 M potassium phosphate, pH 7.4 was de-aerated under a continuous flow of Argon for 5 minutes in a small glass vial. The protein was reduced with a 2.5 fold molar excess of sodium dithionite (Riedel-de Haën AG, Germany) and transferred to 5 mm O.D. NMR tubes (WG-5 Economy, Wilmad) under anaerobic conditions. After incubation at room temperature for 10 minutes the reduced sample was cooled down in a dry ice-ethanol bath to -13 °C for 1 minute. Oxy-ferrous complexes were formed by bubbling $^{16}O_2$ or $^{18}O_2$ gas for 3-5 seconds, followed by rapid cooling in a -60 °C dry ice-ethanol bath. The samples were then flash frozen and stored in liquid N_2 until measurement.

rR measurement

Ferric complexes

The samples of ferric CYP17 samples were measured using the 406.7 and 356.7 nm excitation lines from a Kr+ laser (Coherent Innova Sabre Ion Laser). The rR spectra were collected in the back-scattering geometry using a Spex 1269 spectrometer equipped with Spec-10 LN-cooled detector (Princeton Instruments, NJ). The laser power was adjusted to ~10 mW and all measurements were done at room temperature. Spectra were calibrated with fenchone (Sigma-Aldrich, WI) and processed with Grams/32 AI software (Galactic Industries, Salem, NH).

Oxy-ferrous complexes

The resonance Raman spectra of oxy complexes of ND:CYP19 were acquired using a Spex 1269 spectrometer equipped with a Spec-10 LN-cooled detector (Princeton Instruments, NJ). The data

were measured with 413.1 nm excitation line from a Kr+ laser (Coherent Innova Sabre Ion Laser). The rR spectra were collected using back scattering (180°) geometry with the laser beam being focused by a cylindrical lens to form a line image on the sample. The laser power was adjusted to 1 mW or less. All measurements were done at 77 K and total collection time was 3-4 hours in the high frequency region and 4-5 hours in the low frequency region. The slit width was set at 150 μm and the 1200 g/mm grating was used. The NMR tubes were positioned into a double-walled quartz low temperature cell filled with liquid nitrogen. The sample tubes were spun to avoid local heating. Spectra were calibrated with fenchone (Sigma-Aldrich, WI) and processed with Grams/32 AI software (Galactic Industries, Salem, NH).

RESULTS AND DISCUSSION

AD-, 19-OH-AD and 19-oxo-AD bound ferric CYP19A1

Although the structure of AD-bound CYP19A1 was a significant advancement in the field of aromatase research it did not offer any clues as to the whether the substrate itself can alter the enzyme's active site and therefore affect its own catalysis as seen in CYP17 (Mak et al. 2014). Moreover, no structural information was available for 19-oxo-AD bound CYP19A1, the substrate for the lyase step of CYP19A1. To address these deficiencies resonance Raman was used to probe the active site of CYP19A1 and study its interaction with its three substrates, AD, 19-OH-AD and 19-oxo-AD. By monitoring the oxidation and spin state marker bands and Fe-S stretches in different substrate binding configurations one can study changes occurring in both the distal and proximal side of heme iron upon substrate binding.

Figure 32 shows the high-frequency rR spectra of ferric CYP19A1 in substrate-free and substrate-bound states. The high frequency region contains core size and spin-state markers and provides information about the oxidation state and the spin-state of the heme iron. For substrate-free CYP19A1, the oxidation state marker band ν_4 and the spin state marker bands ν_3, ν_2 and ν_{10} are observed at 1374 cm^{-1}, 1501 cm^{-1}, 1583 cm^{-1} and 1638 cm^{-1} respectively. This is characteristic of a low-spin, hexa-coordinated ferric heme and indicates that substrate-free CYP19A1 is pure low-spin (Champion et al. 1978). Substrate binding results in a change in coordination geometry (6-coordinated to 5-coordinated) and spin state (low-spin to high-spin) of the heme-iron. Full spin state conversion from low-spin in substrate-free P450s to high-spin in substrate-bound P450 is seen as a 14-17 cm^{-1} downshift of all three spin state marker bands (Mak, Im, et al. 2008; Mak et al. 2011; Mak et al. 2014; Mak, Kaluka, et al. 2008). High-frequency rR spectra of substrate-bound

CYP19A1 shows peaks at 1485 cm^{-1} ($\nu_{3, HS}$), 1501 cm^{-1} ($\nu_{3, LS}$); 1568 cm^{-1} ($\nu_{2, HS}$), 1583 cm^{-1} ($\nu_{2, LS}$); and 1621 cm^{-1} ($\nu_{10, HS}$), 1638 cm^{-1} ($\nu_{10, LS}$) for all three substrates. The ratios of intensities of $\nu_{3,LS}$ and $\nu_{3,HS}$, proposed to represent percent spin-state conversion in P450s by Mak et al. (Mak et al. 2013), correspond well with spin state conversion observed using optical spectroscopy in the case of CYP19A1 as well (Table 1).

Figure 33 shows the low-frequency rR spectra of CYP19A1. Low-frequency modes in P450s are sensitive to changes in the heme-macrocycle or peripheral substituents produced as a result of changes in the active site such as those produced upon substrate binding (Hu et al. 1996; Mak et al. 2004; Mak, Kaluka, et al. 2008).

The ν_7 and ν_8 modes are observed at 675 cm^{-1} and 345 cm^{-1}. Low-frequency rR spectra of substrate-free CYP19A1 shows propionate bending modes at 369 cm^{-1} and 376 cm^{-1}, as well as two vinyl bending modes at 407 cm^{-1} and 430 cm^{-1}. AD binding has no effect on propionate bending modes but causes a 8 cm^{-1} downshift of the higher frequency vinyl bending mode. AD binding also causes an activation of the ν_7 mode. Similar behavior is seen upon binding of 19-OH-AD and 19-oxo-AD.

19-OH AD binding causes a decrease in the intensity of the propionate bending mode at 369 cm^{-1} but no change in the intensity of the band at 376 cm^{-1}. 19-oxo AD binding causes an increase in the intensity of the 376 cm^{-1} band. It has been shown that the frequency of the propionate-bending mode is sensitive to hydrogen-bonding with the protein environment and that disruption of H-bonding causes a decrease in propionate bending frequency by ~ 10 cm^{-1} (Hu et al. 1996; Peterson et al. 1998). Binding of substrates in CYP19A1 causes no change in the frequency of the propionate bending modes implying that none of the substrates significantly affect the hydrogen bonding to the propionate groups. The two modes at 369 cm^{-1} and 376 cm^{-1} may be assigned to the non-H-bonded and H-bonded fractions of the substrate bound enzyme.

Fe-S stretches for AD and 19-oxo-AD bound CYP19A1

Electron donation from the axial thiolate is an important parameter in determining the stability of Compound I (Dawson 1988). Tosha et al. observed differences in the Fe-S stretch frequencies for AD, 19-OH AD and 19-oxo-AD-bound ferric CYP19A1 suggesting that substrate binding in CYP19A1 effects both the heme-distal and proximal sites (Tosha et al. 2006). Their observations suggested that in CYP19A1 substrates could modulate the electronic property of the axial thiolate and that owing to the poor electron donation from the axial thiolate in the presence of 19-oxo-AD the ferric

peroxo species would be stabilized. This line of reasoning favors the 'Compound 0' mechanism for lyase step of CYP19A1.

We too measured the Fe-S stretch frequency for AD-bound and 19-oxo-AD-bound ferric CYP19A1 but found no difference in the ν(Fe-S) for these two substrates (Figure 35) thus refuting the above stated hypothesis of reduced electron donation from the axial-thiolate in 19-oxo-AD bound CYP19A1 being responsible for an enhanced stability of the peroxo anion that then may be able to conduct the C-C scission owing to its nucleophilic character.

More informative and valuable than structural characterization of the ferric states of CYP19A1 is the vibrational spectra of the dioxygen adducts of CYP19A1 bound with different substrates, especially in the light of differential H-bonding arrangements with the bound O-O fragment. H-bonding interactions to the O-O moiety of the peroxo anion may give us a clue about the enzyme's preference for the peroxo-anion or Cpd 1 for the lyase step, as recently shown in CYP17A1 (M. Gregory et al. 2013).

AD- and 19-oxo-AD bound oxy-ferrous complexes of CYP19A1

O-O stretch frequencies and their behavior upon isotopic substitution provide valuable information about the active site structure of the oxy-ferrous (Fe-O-O) complex and its propensity to transform into the peroxo anion or the hydroperoxo anion upon ensuing reduction. Here the rR spectra is used to characterize the active site structure of oxy-ferrous complexes of CYP19A1 bound to AD and 19-oxo-AD to see if differences in organization of the active site can shed light on the differences in the choice of reactive intermediate mediating hydroxylation and C-C scission by CYP19A1.

This feasibility of this approach was recently demonstrated in CYP17A1 wherein the dioxygen adducts of CYP17A1 in the presence of 17-OH-progesterone (17-OH-Prog) or 17-OH-pregnenolone (17-OH-Preg) were studied using rR (M. Gregory et al. 2013). 17-OH-Prog and 17-OH-Preg undergo hydroxylation and C-C scission respectively. There is a growing body of evidence suggesting that the conversion of 17-OH-Preg to dihydroepiandrosterone (DHEA) goes via a peroxo-intermediate (Akhtar et al. 2011; Akhtar et al. 1994; Lee-Robichaud et al. 1998). Gregory et al. showed that rR spectra of the oxy-ferrous complexes of CYP17A1 in 17-OH-Prog and 17-OH-Preg bound states showed differences in H-bonding to the Fe-O-O moiety. DFT calculations in histidine-ligated oxy complexes predict that H-bonding to the proximal oxygen atom weakens the O-O and Fe-O bonds whereas that to the terminal oxygen atom weakens the O-O bond but strengthens the Fe-O bond

(Spiro et al. 2013). In other words, H-bonding to the terminal oxygen of Fe-O-O promotes O-O cleavage resulting in the formation of Cpd1 whereas, that to the proximal oxygen atom prolongs the lifetime of the peroxo anion which may then act as the catalytic intermediate via its nucleophilic character. Such differential H-bonding interactions and the resulting difference in the choice of reactive intermediate employed by the enzyme for catalysis has been seen previously in nitric oxide synthase (Li et al. 2007). rR characterization of CYP17A1 showed H-bonding to terminal oxygen atom in the case of 17-OH-Prog and that to the proximal O-atom in the case of 17-OH-Preg also pointing towards the peroxo-anion mediated mechanism for C-C lyase in CYP17A1.

Figure 36 shows the high-frequency rR spectra of AD-bound oxyCYP19 with the ν(O-O) band present at 1130 cm^{-1} and exhibiting an expected 64 cm^{-1} downshift upon $^{16}O_2/^{18}O_2$ substitution. A 2 cm^{-1} upshift, typically associated with H-bonding with amino acid or water molecules present in the heme pocket is observed upon H/D substitution. Figure 37 shows the high frequency of rR spectra of 19-oxo-AD bound oxyCYP19. The ν(O-O) band is observed at 1132 cm^{-1}. Substitution of $^{16}O_2$ to $^{18}O_2$ and $^{1}H_1$ to $^{2}H_1$ show a downshift of 64 cm^{-1} and upshift of 0.5 cm^{-1} respectively. The low frequency spectra of AD- and 19-oxo-AD bound CYP19A1 (Insets in Figure 36 and Figure 37 respectively) show a ν(Fe-O) stretch at 538 cm^{-1} and 534 cm^{-1} respectively. On the whole, the observed frequencies and isotopic shifts obtained for 19-oxo-AD-bound oxy CYP19A1 are quite similar to the data acquired for the AD-bound enzyme, with only the absolute values for the ν(Fe−O) modes differing, but even then with identical 29 cm^{-1} downshift upon $^{16}O_2/^{18}O_2$ substitution. Figure 38 summarizes the stretch frequencies and isotopic shifts observed for O-O and Fe-O for AD- and 19-oxo-AD-bound oxyCYP19A1 as described above.

The spectral pattern of ν(O-O) in the range of 1130-1140 cm^{-1} and a 1-2 cm^{-1} upshift upon H/D substitution is characteristic of a Fe-O-O weakly stabilized by H-bonding interactions from nearby amino acid residues or water molecules present in the heme pocket. The resonance Raman data acquired here suggests that neither of the substrates exhibits an unusual H-bonding arrangement to the Fe-O-O fragment as seen in CYP17A1. Both AD and 19-oxo-AD bound oxyCYP19A1 show signs of H-bonding to the distal oxygen atom which suggests the involvement of Cpd 1 in both the hydroxylation and aromatization steps of CYP19A1. Similarity in the rR signatures of oxyCYP19A1 bound to AD, substrate for the hydroxylase step and 19-oxo-AD, substrate for the lyase step of aromatase suggests that the same iron-oxygen intermediate is involved in carrying out both these distinct chemical modifications. It is widely accepted that hydroxylation in P450s, including CYP19A1 happens via H-rebound mechanism mediated by the archetypical Cpd 1 (Groves 1985). Therefore, our data suggests that Cpd 1 is also responsible for the lyase reactivity of CYP19A1.

Difference in characteristics of the rR spectra of oxyCYP17A1 and oxyCYP19A1 upon H/D substitution when bound to corresponding substrates undergoing carbon-carbon scission suggest that the choice of iron-oxygen intermediate utilized by the P450 to carry out catalysis may partially depend on the substrate molecule itself. The substrate molecule may, by controlling the H-bonding status of the bound O-O moiety, actively decide if the peroxo-anion or Cpd 1 would be used for catalysis. This novel phenomenon, well demonstrated by comparing CYP19A1 and CYP17A1 has been coined as 'substrate-assisted catalysis' and would be subject to future research by the laboratories of Drs. Sligar and Kincaid.

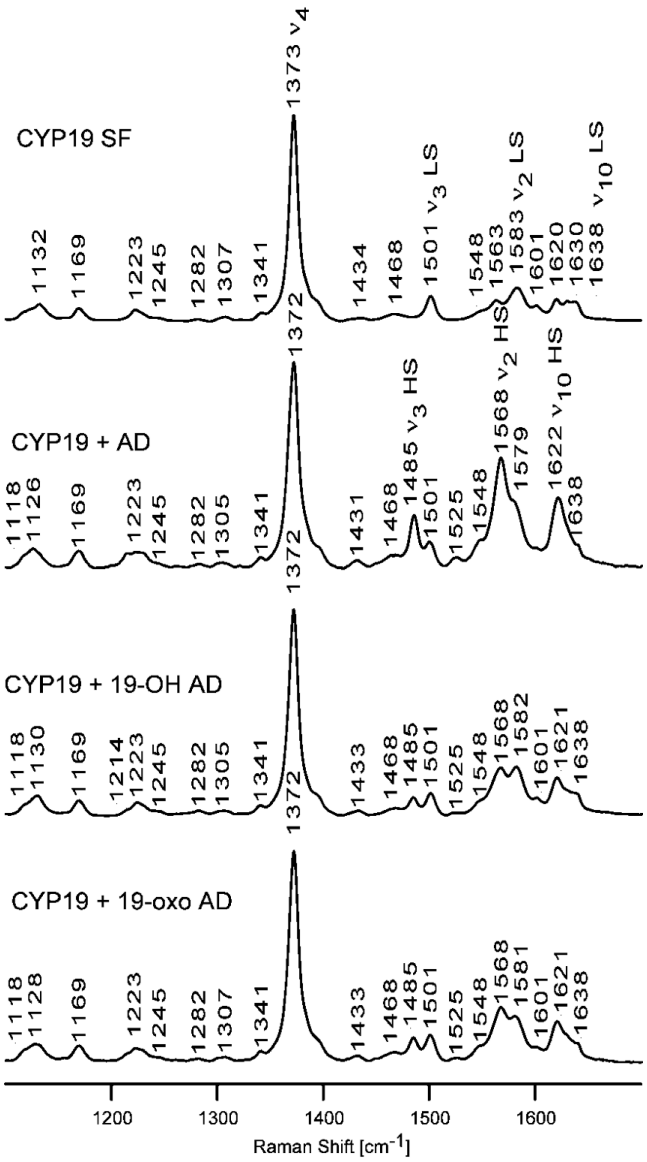

Figure 32: The high frequency RR spectra of CYP19 without substrate (SF) and with androstenedione (AD), 19-OH-androstenedione (19-OH-AD) and 19-oxo androstenedione (19-oxo-AD). Spectra are normalized to the ν4 mode. Protein concentration is 120 μM and the substrates is 700 μM.

CYP19A1	% High-spin	% Low-spin
Substrate-free	6	94
+ Androstenedione	86	14
+ 19-OH androstenedione	53	47
+ 19-oxo androstenedione	60	40

Table 1: Percentage high- and low-spin in CYP19A1 in substrate-free and substrate-bound forms based on resonance Raman (Mak et al. 2013).

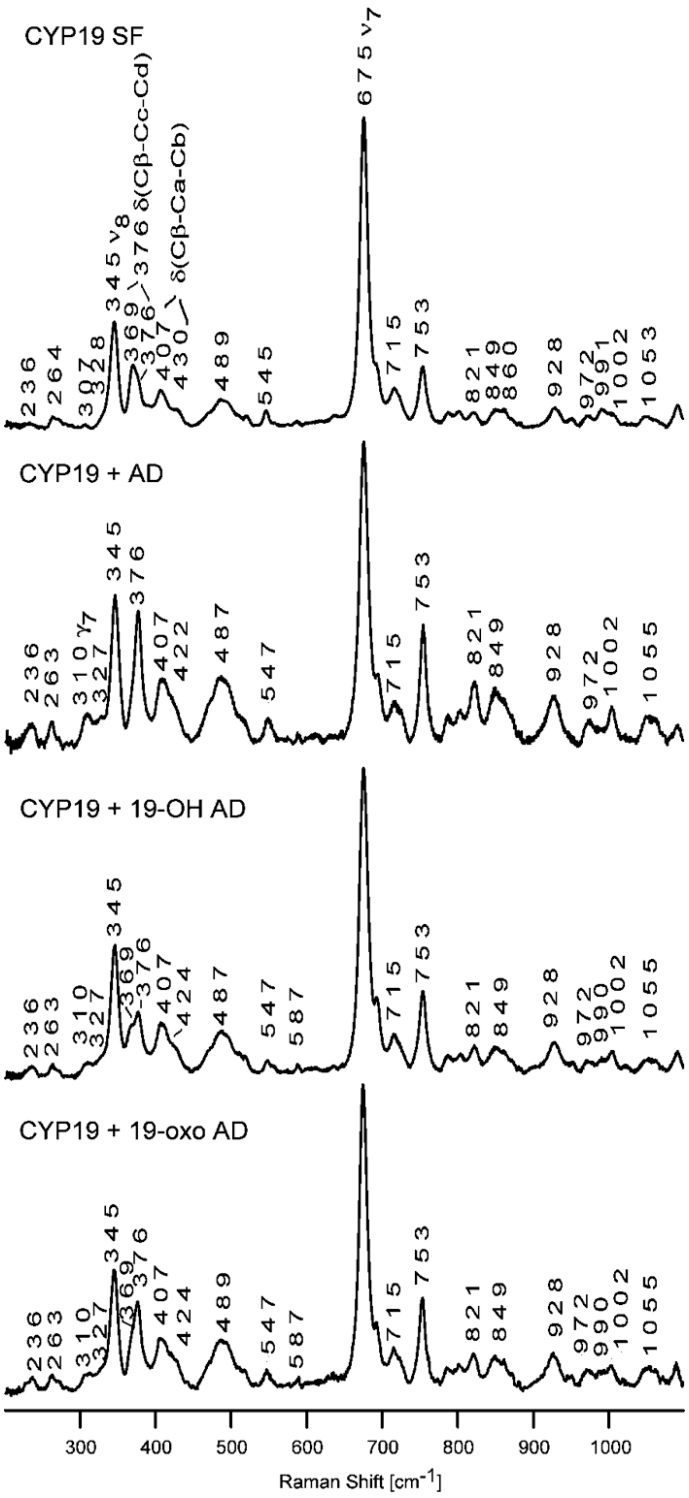

Figure 33: The low frequency RR spectra of CYP19 without substrate (SF), with an androstenedione (AD) 19-OH-androstenedione (19-OH AD) and 19-oxo androstenedione (19-oxo AD). Spectra are normalized to the ν7 mode.

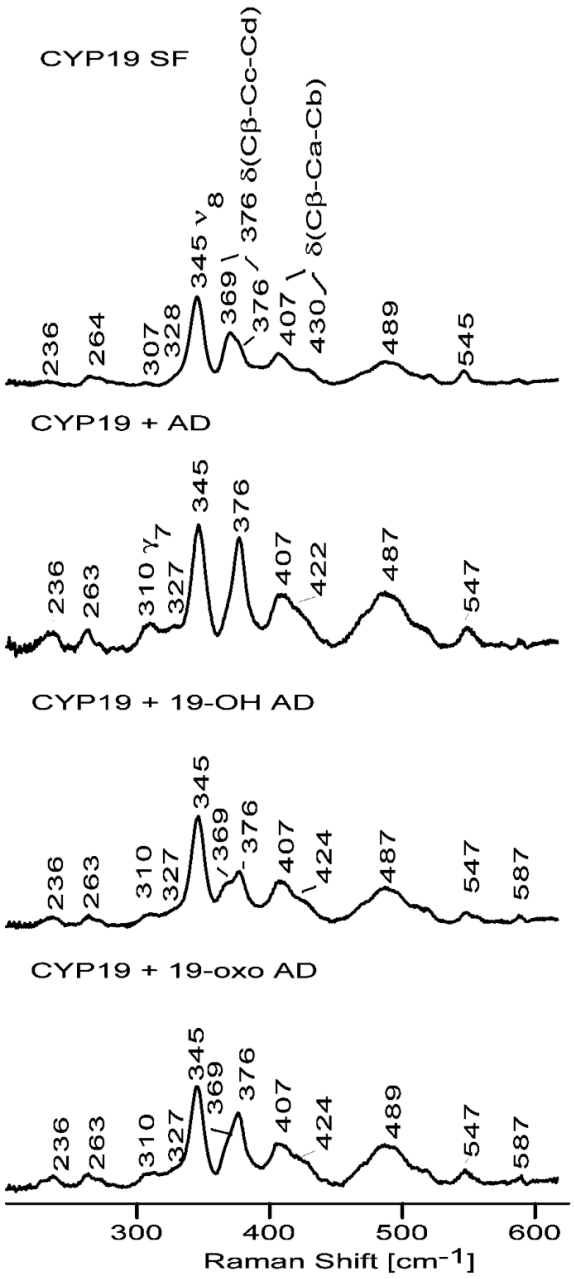

Figure 34: As in Figure 33 but expanded for better view

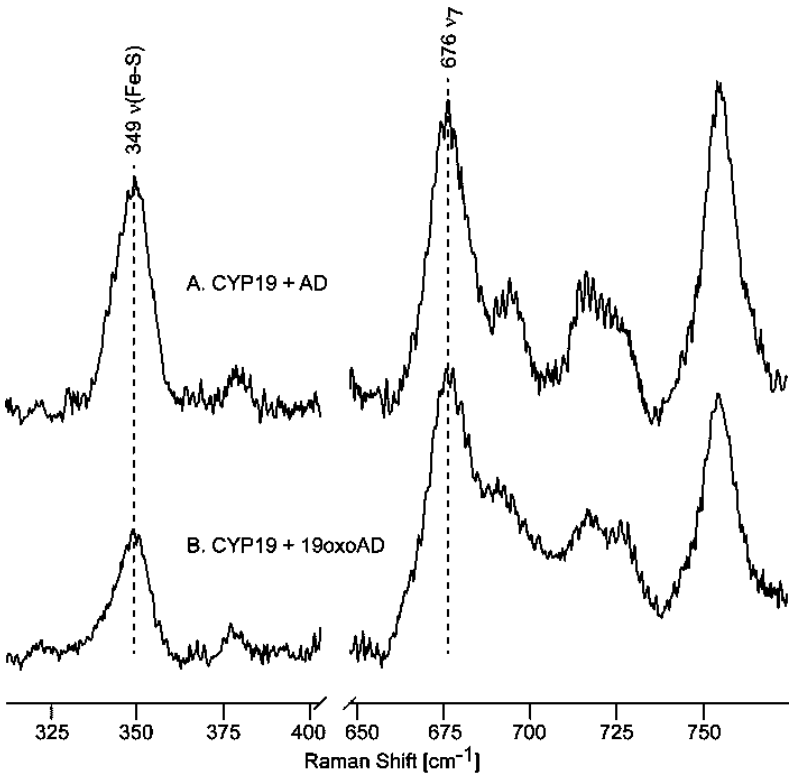

Figure 35: The low frequency spectra of ferric ND:CYP19 with AD (A) and 19-oxo-AD (B) substrates. Excitation line was 356.7 nm, the spectra were normalized to the ν7 mode at 676 cm-1. The lower intensity of the ν(Fe-S) mode in the spectrum of 19-oxo-AD reflects the lower high spin state population in this sample, as compared to the AD-bound sample.

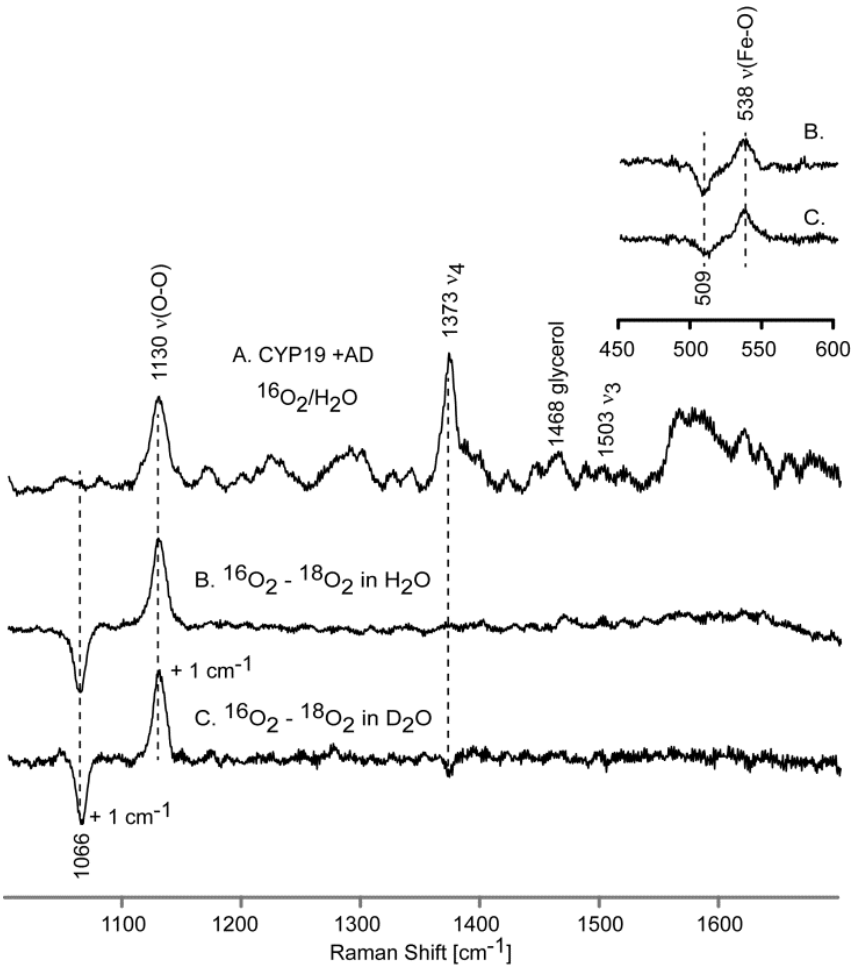

Figure 36: The high frequency region of AD-bound oxy complexes of ND:CYP19 and their difference traces. Inset Difference traces in the low-frequency region.

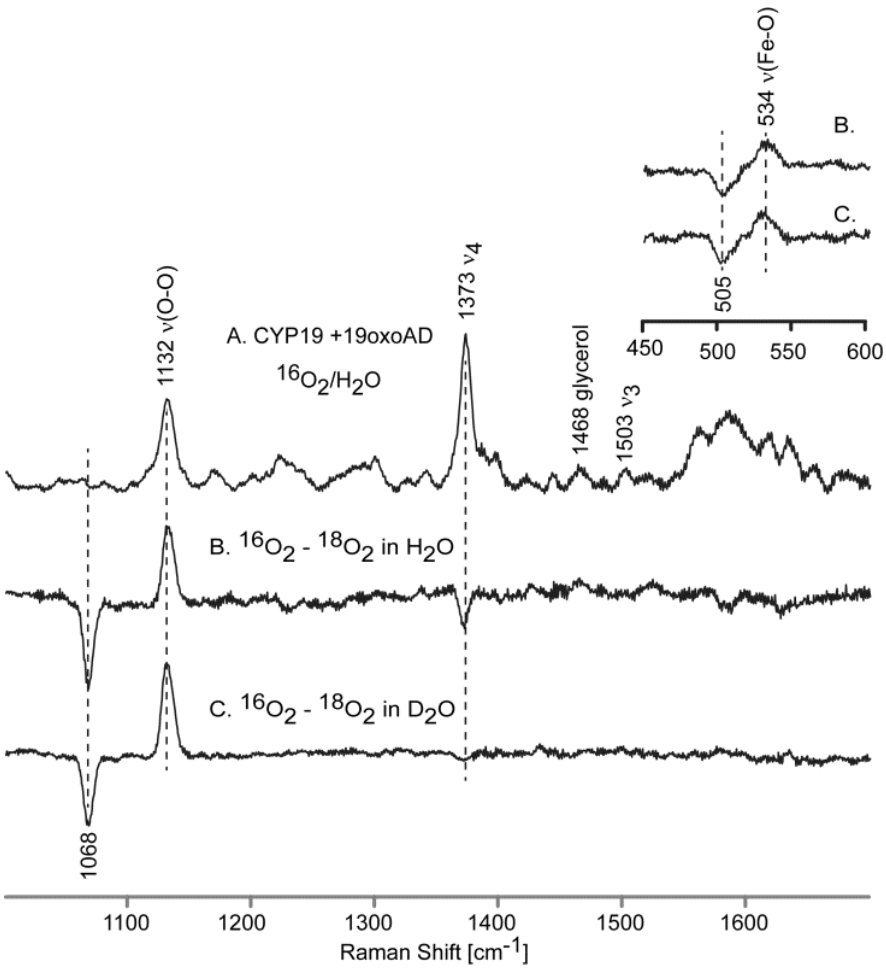

Figure 37: The high frequency spectral region of 19-oxo-AD-bound oxy complexes of ND:CYP19 and the difference traces. Inset Difference traces in the low-frequency region.

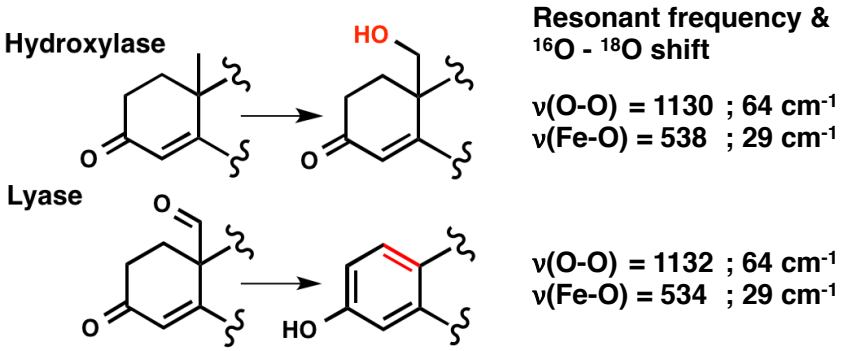

Figure 38: ν(O-O) and ν(Fe-O) stretch frequencies and isotopic shifts for AD- and 19-oxo-AD-bound oxyCYP19A1 complexes.

Chapter 6: Kinetic Solvent Isotope Effect in Steady State Kinetics of NADPH Consumption and Product Formation by CYP19A1

INTRODUCTION

The effect of deuterium substitution on turnover rates can be used as indicator to ascertain the involvement of protons in O-O heterolysis in P450s. This was first shown by Vidakovic et al. in wild-type and D251N mutant of CYP101 (Vidakovic et al. 1998), and recently by (M. C. Gregory et al. 2013) in human CYP17A1. (M. C. Gregory et al. 2013) used kinetic solvent isotope effect (KSIE) to draw a distinction between the reaction mechanisms for hydroxylase and lyase chemistries of human CYP17A1. CYP17A1 is a membrane-bound steroidogenic P450. It acts upstream to CYP19A1 in the human steroidogenesis pathway and is responsible for the biosynthesis of pregnenolone, progesterone, 17-α-hydroxy pregnenolone, 17-α-hydroxy progesterone, dihydroepiandrosterone and androstenedione. Just like CYP19A1, it is unclear whether Compound 0 or Compound 1 is responsible for the lyase chemistry of CYP17A1.

Two distinct protonation events facilitate O-O heterolysis to generate Compound 1 from the peroxoanion intermediate in P450s. The two proposed hypothesis, namely 'Compound 0' and 'Compound 1' mechanisms for C-C scission in CYP19A1 differ in the identity of reaction intermediate that orchestrates catalysis and therefore, differ in the involvement of protons. Kinetic solvent isotope effect is a great way to distinguish between 'Compound 0' and 'Compound 1' mechanisms. The hydroxylase and lyase chemistries of CYP17A1 exhibit KSIEs of 1.3 and 0.39 respectively. This suggests the involvement of iron-bound ferric peroxoanion for C17-C20 scission instead of the archetypical Compound 1 (M. C. Gregory et al. 2013). The same approach was applied to CYP19A1 and the results are discussed below.

MATERIALS AND METHODS

CYP19A1 expression, purification and Nanodisc incorporation

The expression, purification and incorporation of CYP19A1 into POPC Nanodiscs was performed as previously described on sections pages 7 and 10.

CPR expression and purification

Cytochrome P450 reductase from rat was expressed in the pOR262 vector and purified as described previously in (Vermilion & Coon 1978). The rat CPR/pOR262 plasmid was obtained as a gift from Dr. Todd D. Porter (University of Kentucky, Lexington, KY).

Formation of CPR–CYP19A1 complex

Incorporation of CPR into preformed and purified human CYP19A1 Nanodiscs was made by direct addition of oligomeric CPR at a molar ratio of 1:4 CYP19A1 (200 pmol) to CPR (800 pmol), as described previously (Grinkova et al. 2010). Briefly, 1 ml of CYP19A1 and CPR solution in 100 mM potassium phosphate buffer, pH 7.4, containing 50 mM NaCl and 50 μM substrate (AD, 19-OH-AD, or 19-oxo-AD) was brought to 37 °C in a stirred quartz cuvette with a path length of 0.4 cm. The sample was incubated for 3 minutes to facilitate formation of functional CYP19A1–CPR complex. A ratio of 1:4 of P450:CPR was chosen based on previously established optimal ratio of reductase to P450 for *in vitro* turnover experiments using the Nanodisc system (Grinkova et al. 2010). In this approach the reductase, in a dynamic equilibrium with reductase molecules in solution, inserts into the P450 containing Nanodisc through its membrane anchoring tail thereby allowing the formation of an efficient electron transfer complex.

NADPH consumption

300 μM of NADPH was added to the reaction mixture to initiate turnover. The consumption of NADPH was monitored by recording the decrease in absorbance at 340 nm for 10 min. The reaction was then stopped by adding 50 μl of 9 M sulfuric acid to reduce the pH of the reaction below 4.0. The sample was removed from the cuvette, flash frozen in liquid nitrogen, and stored at -80 °C until further analysis. All optical measurements were performed on Hitachi U-3300 spectrophotometer supplied with temperature controller and a built-in magnetic stirrer. The rate of NADPH oxidation was determined from the slope of absorption at 340 nm during the first three minutes using an extinction coefficient of 6.22 $cm^{-1}mM^{-1}$.

Product formation

The conversion of AD, 19-OH and 19-oxo-AD to estrone was analyzed by HPLC (Waters). Briefly, 1 μl of 18 mM progesterone solution in methanol (for use as an internal standard) was added to 1 ml each of the reaction sample and vortexed for 30 seconds. 2 ml of chloroform was added to each aliquot and vortexed for 30 seconds. The organic phase was removed and dried under the

continuous stream of nitrogen. The dried sample was then dissolved in 100 µl of methanol. 30 µl of this solution was injected onto a 150 x 2.1 mm, 3 µm C18-HPLC column (ACE-111-1502). 45% each of methanol and acetonitrile in water was used as the mobile phase at a flow rate of 0.2 ml/min. The 19-hydroxylated and 19-oxo product of AD were separated on the linear gradient of methanol and acetonitrile from 20% to 80% in 30 min, and detected at 240 nm. The formation of estrogen was detected at 280 nm. Peak integration was performed with GRAM/32 software (Thermo Fischer Scientific).

In order to determine the reaction time for the substrates AD, 19-OH-AD and 19-oxo-AD, time-depended substrate conversion was performed first and the 10 min incubation time chosen for the catalytic activity, during which the catalytic activity was still in linear phase (Figure 39).

All measurements were made in deuterated buffers of same ionic strength and pD 7.0. Deuterated samples were prepared by exhaustive exchange of the proteins in D_2O.

RESULTS AND DISCUSSION

Product formation rates and effect of H/D substitution

Upon evaluating the rates of product formation for the three steps of CYP19 catalysis in protiated and deuterated buffers the following observations were made (Figure 40):

- Using AD as a substrate, two products were obtained, 19-OH-AD and 19-oxo-AD. The individual rates of formation of these two products was 1.63 ± 0.04 min^{-1} and 4.06 ± 0.30 min^{-1} , respectively, (total rate of 5.70 ± 0.34 min^{-1}) in H_2O. The same rates slowed to 0.62 ± 0.07 min^{-1} and 1.52 ± 0.15 min^{-1}, respectively (a total of 2.14 ± 0.22 min^{-1}) when H_2O was substituted for D_2O. This corresponds to a KSIE (k_H/k_D) of 2.7 for the first step of CYP19 catalysis.
- Using 19-OH-AD as the starting substrate, two products were obtained again, 19-oxo-AD and estrone. The rates of product formation of these two products were 2.3 ± 0.2 min^{-1} and 1.8 ± 0.3 min^{-1} in H_2O and 2.39 ± 0.2 min^{-1} and 0.91 ± 0.3 min^{-1} in D_2O. The total rates of 19-OH-AD turnover by CYP19 of 4.1 ± 0.5 min^{-1} and 3.3 ± 0.23 min^{-1} in H_2O and D_2O respectively correspond to a KSIE of 1.2.
- When 19-oxo-AD is used as a substrate estrone was obtained as the sole product. The rate of estrone formation in H_2O and D_2O was calculated to be 7.1 ± 0.8 min^{-1} and 2.8 ± 0.8 min^{-1} respectively. This corresponds to a KSIE of 2.53.

The value of KSIE for steps I and II are consistent with those reported for other P450 systems catalyzing hydroxylation chemistry via a Cpd1 mediated hydrogen abstraction and radical recombination (Vidakovic et al. 1998; Batabyal et al. 2013; Liu & Ortiz de Montellano 2000). A KSIE of 2.53 for step III suggests the involvement of same intermediate, Compound 1 in the lyase step of CYP19A1.

The conversion of 19-hydroxy androstenedione gives a KSIE of 1.2 in contrast to 2.7 and 2.53 for androstenedione and 19-oxo-androstenedione turnover. This is an interesting observation and is discussed below:

Catalysis by CYP19A1 is distributive as evidenced by formation of 19-OH AD and 19-oxo AD from AD and 19-oxo AD and estrone from 19-OH AD. Using AD as the starting substrate we observe formation of 19-OH AD and 19-oxo AD under steady state conditions. Rates of formation of both these products show slowing down upon H_2O to D_2O substitution. Both, rates of formation of individual products and total product, display an isotope effect of ≥ 2.6. Using 19-OH AD as the starting substrate we observe 19-oxo AD and estrone under steady state turnover conditions. This case is a little peculiar though. Formation of estrone shows a KSIE of 2 (1.8 min^{-1} in H_2O versus 0.91 min^{-1} in D_2O), however, the formation of 19-oxo AD shows no solvent isotope effect bringing down the net KSIE of product formation down to 1.2 (Table 2). Conversion of 19-OH AD to 19-oxo AD goes through a hydroxylation at the C19 to produce a gem-diol that then undergoes dehydration to yield the 19-oxo AD intermediate (Figure 41). It is plausible that the rate of dehydration of the gem-diol intermediate is partially rate limiting. This would explain the diminished magnitude of observed KSIE for step II as compared to steps I and III.

Rates of NADPH consumption and the effect of deuterium substitution on them

The overall rate of NADPH oxidation in the presence of different substrates was also studied. In protiated solvent system, NADPH consumption rates in the presence of AD, 19-OH AD and 19-oxo AD were found to be 37 ± 4.5 min^{-1}, 37 ± 4 min^{-1} and 35 ± 1 min^{-1}. Upon H/D substitution, they decreased to 14 ± 1.5 min^{-1}, 8.00 ± 1.3 min^{-1} and 6 ± 1.2 min^{-1} respectively. A corresponding increase in the coupling efficiency from 15, 11 and 20% to 16, 41 and 47% respectively was also observed (Figure 42). A higher level of coupling in deuterated solvents is due to slowing of the proton dependent uncoupling pathways, predominantly the peroxide and oxidase shunt pathways. The higher coupling efficiency observed in the presence of 19-OH-AD and 19-oxo-AD may be attributed to the polar nature of these substrates thereby making possible presence of additional water molecules and/or enhanced stabilization of the existing hydrogen-bonding network at the

active site of the enzyme. Slowing down of the NADPH oxidation rates upon solvent substitution when AD, 19-OH-AD or 19-oxo-AD are used as starting substrates indicates that in all three steps protonation is rate limiting.

Taken together, the NADPH oxidation and product formation rates suggest that the same intermediate, Cpd 1 is responsible for both the hydroxylation and lyase chemistries of CYP19A1.

CONCLUSION

We observe a normal slowing of Steps 1 and 2 of CYP19A1 catalysis (k_H/k_D of 2.7 and 1.2) consistent with the need for two protonation steps in concomitant formation of the hydroperoxo-ferric complex and Cpd 1 in D_2O. These observations are also consistent with the previous reports of solvent isotope effects in P450cam and other P450s (Raag et al. 1991; Batabyal et al. 2013; Groves 2006; Shimada et al. 1997). The presence of kinetic solvent isotope effect of a similar magnitude when 19-oxo-AD, the substrate for lyase step of CYP19A1 is present, suggests the involvement of the same intermediate *viz*. Cpd 1 for the aromatization step of CYP19A1 as well. In addition, CYP19A1 also showed the highest coupling for the lyase substrate, 19-oxo-AD, compared with the hydroxylase substrates, AD and 19-OH-AD, in both protiated and deuterated solvent system.

Taken together, our results suggest that the involvement of the same high-valent iron-oxo species, Cpd 1, as the reactive intermediate during the conversion of AD, 19-OH-AD and 19-oxo-AD. This is based on the significant KSIE observed during the first two steps of hydroxylation as well as the last step of lyase reaction. Our conclusions are also are in line with the suggestion, albeit indirect, of Cpd1 mediated C-C scission by CYP19A1 provided by the rR, characterization of the oxy-complexes of AD- and 19-oxo-AD bound CYP19A1 in Nanodiscs. This suggestion of involvement of Cpd 1 during C10-C19 lyase reaction by CYP19A1 is in contrast to recent observation of an *inverse* KSIE in human CYP17A1 involved in androgen formation where the reactive peroxoanion intermediate is involved in the catalytic step (M. C. Gregory et al. 2013).

In conclusion, our results highlight the involvement of Cpd 1 during the first two steps of aromatization by CYP19A1, a general mechanism known to be involved in other P450s. We also implicate the involvement of Cpd 1 as a reactive intermediate during the controversial C10-C19 lyase reaction by human aromatase.

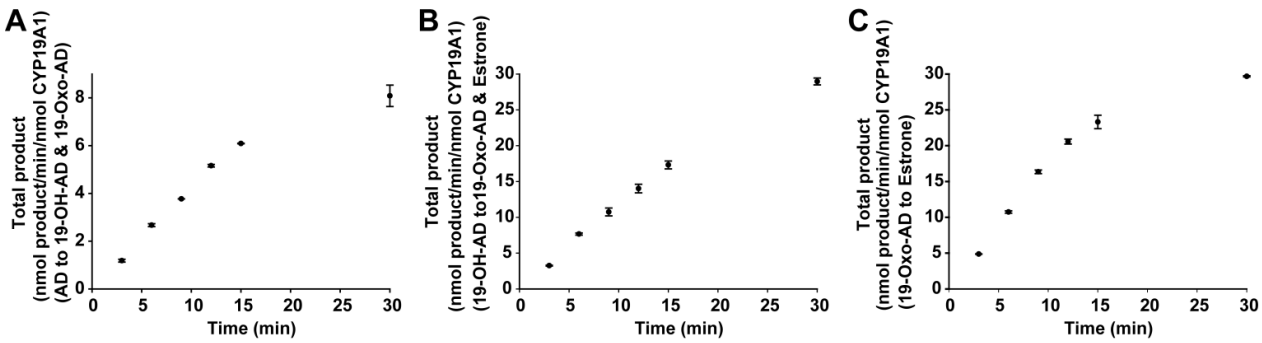

Figure 39: Time dependent total conversion of AD (A), 19-OH-AD (B) and 19-oxo-AD (C) by CYP19A1.

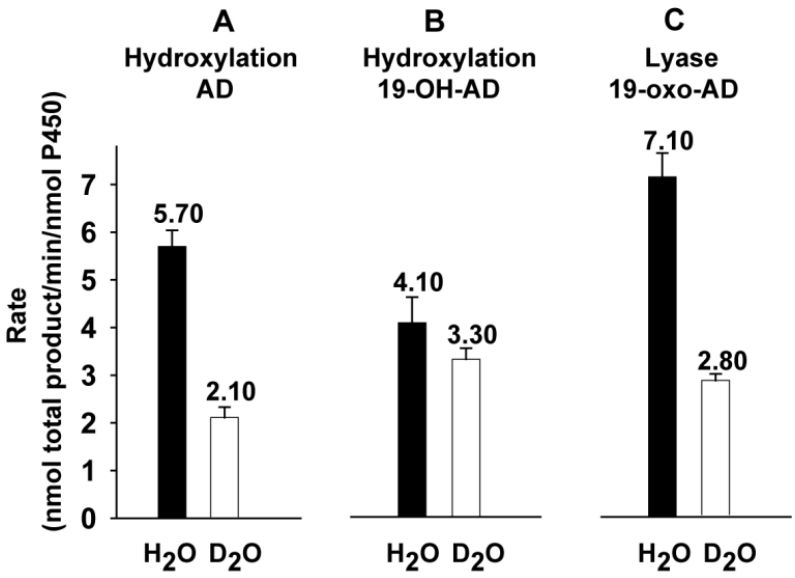

Figure 40: Total product formation rate for AD (A), 19-hydroxy-AD (B) and 19-oxo-AD (C) catalysis by CYP19A1 in protiated (black bars) and deuterated (open bars) solvent systems. Error bars represent standard deviation of 3-5 independent measurements.

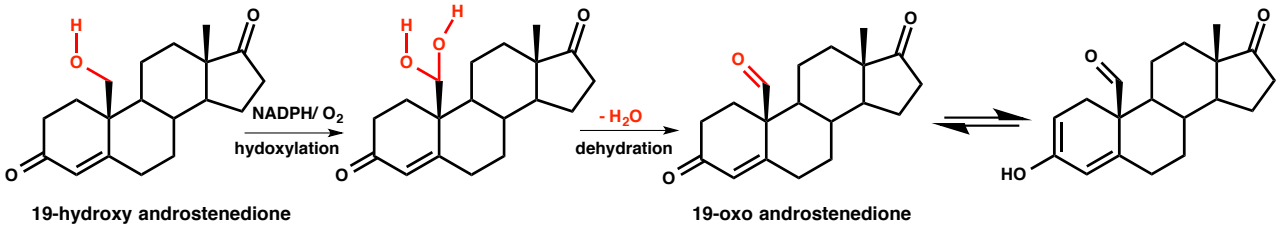

Figure 41: Conversion of 19-hydroxy-androstenedione to 19-oxo-androstendeione by CYP19A1 via an intermediate gem-diol dehydration step.

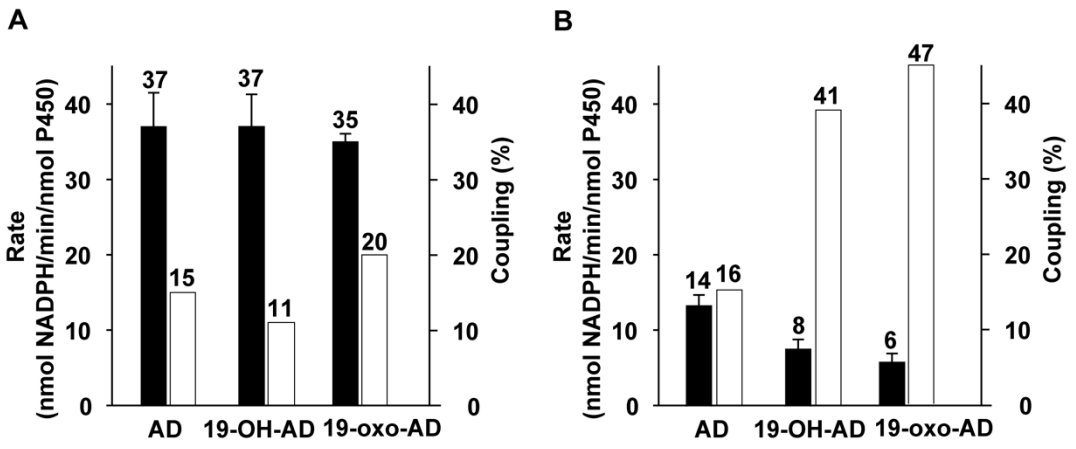

Figure 42: NADPH oxidation rates (solid bars) and corresponding coupling efficiencies (open bars) for steps I, II and III of CYP19A1 catalysis in H_2O (A) and D_2O (B).

Substrate / Product	19-OH AD (min $^{-1}$)	19-oxo-AD (min $^{-1}$)	Estrone (min $^{-1}$)	Product 2/ Product 1	**KSIE w.r.t Product 1**	**KSIE w.r.t Product 2**	Total Product (min $^{-1}$)	**Overall KSIE**
AD	1.63	4.06		2.49	2.6	2.7	5.69	2.7
	0.62	1.52		2.45			2.14	
19-OH AD		2.30	1.80	0.78	1.0	2.0	4.10	1.2
		2.39	0.91	0.38			3.30	
19-oxo-AD			7.10	-	2.5		7.10	2.5
			2.80	-			2.80	

H_2O/ D_2O

Table 2: Individual and net product formation rates starting with different androgenic substrates of CYP19A1 and corresponding kinetic solvent isotope effects upon H/D substitution.

References

Akhtar, M. et al., 1994. Mechanism of the Acyl-Carbon Cleavage and Related Reactions Catalyzed by Multifunctional P-450s: Studies on Cytochrome P-45017.alpha. *Biochemistry*, 33(14), pp.4410–4418.

Akhtar, M., Wright, J.N. & Lee-Robichaud, P., 2011. A review of mechanistic studies on aromatase (CYP19) and 17α-hydroxylase-17,20-lyase (CYP17). *The Journal of Steroid Biochemistry and Molecular Biology*, 125(1-2), pp.2–12.

Andrade, E.N.C., 1934. A theory of the viscosity of liquids .— Part I. *Philosophical Magazine Series 7*, 17(112), pp.497–511.

Ansari, A. et al., 1987. Rebinding and relaxation in the myoglobin pocket. *Biophysical Chemistry*, 26(2-3), pp.337–55.

Austin, R.H. et al., 1975. Dynamics of ligand binding to myoglobin. *Biochemistry*, 14(24), pp.5355–73.

Avramov, I., 2005. Viscosity in disordered media. *Journal of Non-Crystalline Solids*, 351(40-42), pp.3163–3173.

Batabyal, D., Li, H. & Poulos, T.L., 2013. Synergistic effects of mutations in cytochrome P450cam designed to mimic CYP101D1. *Biochemistry*, 52(32), pp.5396–402.

Bayburt, T.H., Grinkova, Y. V. & Sligar, S.G., 2002. Self-Assembly of Discoidal Phospholipid Bilayer Nanoparticles with Membrane Scaffold Proteins. *Nano Letters*, 2(8), pp.853–856.

Bayburt, T.H. & Sligar, S.G., 2010. Membrane protein assembly into Nanodiscs. *FEBS letters*, 584(9), pp.1721–7.

Bayburt, T.H. & Sligar, S.G., 2003. Self-assembly of single integral membrane proteins into soluble nanoscale phospholipid bilayers. *Protein science : a publication of the Protein Society*, 12(11), pp.2476–81.

Beece, D. et al., 1980. Solvent viscosity and protein dynamics. *Biochemistry*, 19(23), pp.5147–5157.

Beece, D. et al., 1981. The effect of viscosty on the photocycle of Bacteriorhodopsin. *Photochemistry and Photobiology*, 33(4), pp.517–522.

Berendzen, J. & Braunstein, D., 1990. Temperature-derivative spectroscopy: A tool for protein dynamics. *Proceedings of the National Academy of Sciences*, 87(1), p.1.

Boldog, T. et al., 2006. Nanodiscs separate chemoreceptor oligomeric states and reveal their signaling properties. *Proceedings of the National Academy of Sciences of the United States of America*, 103(31), pp.11509–14.

Borch, J. et al., 2008. Nanodiscs for immobilization of lipid bilayers and membrane receptors: kinetic analysis of cholera toxin binding to a glycolipid receptor. *Analytical chemistry*, 80(16), pp.6245–52.

Bulun, S.E. et al., 2004. Organization of the human aromatase p450 (CYP19) gene. *Seminars in reproductive medicine*, 22(1), pp.5–9.

Champion, P.M., Gunsalus, I.C. & Wagner, G.C., 1978. Resonance Raman investigations of cytochrome P450cam from Pseudomonas putida. *Journal of the American Chemical Society*, 100, pp.3743–3751.

Chen, Y.-M. & Pearlstein, A.J., 1987. Viscosity-Temperature Correlation for Glycerol-Water Solutions. *Industrial and Engineering Chemistry Research*, 26, pp.1670–1672.

Cheng, N., 2008. Formula for the Viscosity of a Glycerol-Water Mixture. *Industrial and Engineering Chemistry Research*, 47, pp.3285–3288.

Clark, J.P. et al., 2006. The role of Thr268 and Phe393 in cytochrome P450 BM3. *Journal of inorganic biochemistry*, 100(5-6), pp.1075–90.

Cuzick, J. et al., 2003. Overview of the main outcomes in breast-cancer prevention trials. *Lancet*, 361(9354), pp.296–300.

Davydov, R. et al., 1991. EPR-spectroscopy of reduced oxyferrous-P450cam. *FEBS Letters*, 295(1-3), pp.113–115.

Davydov, R. et al., 2001. Hydroxylation of Camphor by Reduced Oxy-Cytochrome P450cam: Mechanistic Implications of EPR and ENDOR Studies of Catalytic Intermediates in Native and Mutant Enzymes. *Journal of the American Chemical Society*, 123(7), pp.1403–1415.

Davydov, R.M., 1980. *Optical and ESR spectroscopy studies of electronic adducts of oxymyoglobin and oxyhemoglobin*,

Dawson, J.H., 1988. Probing structure-function relations in heme-containing oxygenases and peroxidases. *Science*, 240(4851), pp.433–439.

Denisov, I.G. et al., 2001. Characterization of the oxygenated intermediate of the thermophilic cytochrome P450 CYP119. *Journal of Inorganic Biochemistry*, 87(4), pp.215–26.

Denisov, I.G. et al., 2008. Resonance Raman characterization of the peroxo and hydroperoxo intermediates in cytochrome P450. *The Journal of Physical Chemistry A*, 112(50), pp.13172–9.

Denisov, I.G. et al., 2006. The ferrous-dioxygen intermediate in human cytochrome P450 3A4. Substrate dependence of formation and decay kinetics. *The Journal of Biological Chemistry*, 281(33), pp.23313–8.

Denisov, I.G., Makris, T.M. & Sligar, S.G., 2002. Cryoradiolysis for the study of P450 reaction intermediates. *Methods in enzymology*, 357, pp.103–115.

Denisov, I.G. & Sligar, S.G., 2011. Cytochromes P450 in nanodiscs. *Biochimica et biophysica acta*, 1814(1), pp.223–9.

Derouet-Hümbert, E., Roemer, K. & Bureik, M., 2005. Adrenodoxin (Adx) and CYP11A1 (P450scc) induce apoptosis by the generation of reactive oxygen species in mitochondria. *Biological chemistry*, 386(5), pp.453–61.

Van Doorslaer, S. & Vinck, E., 2007. The strength of EPR and ENDOR techniques in revealing structure-function relationships in metalloproteins. *Physical Chemistry Chemical Physics : PCCP*, 9(33), pp.4620–38.

Ehrenstein, D. & Nienhaus, G.U., 1992. Conformational substates in azurin. *Proceedings of the National Academy of Sciences of the United States of America*, 89(20), pp.9681–5.

Eisenmesser, E.Z. et al., 2005. Intrinsic dynamics of an enzyme underlies catalysis. *Nature*, 438(7064), pp.117–21.

Fisher, B. et al., 2001. Five Versus More Than Five Years of Tamoxifen for Lymph Node-Negative Breast Cancer: Updated Findings From the National Surgical Adjuvant Breast and Bowel Project B-14 Randomized Trial. *JNCI Journal of the National Cancer Institute*, 93(9), pp.684–690.

Frauenfelder, H. et al., 2009. A unified model of protein dynamics. *Proceedings of the National Academy of Sciences of the United States of America*, 106(13), pp.5129–34.

Frauenfelder, H., Parak, F. & Young, R.D., 1988. Conformational substates in proteins. *Annual review of biophysics and biophysical chemistry*, 17, pp.451–79.

Frauenfelder, H., Petsko, G.A. & Tsernoglou, D., 1979. Temperature-dependent X-ray diffraction as a probe of protein structural dynamics. *Nature*, 280(5723), pp.558–563.

Frauenfelder, H., Sligar, S.G. & Wolynes, P.G., 1991. The Energy Landscapes and Motions of Proteins. *Science*, 254, pp.1598–1603.

Gantt, S.L. et al., 2009. The critical iron-oxygen intermediate in human aromatase. *Biochemical and Biophysical Research communications*, 387(1), pp.169–73.

Gavish, B., 1978. The role of geometry and elastic strains in dynamic states of proteins. *Biophysics of Structure and Mechanism*, 4(1), pp.37–52.

Gavish, B. & Werber, M.M., 1979. Viscosity-dependent structural fluctuations in enzyme catalysis. *Biochemistry*, 18(7), pp.1269–75.

Gekko, K. & Timasheff, S.N., 1981. Mechanism of protein stabilization by glycerol: preferential hydration in glycerol-water mixtures. *Biochemistry*, 20(16), pp.4667–4676.

Ghosh, D. et al., 2009. Structural basis for androgen specificity and oestrogen synthesis in human aromatase. *Nature*, 457(7226), pp.219–23.

Glück, J.M. et al., 2009. Integral membrane proteins in nanodiscs can be studied by solution NMR spectroscopy. *Journal of the American Chemical Society*, 131(34), pp.12060–1.

Glück, J.M., Koenig, B.W. & Willbold, D., 2011. Nanodiscs allow the use of integral membrane proteins as analytes in surface plasmon resonance studies. *Analytical biochemistry*, 408(1), pp.46–52.

Gonzalez, J.A.T., Longinotti, M.P. & Corti, H.R., 2011. The Viscosity of Glycerol-Water Mixtures Including the Supercooled Region. *Journal of Chemical & Engineering Data*, 56, pp.1397–1406.

Graham-Lorence, S. et al., 1995. A three-dimensional model of aromatase cytochrome P450. *Protein Science*, 4(6), pp.1065–1080.

Gregory, M. et al., 2013. Differential hydrogen bonding in human CYP17 dictates hydroxylation versus lyase chemistry. *Angewandte Chemie (International ed. in English)*, 52(20), pp.5342–5.

Gregory, M.C. et al., 2013. Kinetic solvent isotope effect in human P450 CYP17A1-mediated androgen formation: evidence for a reactive peroxoanion intermediate. *Journal of the American Chemical Society*, 135(44), pp.16245–7.

Grinkova, Y. V et al., 2008. The ferrous-oxy complex of human aromatase. *Biochemical and biophysical research communications*, 372(2), pp.379–82.

Grinkova, Y. V, Denisov, I.G. & Sligar, S.G., 2010. Functional reconstitution of monomeric CYP3A4 with multiple cytochrome P450 reductase molecules in Nanodiscs. *Biochemical and biophysical research communications*, 398(2), pp.194–8.

Groves, J.T., 2006. High-valent iron in chemical and biological oxidations. *Journal of inorganic biochemistry*, 100(4), pp.434–47.

Groves, J.T., 1985. Key elements of the chemistry of cytochrome P-450: The oxygen rebound mechanism. *Journal of Chemical Education*, 62(11), p.928.

Guzzi, R., Bartucci, R. & Marsh, D., 2014. Heterogeneity of protein substates visualized by spin-label EPR. *Biophysical journal*, 106(3), pp.716–22.

Hackett, J.C., Brueggemeier, R.W. & Hadad, C.M., 2005. The final catalytic step of cytochrome P450 aromatase: a density functional theory study. *Journal of the American Chemical Society*, 127(14), pp.5224–37.

Harada, N. et al., 1999. Localized Expression of Aromatase in Human Vascular Tissues. *Circulation Research*, 84(11), pp.1285–1291.

Hoffman, B.M., 1991. Electron nuclear double resonance (ENDOR) of metalloenzymes. *Accounts of Chemical Research*, 24(6), pp.164–170.

Hu, S., Smith, K.M. & Spiro, T.G., 1996. Assignment of protoheme Resonance Raman spectrum by heme labeling in myoglobin. *Journal of the American Chemical Society*, 118, pp.12638–12646.

Imai, Y. & Nakamura, M., 1989. Point mutations at threonine-301 modify substrate specificity of rabbit liver microsomal cytochromes P-450 (laurate (ω-1)-hydroxylase and testosterone 16α-hydroxylase). *Biochemical and Biophysical Research Communications*, 158(3), pp.717–722.

Jones, M.E.E. et al., 2007. Recognizing rare disorders: aromatase deficiency. *Nature clinical practice. Endocrinology & metabolism*, 3(5), pp.414–21.

Kappl, R. et al., 1985. Electron spin and electron nuclear double resonance of the [FeO2]-centre from irradiated oxyhemo- and oxymyoglobin. *Biochimica et Biophysica Acta (BBA)/Protein Structure and Molecular*, 827(3), pp.327–343.

Khatri, Y. et al., 2014. Active site proton delivery and the lyase activity of human CYP17A1. *Biochemical and biophysical research communications*, 443(1), pp.179–84.

Kijac, A.Z. et al., 2007. Magic-angle spinning solid-state NMR spectroscopy of nanodisc-embedded human CYP3A4. *Biochemistry*, 46(48), pp.13696–703.

Kispert, L.D. & Piekara-Sady, L., 2006. ENDOR Spectroscopy. In *Handbook of Applied Solid State Spectroscopy*. Springer US, pp. 151–199.

Kriegl, J.M. et al., 2002. Ligand binding and protein dynamics in neuroglobin. *Proceedings of the National Academy of Sciences of the United States of America*, 99(12), pp.7992–7.

Kuimova, M.K. et al., 2009. Imaging intracellular viscosity of a single cell during photoinduced cell death. *Nature chemistry*, 1(1), pp.69–73.

Kulik, L. & Lubitz, W., 2009. Electron-nuclear double resonance. *Photosynthesis Research*, 102, pp.391–401.

Labrie, F., 2003. Extragonadal synthesis of sex steroids: intracrinology. *Annales d'endocrinologie*, 64(2), pp.95–107.

Lancaster, G., 1967. Electron paramagnetic resonance (a review). *Journal of Materials Science*, 2(5), pp.489–495.

Lavalette, D., Tetreau, C. & Momenteau, M., 1979. Laser photolysis of hemochromes. Kinetics of nitrogenous bases binding to four-coordinated and five-coordinated iron(II) tetraphenylporphine. *Journal of the American Chemical Society*, 101(18), pp.5395–5401.

Lee-Robichaud, P. et al., 1995. Mechanistic kinship between hydroxylation and desaturation reactions: acyl-carbon bond cleavage promoted by pig and human CYP17 (P-45017.alpha.; 17.alpha.-hydroxylase-17,20-lyase). *Biochemistry*, 34(43), pp.14104–14113.

Lee-Robichaud, P., Akhtar, M.E. & Akhtar, M., 1998. Control of androgen biosynthesis in the human through the interaction of Arg347 and Arg358 of CYP17 with cytochrome b5. *Biochemical Journal*, 332, pp.293–296.

Leibl, W., Nitschke, W. & Hüttermann, J., 1986. Spin-density distribution in the [FeO2]-complex. Electron spin resonance of myoglobin single crystals. *Biochimica et Biophysica Acta (BBA)/Protein Structure and Molecular*, 870(1), pp.20–30.

Leitz, A. et al., 2006. Functional reconstitution of β2-adrenergic receptors utilizing self-assembling Nanodisc technology. *BioTechniques*, 40(5), pp.601–612.

Li, D. et al., 2007. Substrate- and Isoform-Specific Dioxygen Complexes of Nitric Oxide Synthase. *J. Am. Chem. Soc.*, 129(21), pp.6943–6951.

Li, M. & Hazelbauer, G.L., 2011. Core unit of chemotaxis signaling complexes. *Proceedings of the National Academy of Sciences of the United States of America*, 108(23), pp.9390–5.

Linderstrøm–Lang, K. & Schellman, J.A., 1959. Protein structure and enzymatic activity. In H. Lardy & K. Myrback, eds. *The Enzymes*. New York: Academic Press, pp. 443–510.

Lipscomb, J.D. et al., 1976. Autooxidation and hydroxylation reactions of oxygenated cytochrome P-450cam. *The Journal of Biological Chemistry*, 251(4), pp.1116–24.

Liu, Y. & Ortiz de Montellano, P.R., 2000. Reaction intermediates and single turnover rate constants for the oxidation of heme by human heme oxygenase-1. *The Journal of biological chemistry*, 275(8), pp.5297–307.

Love, R.R., 1994. Effect of Tamoxifen on Lumbar Spine Bone Mineral Density in Postmenopausal Women After 5 Years. *Archives of Internal Medicine*, 154(22), p.2585.

Luthra, A. et al., 2013. Nanodiscs in the studies of membrane-bound cytochrome P450 enzymes. In I. R. Phillips, E. A. Shepard, & P. R. O. De Montellano, eds. *Cytochrome P450 Protocols: Methods in Molecular Biology*. New York: Humana Press, pp. 115–27.

Luthra, A., Denisov, I.G. & Sligar, S.G., 2011a. Spectroscopic features of cytochrome P450 reaction intermediates. *Archives of Biochemistry and Biophysics*, 507(1), pp.26–35.

Luthra, A., Denisov, I.G. & Sligar, S.G., 2011b. Temperature Derivative Spectoscopy To Monitor the Autoxidation Decay of Cytochromes P450. *Analytical Chemistry*, 83, pp.5394–5399.

Mak, P.J. et al., 2011. Defining CYP3A4 Structural Responses to Substrate Binding. Raman Spectroscopic Studies of a Nanodisc-Incorporated Mammalian Cytochrome P450. *Journal of the American Chemical Society*, pp.1–21.

Mak, P.J., Kaluka, D., et al., 2008. Defining resonance Raman spectral responses to substrate binding by cytochrome P450 from Pseudomonas putida. *Biopolymers*, 89(11), pp.1045–53.

Mak, P.J. et al., 2004. Effects of systematic peripheral group deuteration on the low-frequency resonance Raman spectra of myoglobin derivatives. *Biopolymers*, 75(3), pp.217–28.

Mak, P.J. et al., 2014. Resonance Raman spectroscopy reveals that substrate structure selectively impacts the heme-bound diatomic ligands of CYP17. *Biochemistry*, 53(1), pp.90–100.

Mak, P.J., Im, S.-C., et al., 2008. Resonance Raman studies of cytochrome P450 2B4 in its interactions with substrates and redox partners. *Biochemistry*, 47(12), pp.3950–63.

Mak, P.J., Zhu, Q. & Kincaid, J.R., 2013. Using resonance Raman cross-section data to estimate the spin state populations of Cytochromes P450. *Journal of Raman Spectroscopy*, 44(12), pp.1792–1794.

Makris, T.M. et al., 2007. Alteration of P450 distal pocket solvent leads to impaired proton delivery and changes in heme geometry. *Biochemistry*, 46(49), pp.14129–14140.

Marty, M.T. et al., 2012. Native mass spectrometry characterization of intact nanodisc lipoprotein complexes. *Analytical chemistry*, 84(21), pp.8957–60.

Maves, S.A. & Sligar, S.G., 2001. Understanding thermostability in cytochrome P450 by combinatorial mutagenesis. *Protein science : a publication of the Protein Society*, 10(1), pp.161–8.

McCammon, J.A., 1984. Protein dynamics. *Reports on Progress in Physics*, 47, pp.1–46.

McKenna, C.E., Gutheil, W.G. & Song, W., 1991. A method for preparing analytically pure sodium dithionite. Dithionite quality and observed nitrogenase-specific activities. *Biochimica et biophysica acta*, 1075(1), pp.109–17.

McLean, M.A. et al., 1998. Characterization of a cytochrome P450 from the acidothermophilic archaea Sulfolobus solfataricus. *Biochemical and biophysical research communications*, 252(1), pp.166–72.

Morrissey, J.H. et al., 2008. Blood clotting reactions on nanoscale phospholipid bilayers. *Thrombosis Research*, 122 Suppl, pp.S23–6.

Morrissey, J.H., Tajkhorshid, E. & Rienstra, C.M., 2011. Nanoscale studies of protein-membrane interactions in blood clotting. *Journal of thrombosis and haemostasis : JTH*, 9 Suppl 1, pp.162–7.

Nagano, S., Cupp-Vickery, J.R. & Poulos, T.L., 2005. Crystal structures of the ferrous dioxygen complex of wild-type cytochrome P450eryF and its mutants, A245S and A245T: investigation of the proton transfer system in P450eryF. *The Journal of biological chemistry*, 280(23), pp.22102–7.

Nagano, S. & Poulos, T.L., 2005. Crystallographic study on the dioxygen complex of wild-type and mutant cytochrome P450cam. Implications for the dioxygen activation mechanism. *The Journal of Biological Chemistry*, 280(36), pp.31659–63.

Nelson, D.R., 2013. A world of cytochrome P450s. *Philosophical transactions of the Royal Society of London. Series B, Biological sciences*, 368(1612), p.20120430.

Nelson, D.R., 2009. The cytochrome p450 homepage. *Human genomics*, 4(1), pp.59–65.

Ng, K. & Rosenberg, A., 1991. The coupling of catalytically relevant conformational fluctuations in subtilisin BPN' to solution viscosity revealed by hydrogen isotope exchange and inhibitor binding. *Biophysical chemistry*, 41(3), pp.289–299.

Nienhaus, G.U. et al., 1994. Ligand binding to heme proteins: the effect of light on ligand binding in myoglobin. *Biochemistry*, 33(45), pp.13413–30.

Nienhaus, K. & Nienhaus, G.U., 2011. Ligand dynamics in heme proteins observed by Fourier transform infrared-temperature derivative spectroscopy. *Biochimica et biophysica acta*, 1814(8), pp.1030–41.

Oang, K.Y. et al., 2014. Conformational Substates of Myoglobin Intermediate Resolved by Picosecond X-ray Solution Scattering. *The journal of physical chemistry letters*, 5(5), pp.804–808.

Omura, T. & Sato, R., 1962. A New Cytochrome in Liver Microsomes. *The Journal of Biological Chemistry*, 237, pp.1375–1376.

Peterson, E.S. et al., 1998. Functional implications of the proximal hydrogen-bonding network in myoglobin: A resonance raman and kinetic study of Leu89, Ser92, His97, and F- helix swap mutants. *Biochemistry*, 37, pp.12301–12319.

Pilbrow, J.R. & Hanson, G.R., 1993. Electron paramagnetic resonance. *Methods in Enzymology*, 227, pp.330–353.

Podust, L.M., Poulos, T.L. & Waterman, M.R., 2001. Crystal structure of cytochrome P450 14alpha -sterol demethylase (CYP51) from Mycobacterium tuberculosis in complex with azole inhibitors. *Proceedings of the National Academy of Sciences of the United States of America*, 98(6), pp.3068–73.

Poulos, T.L. et al., 1985. The 2.6-A crystal structure of Pseudomonas putida cytochrome P-450. *The Journal of biological chemistry*, 260(30), pp.16122–30.

Raag, R. et al., 1991. Crystal structure of the cytochrome P-450CAM active site mutant Thr252Ala. *Biochemistry*, 30(48), pp.11420–9.

Ritchie, T.K. et al., 2009. Reconstitution of Membrane Proteins in Phospholipid Bilayer Nanodiscs. *Methods in Enzymology*, 464(09), pp.211–231.

Rosenberg, A., Ng, K. & Punyicski, M., 1989. Activity and viscosity effects on the structural dynamics of globular proteins in mixed solvent systems. *Journal of Molecular Liquids*, 42, pp.31–43.

Rowland, P. et al., 2006. Crystal structure of human cytochrome P450 2D6. *The Journal of biological chemistry*, 281(11), pp.7614–22.

Shenkarev, Z.O. et al., 2010. NMR structural and dynamical investigation of the isolated voltage-sensing domain of the potassium channel KvAP: implications for voltage gating. *Journal of the American Chemical Society*, 132(16), pp.5630–7.

Shimada, H. et al., 1997. Heme Monooxygenases. In T. Funabiki, ed. *Oxygenases and Model Systems*. Catalysis by Metal Complexes. Dordrecht: Kluwer Academic Publishers, pp. 195–221.

Shozu, M. et al., 2003. Estrogen excess associated with novel gain-of-function mutations affecting the aromatase gene. *The New England journal of medicine*, 348(19), pp.1855–65.

Shyadehi, A.Z. et al., 1996. The Mechanism of the Acyl-Carbon Bond Cleavage Reaction Catalyzed by Recombinant Sterol 14{alpha}-Demethylase of Candida albicans (Other Names Are: Lanosterol 14{alpha}-Demethylase, P-45014DM, and CYP51). *J. Biol. Chem.*, 271(21), pp.12445–12450.

Simpson, E.R. et al., 2002. Aromatase -a brief overview. *Annual Review of Physiology*, 64, pp.93–127.

Simpson, E.R. et al., 1994. Aromatase Cytochrome P450, The Enzyme Responsible for Estrogen Biosynthesis. *Endocrine Reviews*, 15(3), pp.342–355.

Simpson, E.R., 2000. Genetic Mutations Resulting in Loss of Aromatase Activity in Humans and Mice. *Journal of the Society for Gynecologic Investigation*, 7(1 (Supplement)), pp.S18–21.

Singh, S.K. et al., 2013. Membrane Protein Interaction Studies using Microscale Thermophoresis. *Biophysical Journal*, 104(2), p.557a–558a.

Sinibaldi, R. et al., 2007. Preferential hydration of lysozyme in water/glycerol mixtures: a small-angle neutron scattering study. *The Journal of Chemical Physics*, 126(23), p.235101.

Sloan, C.D.K. et al., 2013. Interfacing lipid bilayer nanodiscs and silicon photonic sensor arrays for multiplexed protein-lipid and protein-membrane protein interaction screening. *Analytical chemistry*, 85(5), pp.2970–6.

Somogyi, B. et al., 1988. Viscosity and transient solvent accessibility of Trp-63 in the native conformation of lysozyme. *Biophysical chemistry*, 32(1), pp.1–13.

Spiro, T.G. & Czernuszewicz, R.S., 1995. Resonance Raman Spectroscopy of Metalloproteins. *Methods in Enzymology*, 246(1985), pp.416–460.

Spiro, T.G., Soldatova, A. V & Balakrishnan, G., 2013. CO, NO and O2 as Vibrational Probes of Heme Protein Interactions. *Coordination chemistry reviews*, 257(2), pp.511–527.

Spiro, T.G. & Wasbotten, I.H., 2005. CO as a vibrational probe of heme protein active sites. *Journal of inorganic biochemistry*, 99(1), pp.34–44.

Symons, M.C.R. & Petersen, R.L., 1978. Electron capture by oxyhaemoglobin: an e.s.r. study. *Proceedings of the Royal Society of London - Biological Sciences*, 201(1144), pp.285–300.

Tilton, R.F., Dewan, J.C. & Petsko, G.A., 1992. Effects of temperature on protein structure and dynamics: x-ray crystallographic studies of the protein ribonuclease-A at nine different temperatures from 98 to 320K. *Biochemistry*, 31(9), pp.2469–2481.

Tosha, T. et al., 2006. Raman evidence for specific substrate-induced structural changes in the heme pocket of human cytochrome P450 aromatase during the three consecutive oxygen activation steps. *Biochemistry*, 45(17), pp.5631–40.

Tuckey, R.C. & Kamin, H., 1982. The oxyferro complex of adrenal cytochrome P-450scc. Effect of cholesterol and intermediates on its stability and optical characteristics. *The Journal of Biological Chemistry*, 257(16), pp.9309–9314.

Vaz, A.D.N. et al., 1996. Peroxo-iron and oxenoid-iron species as alternative oxygenating agents in cytochrome P450-catalyzed reactions: switching by threonine-302 to alanine mutagenesis of cytochrome P450 2B4. *Proceedings of the National Academy of Sciences*, 93(10), pp.4644–8.

Vermilion, J.L. & Coon, M.J., 1978. Purified liver microsomal NADPH-cytochrome P-450 reductase. Spectral characterization of oxidation-reduction states. *The Journal of biological chemistry*, 253(8), pp.2694–704.

Vidakovic, M. et al., 1998. Understanding the Role of the Essential Asp251 in Cytochrome P450cam Using Site-Directed Mutagenesis , Crystallography , and Kinetic Solvent Isotope Effect. *Biochemistry*, 37(26), pp.9211–19.

Wertz, D.L. et al., 1998. Mimicking Cytochrome P-450 2B4 and Aromatase: Aromatization of a Substrate Analogue by a Peroxo Fe(III) Porphyrin Complex. *Journal of the American Chemical Society*, 120(21), pp.5331–5332.

Williams, P.A. et al., 2004. Crystal structures of human cytochrome P450 3A4 bound to metyrapone and progesterone. *Science (New York, N.Y.)*, 305(5684), pp.683–6.

Woodward, J.J. et al., 2009. The second step of the nitric oxide synthase reaction: evidence for ferric-peroxo as the active oxidant. *Journal of the American Chemical Society*, 131(1), pp.297–305.

Yedgar, S. et al., 1995. Viscosity dependence of O2 escape from respiratory proteins as a function of cosolvent molecular weight. *Biophysical Journal*, 68(2), pp.665–70.

Young, R.D. & Bowne, S.F., 1984. Conformational substates and barrier height distributions in ligand binding to heme proteins. *The Journal of Chemical Physics*, 81(8), p.3730.